Technische Universität München
TUM School of Medicine and Health

Activating transcriptional elongation as a strategy to treat aggressive mesenchymal pancreatic ductal adenocarcinoma

Janine V. Murr

Vollständiger Abdruck der von der TUM School of Medicine and Health der Technischen Universität München zur Erlangung des akademischen Grades eines

Doctor of Philosophy (Ph.D.)

genehmigten Dissertation.

Vorsitz:	Prof. Dr. Susanne Kossatz
Betreuer:	Prof. Dr. Günter Schneider
Prüfer*innen der Dissertation:	1. Prof. Dr. Roland M. Schmid
	2. Prof. Dr. Oliver Krämer

Die Dissertation wurde am 04.09.2023 bei der
Technischen Universität München eingereicht und durch die
TUM School of Medicine and Health am 30.11.2023 angenommen.

Table of contents

Listings

List of Figures

List of Tables

List of Abbreviations

× g ..... *times gravity*
5-FU *5-Flourouracil*
A3SS ..... *Alternative 3' splice site*
A5SS ..... *Alternative 5' splice site*
ADEX ..... *aberrantly differentiated endocrine exocrine*
ADM ..... *Acinar-to-ductal metaplasia*
ANOVA ..... *Analysis of variance*
APS ..... *ammonium persulfate*
ARID1A ..... *AT-Rich interaction domain 1a*
AS ..... *aminoacids*
ATM ..... *Ataxia Telangiectasia mutated*
ATP ..... *adenosine triphosphate*
BRCA ..... *Breast Cancer*
BSA ..... *bovine serum albumin*
CC1 family ..... *Cys-based Class*
CDK ..... *Cyclin dependent kinase*
CDKN2A ..... *cyclin-dependent kinase inhibitor 2A*
cDNA ..... *complementary DNA*
ChIP ..... *Chromatin Immunoprecipitation*
CIP2A ..... *cancerous inhibitor of PP2A*
CIP2A ..... *Cellular inhibitor of PP2A*
CN-LOH ..... *copy neutral loss of heterozygosity*
CNV ..... *copy number variations*
CPTAC ..... *Clinical proteomic tumour analysis consortium*
CPTAC Cancer ..... *Institute's clinical proteomic tumor analysis consortium*
CRISPR ..... *clustered regularly interspaced short palindromic repeats*
CTD ..... *C-terminal domain*
DepMap ..... *Dependency Map*
DI ..... *Detained introns*
DMEM ..... *Dulbecco's modified eagle medium*
DMSO ..... *dimethylsulfoxide*
DNA ..... *Deoxyribonucleic acid*
DSIF ..... *DRB sensitivity inducing factor*
DSP ..... *Dual specific phosphatase*
DXDXT/V ..... *aspartate based phosphatases*
ECAR ..... *extracellular acidification rate*
EGFR ..... *Epidermal growth factor receptor*
EIF ..... *Eukaryotic translation initation factor*
EMT ..... *epithelial-to-mesenchymal transition*
ER ..... *Endoplasmic reticulum*
ERBB2 ..... *v-erb-b2 erythroblastic leukemia viral oncogene homolog 2*
EtOH ..... *Ethanol*
FAP ..... *Fibroblast activation protein*
FC ..... *fold change*
FCCP ..... *carbonyl cyanide-p-trifluoromethoxyphenylhydrazone*
FCS ..... *fetal calf sera*
FDA ..... *Food and Drug Administration*
FDR ..... *false discovery rate*, *false discovery rate*
FGFR ..... *Fibroblast growth factor receptors*
Fig ..... *Figure*
FITC *fluorescein-5-isothiocyanate*
FOLFIRINOX ..... *Folinsäure, 5-Fluorouracil, Irinotecan, Oxaliplatin*
FSF ..... *Frt-Stop-Frt casette*

FTY720 ..... *Fingolimod*
G1/S ..... *Gap1 / Synthese phase*
G2/M ..... *Gap2 /mitosis phase*
GEMM ..... *genetic engineered mouse models*
GI_{50} ..... *50 % growth inhibitory*
GRO-Seq ..... *Global run-on sequencing*
GSEA ..... *gene set enrichment analysis*
GTEx ..... *genotype-tissue expression*
HCC ..... *hepatocellular carcinoma*
HDI ..... *Higher development index*
HEK ..... *human embryonic kidney*
HET ..... *heterozygote*
HGNC ..... *HUGO gene nomenclature committee*
HIF-1a ..... *hypoxia-inducible factor alpha*
HOM ..... *homozygote*
HRP ..... *horseradish peroxidase*
HRR ..... *homologous recombination repair*
IEG ..... *Immediate early genes*
IgG ..... *Immunoglobulin G*
IPA ..... *Alternative polyadenylation*
ISR ..... *Integrated stress response*
KEGG ..... *Kyoto encyclopaedia of genes and genomes*
KRAS ..... *Kirsten rat sarcoma virus*
LB ..... *lysogeny broth*
LCM ..... *Laser capture microdissection*
LCMT1 ..... *leucine carboxyl transferase1*
LoxP ..... *Cre/LoxP recombination system*
LSL ..... *Lox-Stop-Lox*
MAGeCK ..... *Model-based analysis of genome-wide CRISPR/Cas9 knockout*
MAPK ..... *Mitogen activated protein kinase*
MDS ..... *myelodysplastic syndrome*
MEM ..... *minimal essential media*
MID ..... *Midline*
MID1 ..... *Midline 1*
MOI ..... *Multiplicity of infection*
MPF ..... *M phase-promoting factor*
mRNA ..... *messenger RNA*
MSigDB ..... *molecular signature database*
MSigDB ..... *Molecular signature database*
MTD ..... *maximum tolerated dose*
NELF ..... *Negative elongation factor*
NES ..... *normalised enrichment score*
NGS ..... *next-generation sequencing*
NSCLC ..... *non-small cell lung carcinoma*
OCR ..... *oxygen consumption rate*
OD ..... *optical density*
P/S ..... *Penicillin/Streptomycin*
PAAD ..... *Pancreatic adenocarcinoma*
PanIN ..... *pancreatic intra-epithelial neoplasm*
PBS ..... *phosphate buffered saline*
PCR ..... *polymerase chain reaction*
PDAC ..... *Pancreatic ductal adenocarcinoma*
PDCL ..... *patient derived cell lines*
PDO ..... *patient derived organoids*
PDVF ..... *polyvinylidenfluoride*

PDX1 ……*Pancreatic and duodenal homeobox 1*
PFA……*paraformaldehyde*
PI ……*propidium iodide*
PI3K ……*Phosphoinositid-3-Kinasen*
PP1 ……*Protein phosphatase 1*
PP2A……*Protein phosphatase 2A*
PPM ……*metal-dependent protein phosphatases*
PPP-like ……*Phospho-protein phosphatase like*
PPT……*Primary patient tumor*
ProteomicsDB ……*Proteomics database*
P-TEF……*Positive transcription elongation factor*
PTEN ……*Phosphatase and tensin homolog*
PTF1……*Pancreas associated transcription factor 1*
PTM ……*post-translational modifications*
PTP……*protein tyrosine phosphatases*
PTPA……*phosphotyrosyl phosphatase activator*
QCMG……*Queensland centre of medical genomics*
QM ……*quasimesenchymal*
Q-PCR ……*quantitative PCR*
RIPA ……*radioimmunoprecipitation assay buffer*
RNA ……*Ribonucleic acid*
RNAseq……*RNA sequencing*
ROBO2 ……*Roundabout guidance receptor 2*
ROS……*Reactive oxygen species*
RPMI……*Roswell park memorial institute 1640 media*
RRID ……*Research resource identifiers*
SD ……*Standard deviation*
SDS-PAGE ……*sodium dodecyl sulfate polyacrylamide gel*
SE ……*Skipped exons*
Ser/Thr……*Serin/Threonin*
SG ……*Stress granules*
sgRNA……*single guide RNA*
SMA ……*Smooth muscle actin*
SMAD4……*mothers against decapentaplegic homolog 4*
snRNA ……*small nuclear RNA*
SOC……*super optimal broth with catabolite repression*
SPARC……*Secreted protein acidic and cysteine rich*
STAT ……*Signal transducer and activator of transcription*
STK11……*Serin/Threonine-Kinase 11*
SUnSET……*surface sensing of translation*
SV 40 ……*Simian-Virus 40*
SV40 ……*Simian-Virus 40*
TAE……*Tris acetate EDTA*
T-ALL ……*T cell acute lymphoblastic leukaemia*
TBS……*tris buffered saline*
TCGA……*The cancer genome atlas*
TE ……*Tris-EDTA*
TEMED……*Tetramethylethylendiamin*
TGFß ……*Transforming growth factor ß*
TNF……*tumour necrosis factor*
TNF ……*Tumor necrosis factor*
TP53 ……*tumour suppressor protein 53*
TPM ……*transcripts per million*
tRNA ……*transport RNA*
TSB……*tryptic soy broth*

USA ..... *United States of America*
VEGF ..... *Vascular endothelial growth factor*

Summary

Pancreatic ductal adenocarcinoma (PDAC) stands out as an exceptionally aggressive cancer variant and the most common neoplasia of the pancreas, with a dismal prognosis for the patient. This is primarily due to late-stage detection at already advanced stages and a lack of targeted therapies. Since the tumour is highly heterogeneous, precision and subtype-specific treatment could improve future therapy applications. Genetic dropout screens combined with patient genomic data and pathway annotations revealed the catalytic subunit of the protein phosphatase 2A (PP2A) as a potential target for the treatment of pancreatic cancer. Beyond that, a PDAC subtype-specific sensitivity could be first demonstrated by using the inhibitor LB-100, an inhibitor of the catalytic site of the phosphatase which has already undergone preliminary evaluation in a human clinical trial. Undifferentiated, mesenchymal pancreatic cancer cells and patient derived organoids revealed a high response to the inhibitor in a low micromolar range, resulting in apoptotic cell death. Deeper analysis elucidated the integrated stress response (ISR) of the endoplasmic reticulum (ER), autophagy and a collapse of the homeostatic networks as a response to LB-100 treatment preeminently in the mesenchymal subtype. On top, CRISPR-Cas9 genetic dropout screens revealed components of the transcription cycle as pivotal nodes. CDK9, in particular, emerged as the potential mechanistic factor governing the transcriptional elongation subsequent to PP2A inhibition and the consequent abrogation of the pause checkpoint. Enhanced transcriptional elongation and splicing rates after LB-100 treatment, combined with increased induction of immediate early genes (IEG) confirmed this assumption. Impressively, the phenotypic effects can be mitigated by pharmacological suppression of CDK9 in tandem with LB-100 treatment. Overall, this data provides evidence for a new subtype specific treatment option and could lead to future biomarker identification due to detailed insights into the mechanistic cellular response to LB-100 treatment. All in all, these novel insights could help find rational synergistic drug combinations and therefore improve patients' outcomes.

Zusammenfassung

Das duktale Adenokarzinom des Pankreas (PDAC) ist eine äußerst aggressive Krebsvariante und die häufigste Neoplasie der Bauchspeicheldrüse. Die Prognose für den Patienten ist aufgrund der häufig späten Diagnose in fortgeschrittenen Stadien und des Mangels an gezielten Therapien sehr schlecht. Da der Tumor sehr heterogen ist, könnte eine präzise und subtyp-spezifische Behandlung zukünftige Therapieanwendungen verbessern. Genetische Dropout-Screens in Kombination mit genomischen Patientendaten und Signalwegannotierungen ergaben, dass die katalytische Untereinheit der Protein Phosphatase 2A (PP2A) ein potenzielles Ziel für die Behandlung von Bauchspeicheldrüsenkrebs sein könnte. Mithilfe des Inhibitors LB-100, einem Inhibitor der katalytischen Untereinheit der Phosphatase, der bereits in einer ersten klinischen Studie am Menschen untersucht wurde, konnte darüber hinaus erstmals eine PDAC subtyp-spezifische Empfindlichkeit nachgewiesen werden. Undifferenzierte mesenchymale Bauchspeicheldrüsenkrebszellen und von Patienten stammende Organoide zeigten eine starke Reaktion auf den Inhibitor im niedrigen mikromolaren Bereich, was schließlich zum Zelltod durch Apoptose führte. Weitere eingehendere Analysen implizierten die integrierte Stressreaktion (ISR) des endoplasmatischen Retikulums (ER), Autophagie und einen Zusammenbruch der homöostatischen Netzwerke als Reaktion auf die LB-100-Behandlung vermehrt im mesenchymalen Subtyp. Darüber hinaus zeigten CRISPR-Cas9 genetische Dropout Screens Komponenten des Transkriptionszyklus als Angriffspunkt von LB-100. Insbesondere CDK9 erwies sich als potenzieller mechanistischen Faktor, der die Transkriptionsverlängerung nach der PP2A-Hemmung und dem damit verbundenen deaktivierten Pausenkontrollpunkt steuert. Erhöhte Transkriptions- und Splicingraten nach LB-100 Behandlung in Kombination mit einer erhöhten Induktion unmittelbar früher Gene (IEG) bestätigten diese Annahme. Beeindruckend ist, dass die phänotypischen Effekte durch die pharmakologische Unterdrückung von CDK9 in Kombination mit der LB-100-Behandlung gemildert werden können. Insgesamt liefern diese Daten Hinweise auf eine neue subtypspezifische Behandlungsoption und könnten durch die beschriebene zelluläre Reaktion zur zukünftigen Identifizierung von Biomarkern beitragen. Alles in allem könnten diese neuen Erkenntnisse dazu beitragen, rationale synergistische Arzneimittelkombinationen zu finden und so die Behandlungsergebnisse für Patienten zu verbessern

Graphical abstract

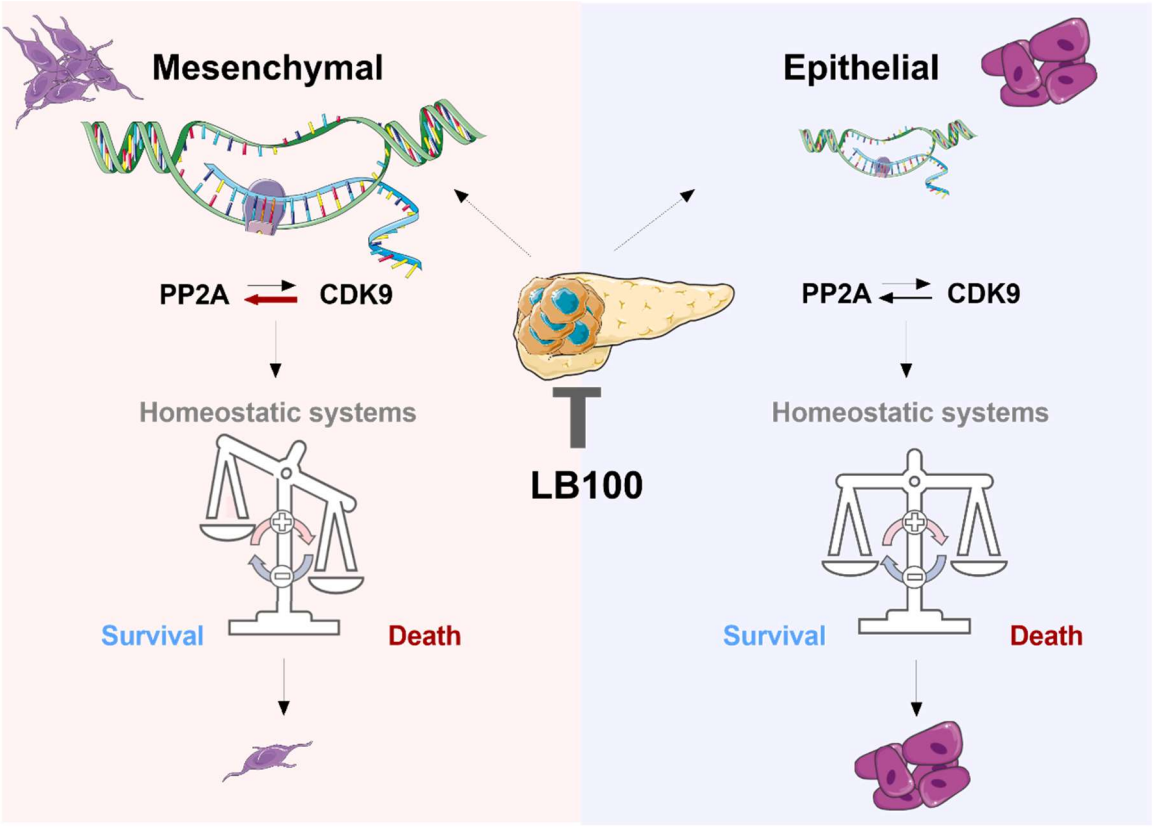

1 Introduction

1.1 Pancreatic Cancer

1.1.1 Epidemiology and risk factors

Cancer, in principle, is the first- or second leading cause of death before the age of 70 in almost all countries of the world and although the mortality is decreasing over the past years, the numbers of cases each year are still rising[1,2]. This is mostly directly correlating with advanced ages, populations growth and an increase of the high risk factors due to socioeconomic development, reflected also in the direct correlation of the higher development index (HDI) in comparison with cancer deaths [2–6]. But overall, the 5-year survival rates, including all types of cancers, still increased to 68 % with the highest rates in prostate, kidney and breast cancer[7]. The lowest 5-year survival rate is still predetermined for pancreatic cancer, having a poor prognosis and outcome with a 5-year survival rate of less than 12 %[7] (Fig. 1 a,b). It is projected to be even the second leading cause of death in the next decades, mostly resulting from unspecific symptoms, no effective screening method and therefore late diagnosis at advanced stages of tumour development, metastasis and still limited treatment options [1,8,9]. Pancreatic ductal adenocarcinoma (PDAC) is an exocrine pancreatic cancer and the most common type of this disease, resulting in 85-90 % of all pancreatic neoplasms [8,10]. The minor subtypes are acinar carcinoma, pancreaticoblastoma, and neuroendocrine tumours. [11]

The risk factors for pancreatic cancer are widely distributed and mostly not only caused by a single agent. For most of the cases, sporadically occurring mutations lead to pancreatic cancer (>80 %) [12], but genetic predispositions can identify high-risk groups or therapy options. Overall, these predispositions only account for 10 % of all pancreatic cancer cases [13]. Patients carrying inherited or acquired genetic mutations in susceptibility genes like *BRCA1, BRCA2, P16/CDKN2, STK11/LKB1, PALP2, ATM, TP53* or *PRSS1* have a higher risk to also develop pancreatic cancer, with the highest risk for *STK11/LKB1* mutations (Peutz-Jeghers Syndrome, 132-fold) [14]. The same is also true for patients with chronic pancreatitis or a family history of pancreatic cancer [6,15]. Moderate risk results also from modifiable risk factors like obesity and low physical activity, diabetes type 2 (long term) and also high tobacco use and alcohol intake [6,13,14]. A direct correlation between fatty acid incorporation into pancreatic tissue and the development of the precursor lesions (pancreatic intraepithelial neoplasia (PanIN)) for PDAC could further be demonstrated [16]. On the other side, treatment of diabetes with metformin confirmed a reduced risk for pancreatic cancer[17].

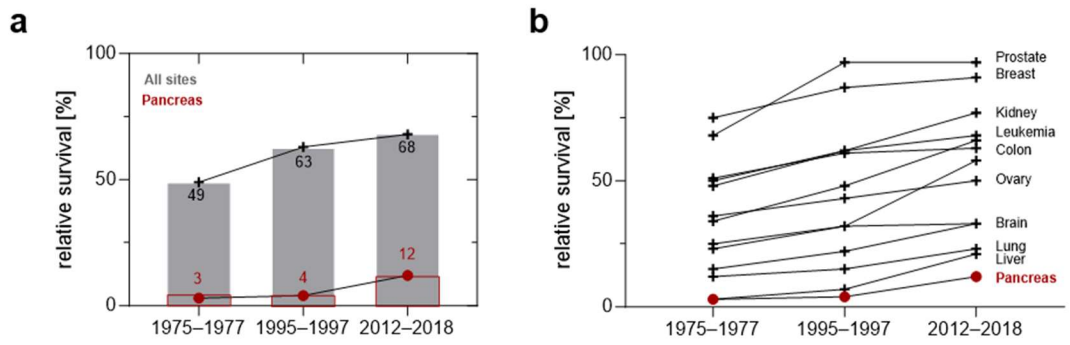

Figure 1 | 5-year survival rate remains poor for pancreatic cancer

a, Changes of the relative 5-year survival rate [%] during the last 50 years from all cancer entities and pancreatic cancer in the US (red line). **b,** Survival rates improved over the last decades for different cancer sites, except pancreatic cancer, which has the lowest 5-year survival rate for all cancer entities. Graphs according to Cancer statistics, 2023 [7].

1.1.2 Symptoms and treatment options

The 5-year survival rate of only 12 % for pancreatic cancer is still quite low compared to gains in survival in other tumour entities[7], because most of the patients are diagnosed when the tumour is already in a late stage (locally advanced (30 %-35 %) or metastatic (50 %-55 %))[18] . This results from unspecific symptoms, which lead to a usually median time-delay between presentation, even if symptomatic, and diagnosis and treatment of around two months [19,20]. The most common and unspecific symptoms described by the patients are physical weakness (86 %), anorexia (83 %) and weight loss (85 %), followed by abdominal epigastric pain (79 %) [20]. Specific clinical symptoms, relevant for a rapid diagnosis, are much less common (jaundice (55 %), hepatomegaly (29 %), cachexia (13 %), epigastric mass (9 %), or ascites (5 %)) [10,20].

So far, the only curative option lies in surgical removal, which is possible in only 10-20 % of the cases. Yet still, postoperative multimodal treatment is needed for most of the patients, even if they have negative margins at resection [8,12,21]. Standard therapy for these patients at the moments is a postoperative adjuvant chemotherapy (after the resection) with gemcitabine and capecitabine, leading to an overall 5-year survival rate of 30 % [22]. But the majority of tumours are not resectable, borderline resectable or locally advanced and therefore, the application of neoadjuvant chemotherapy preceding the resection is now the standard of treatment [8,21,22]. The advantages of neoadjuvant treatment preceding resection result from testing of the chemosensitivity in an early stage, better and earlier control of circulating tumour cells and micrometastases and higher R0 resection rate [8]. In an already metastatic clinical finding, which is the case for most of the

diagnosed patients, tumours are usually unresectable and palliative care is the only feasible option [8]. For a long time gemcitabine was considered the first line therapy option for metastasising tumours, leading to an increase of the median overall survival rate from 4.41 to 5.65 months and becoming the standard of care [23]. The addition of Nab-paclitaxel (albumin-bound, solvent-free and water-soluble formulation of paclitaxel; 125 mg/m^2 weekly for three out of four weeks together with 1000 mg/m^2 Gemcitabine) increased the overall survival rate from 6.6 to 8.7 months and is nowadays favoured over the monotherapy alone [24]. However, the preferred therapy option for metastatic tumours since 2011 is the combination treatment with FOLFIRINOX (oxaliplatin (85 mg/m^2), irinotecan (180 mg/m^2), and 5-FU (400 mg^2 as bolus and 2400 mg/m^2 as continuous infusion for 46 hours every two weeks) which led to a median overall survival rate of 11.1 months compared to 6.8 months with gemcitabine in the study [25]. Although the FOLFIRINOX treatment showed higher toxicities compared to Gemcitabine, the cancer related symptoms were delayed and the quality of life improved [25–27]. So far, there are no real life expectancy-increasing drugs available, but more and more evidence is coming up, that different subtypes of pancreatic cancer respond differently to available treatment options [27].

1.1.3 Tumour progression, driver mutations and subtypes of PDAC

1.1.3.1 PDAC initiation mechanisms and tumour progression

The distinct feature of being an endocrine as well as exocrine gland with the ability to change the cellular plasticity in already terminally differentiated cell types, makes the pancreas a very special organ. In general, the pancreas consists of different functional compartments, ranging from exocrine acinar cells, which are producing enzymes for the digestive track, endocrine hormone producing cells (Langerhans islets, α, β, δ, ε) or epithelial duct cells [28,29] (Fig. 2a). Among all these cell types, acinar cells are well known for their high degree of cellular plasticity in reaction to diverse cellular stress factors, including injury, metabolic pressure, or inflammation in the pancreas. But this transdifferentiating process with “progenitor cell-like” features is also known as tumour-initiating event in early cancer development stages of PDAC [28–30]. One of the earliest genetic driver events, that are typically acquired during the cancer initiation process and detectable in over 95 % of all PDAC patients, results in the constitutive activation of the proto-oncogene *KRAS* and therefore leads to pancreatic intra-epithelial neoplasm (PanIN1, mucinous lesions with ductal morphology) formation [30–34] (Fig. 2b). PanIN can be clustered according to histological analysis into three distinct stages (PanIN1-3) and can so far not be detected by any available form of clinical imaging.

During cancer progression, an accumulation of diverse genetic alterations and somatic mutations in tumour suppressor genes is detectable, facilitating higher grade PanINs[33]. Next-generation sequencing could demonstrate that genetic alterations in higher grade PDAC (PanIN3) occur in >50 % of the cases in the genes encoding for the tumor suppressor TP53, cyclin-dependent kinase inhibitor 2A (*CDKN2A*) or mothers against decapentaplegic homolog 4 (*SMAD4*)[29,35]. Other key mutations can be found in the PI3-Kinase (*PI3KCA*) or the downstream effector AKT (*AKT2*) [36,37]. Additionally, the epigenetic deregulation, independent of genetic alterations, is often affected during PanIN progression and drives metastasis formation. This includes changes in DNA methylation, histone post-translational modification or non-coding RNAs[38].

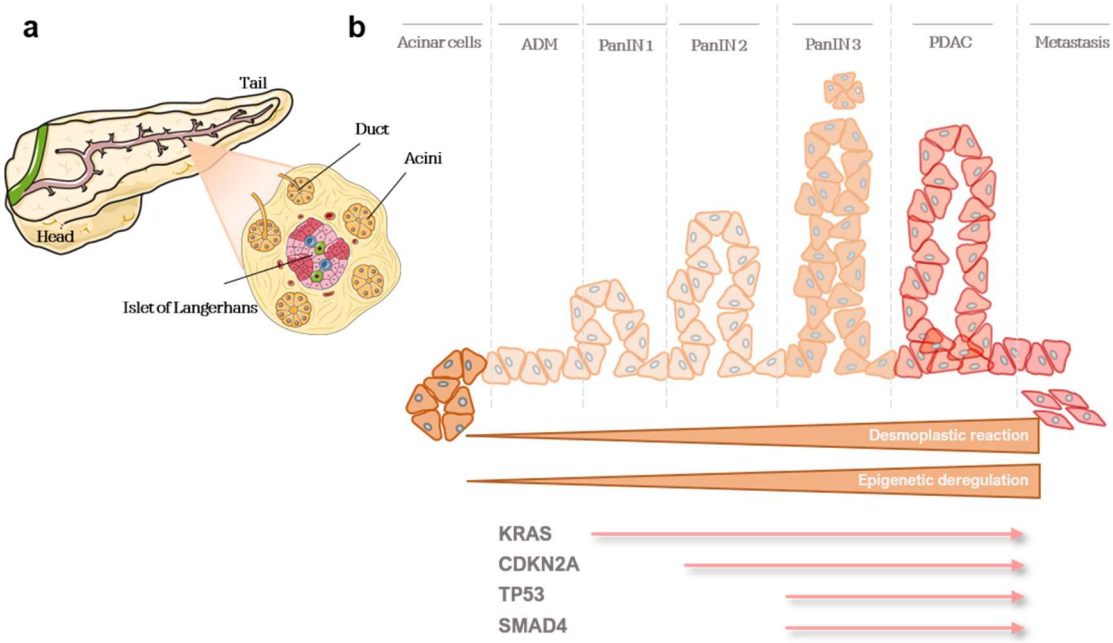

Figure 2 | PDAC initiation and progression model

a, Schematic representation of the pancreas. The functional compartments include exocrine acinar cells, producing enzymes for the digestive track, endocrine cells of the Islet of Langerhans (α, β, δ, ε), necessary for the hormone production and epithelial duct cells. **b**, Illustration of the PDAC initiation and progression model. Acinar cells have the ability to undergo ADM-formation in response to diverse cellular stress factors, and thereby initiating PDAC formation. Additional early genetic alterations in the proto-oncogene KRAS promoting the PanIN formation and cancer development. During progression, further inactivation of genetic mutations in tumour suppressor genes like CDKN2A, TP53 or SMAD4, as well as increasing epigenetic deregulation is acquired, leading to highly aggressive PDAC with metastasis in the end. Figure modified from [29,34].

1.1.3.2 Subtypes of pancreatic cancer

Since pancreatic cancer is quite a complex and heterogeneous disease, a lot of effort was taken to corroborate the molecular, metabolomic and transcriptomic characteristics of this cancer entity and to define subtypes of PDAC to improve personalised treatment options (Fig. 3a) [39–45]. One way to subgroup PDAC is due to genomic aberrations such as deletions, amplifications, duplications or translocations occurring in the genome, detected by whole genome sequencing and copy number variations (CNV) [35,46]. The most prominent rearrangement detected resulting in gene disruption of known PDAC progression and tumour suppressor genes (*TP53, SMAD4, CDKN2A, ARID1A or ROBO2*). Therefore, PDAC can be clustered into 4 different chromosomal stability categories: stable genomes (20 % of all samples, <50 structural variations), locally rearranged subtype (30 % of all samples, >200 variants on <3 chromosomes), scattered subtype (36 % of all samples, <200 structural variation events) or an unstable subtype (14 % of all samples, >200 structural variation distributed across the genome, max.) [35,46]. Patients with a locally rearranged subtype can profit from improved therapy options due to focal amplification in known therapeutic targets (ERBB2 or FGFR) or patients having an unstable subtype gain therapeutic options of DNA-damaging agents due to their defective DNA repair mechanisms[35]. Another way for classification of tumour subtypes, and the most prominent so far, is due to transcriptomic gene expression pattern analysis either determined by array-based hybridization [40,42] or RNAseq data [39,41,42]. In 2011, Collisson et al. did the first bioinformatic analysis of microarray-based hybridization datasets of microdissected, untreated, resected PDAC samples (n=27 and a previously published dataset [47]) and revealed three distinct subtypes of PDAC: a classical, a quasimesenchymal (QM-PDA) and an exocrine-like type, based on subtype specific gene expression pattern. Whereas the classical one demonstrated expression of typical epithelial and adhesion-related genes, the quasimesenchymal showed a clear mesenchymal expression pattern and had the worst prognosis of all tumour subtypes. Furthermore, *GATA6* showed high expression in the classical, but not in the mesenchymal subtype, and therefore is now associated as a “classical” marker [40]. To determine tumour and stromal-specific subtypes, Moffitt et al. performed a virtual microdissection of primary (n = 145) and metastatic (n = 61) PDAC as well as normal samples and found a classical and basal-like subtype in combination with a normal and activated stromal subtype. Overlapping with previous findings, the basal-like subtype and patients with activated stroma, exhibited a poorer prognosis and decreased overall survival [42,48]. One year later, Bailey and colleagues analysed 96 PDAC bulk sequencing and 266 mRNA array datasets in combination with histological analysis and demonstrated 4 different subtypes : a squamous one, a

pancreatic progenitor, an immunogenic and an aberrantly differentiated endocrine exocrine (ADEX) subtype [39]. By comparing all three annotation classes, an overlap between the squamous, QM-PDA and basal like subtype can be detected and is generally associated with a poorer prognosis and aggressive tumours [46]. The immunogenic and pancreatic progenitor subtypes correspond to the previous classical subtype, whereas the exocrine and ADEX build the third association and are more like a terminally differentiated normal pancreas [46,48]. In 2018, Puleo and colleagues collected freshly frozen, fixed and paraffin embedded tissue samples from the surgery of 309 patients an analysed the normal as well as tumoral transcriptomic pattern, while also including the tumour microenvironment signals [41]. Survival data from 288 patients were also available from the study, so that a direct correlation between subtype classification and prognosis could be shown. Whereas the two subtypes named “basal-like” and “classical” showed a huge overlap with the previously described classifications, two subgroups of the classical subtype could be identified: one labelled as “pure classical” with low stromal signal and the other one as “immune classic”, showing marked stromal signatures. Between the clear differentiation of the classical and the basal-like subtypes, two other minor stroma enriched subclassifications were established: the “stroma activated” and “desmoplastic” subtype, expressing activated stroma genes (high a-*SMA*, *ACTA2, SPARC* or *FAP*) or high structural and vascularised stroma components, respectively [41,46]. To capture also high grade patients with already metastatic tumours (Grad 4), Chan-Seng-Yue et al., firstly implemented these tumour samples in the most recent study cohort with 330 LCM-purified primary and metastatic tumours [45]. After analysation of the gene expression pattern, the five subtypes not only confirmed previous classifications in a basal-like and classical subtype, but specified them even more. The basal-like was divided in *classical A or B,* correlating mostly with early-stage tumours (Stage I/II), whereas the *basal-like subgroup A* was found more representative of Stage IV tumours. *Basal-like B* and *Hybrid* tumours grouped to previous found “basal-like” tumours. Interestingly, epithelial-to-mesenchymal signatures, amplification of mutant KRAS, complete loss of CDKN2A, higher frequency of TP53 mutations and TGFß signalling were only positively correlating with the basal-like tumours, leading to a more aggressive phenotype and a decreased overall survival. GATA6 amplification and SMAD4 loss were predominantly found in the classical A/B subtypes [45].

Other classifications were based on different methodologies, including epigenetic and metabolic changes [43,44]. So far, all these classifications have not improved diagnostics or patient’s outcome but reinforced the complexity and heterogeneity of this disease which makes it so difficult to treat.

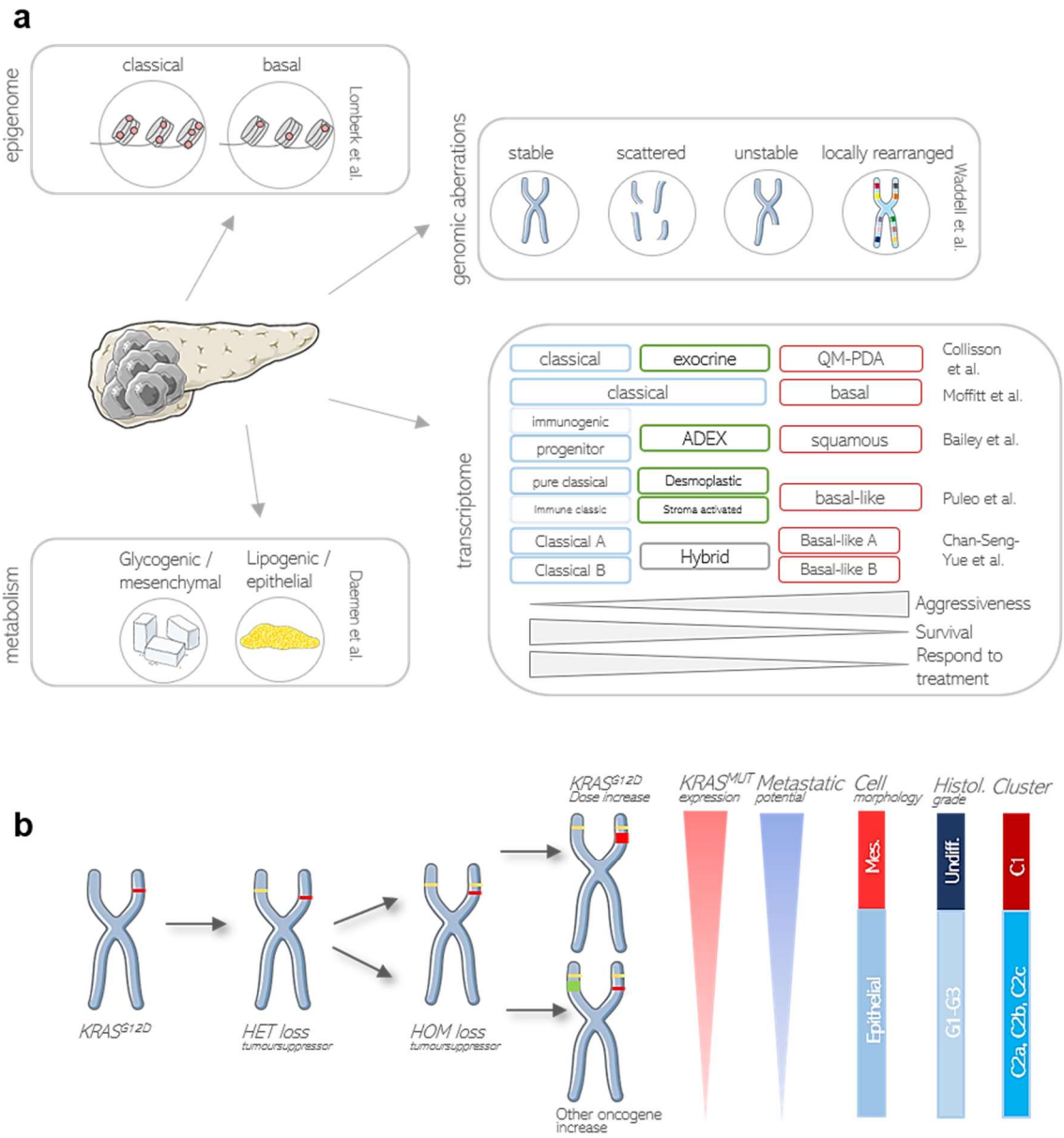

Figure 3 | Subtypes of Pancreatic cancer

a, Genomic aberrations, epigenomic changes, transcriptome analysis or also differences in the metabolism were used to subgroup pancreatic cancer. Whereas genomic aberrations clustered PDAC in four different subtypes, epigenomic and metabolic approaches favour only two subtypes (classical vs. basal or glycogenic vs. lipogenic subtype). A lot of transcriptomic studies over the last year concluded that in principle a quasi-mesenchymal, basal-like and a classical subtype with some subgroupings exist. Figure modified from [48], respective authors are indicated and citated in the text. **b,** Genetic evolution of PDAC formation in mouse models are simplified here. All mice carrying a *KRAS*^{G12D} genetic background, but over time accumulation and *KRAS*^{G12D} dose increase favours a mesenchymal, undifferentiated tumour entity with higher metastatic potential and lower survival (C1 cluster). Additional heterozygote (HET) and later homozygote (HOM) loss of tumour suppressors (e.g., CDKN2A orT P53) are also necessary for tumour development. Mice having other oncogenic dose increase were found to be more representative of the epithelial, well differentiated subtype and therefore having less metastatic potential. Figure adapted from [37].

1.1.3.3 *KRAS^{G12D}* driven mouse models for modelling subtype differences

As described above, PDAC is a highly complex and heterogeneous cancer entity, making it difficult for target therapies and therapeutic options. To get a better understanding of different tumour subtypes, identify tumour drivers and also test new therapy options, *in vivo* studies of genetic engineered mouse models (GEMMs) of PDAC are a powerful tool in pre-clinical research. Since most of the PDAC patients (>95 %) carry a point mutation in codon 12 in the *K-RAS* gene (*KRAS^{G12D}*), the first development of mice carrying this Lox-Stop-Lox-*KRAS^{G12D}* (*LSL- KRAS^{G12D}*) genetic background was a revolutionary step in deciphering cancer formation and evolution of KRAS-driven tumour entities [49]. In these mouse models, the expression of the *KRAS^{G12D}* gene is controlled by an inserted STOP cassette which is flanked by an identical orientated LoxP sites. This LoxP sites can be removed by addition of the Cre recombinase (AdenoCre), resulting in constitutive activation of *KRAS^{G12D}* [49,50].To make sure the activation of this genetic alteration is tissue-specific for the pancreas, Hingorani et. al regulated the expression of *LSL-KRAS^{G12D}* by a Cre recombinase, which is under the control of a pancreas specific *Pdx1* (Pdx1-Cre, “KC-mice”) or *Ptf1* (*P48*) promoter and therefore link the expression to mouse pancreatic progenitor cells [51]. All of the tumours were able to induce ADM and PanIN formation but only some of them underwent PDAC and metastasis development, highlighting the need of additional genetic events occurring in a multistep PDAC progression[50–52]. A lot of effort was undertaken to implement these additional genetic drivers in PDAC mouse models [53–62], until a “next-generation” PDAC mouse model with the development of a dual recombinase-system was generated [52]. In these mice, the recombinase system consists of a *Cre/Lox* system and additional *Flp/Frt* recombinases, whereas the expression of *Flp* is under the pancreas specific *Pdx1* promoter. Therefore, *KRAS^{G12D}* (*FSF - KRAS^{G12D}*) and tamoxifen inducible FSF-R26$^{CAG\text{-}CreERT2}$ activation are specifically achieved in the pancreatic progenitors by deletion of the *Frt-Stop-Frt* (FSF) cassette by the *FLP* recombinase and the mice develop PanIN and gradually PDAC as described before [51,52]. The fact, that the Cre-recombinase is only activated by the administration of tamoxifen makes it possible, to additionally activate not only *floxed* reporter genes (like R26$^{mT/mG}$ in this case), but also timely activate potential therapeutic targets or further genetic drivers [63,64]. A recent multiomics study made use of these and previous [49] mouse models to characterize the evolution of PDAC on a transcriptomic, genomic, morphologic and histologic background and further explore the underlining molecular and morphological subtypes [37,65]. The main finding consisted of an increased gene dosage of the oncogenic gene *KRAS^{G12D}* in the more aggressive, metastatic, undifferentiated and mesenchymal subtype of PDAC. This amplification comes along with other genetic drivers, but

the dose increase of *KRAS*^{G12D} is absolutely necessary for an epithelial-to-mesenchymal transition. Mice classified to the C1 Cluster (mesenchymal subtype, higher *KRAS*^{G12D} gene dosage, undifferentiated histology) showed a significant reduced survival when compared to the other epithelial subtype clusters (C2a, b, c) (Fig. 3b). Summing up, the dosage of *KRAS* itself is a driver for PDAC progression, metastasis and a hallmark of the mesenchymal subtype, although additional mutations in tumour suppressor genes are necessary for tumour progression [37].

1.2 Protein Phosphatase 2A

1.2.1 Protein phosphorylation is regulated by kinases and phosphatases

Almost all proteins undergo protein post-translational modifications (PTM), not only on their way to formation, but even during their whole lifetime. This regulates protein activity, structure formation, charge, localisation or interactions with other proteins [66]. The PMTs include ubiquitination, glycosylation, methylation, acetylation, sumoylation, farnecylation or further protein modifications, but the most prominent and first described modification is a reversible protein phosphorylation [67]. Protein phosphorylation is accomplished by kinases and phosphatases and thereby regulates primarily the enzymatic activity of these proteins [67,68]. Whereas 539 different kinases are encoded in the human genome, only 189 protein phosphatases (ratio kinase/phosphatase 2.85) are known so far [69]. Phosphatases can be clustered into 20 different families, where more than half of them belong to the CC1 family (Cys-based Class, for example protein tyrosine phosphatases (PTP), PTEN or dual specificity phosphatase (DSP)). Serine/Threonine protein phosphatases are only found in a minor amount, but belong to the larger PPP-like subgroup (Phospho-protein phosphatase like), PPM family (metal-dependent protein phosphatases) or aspartate based (DXDXT/V) group and have basically the same conserved domains and motifs [69–71]. Examples for subfamilies of the PPP family are PP1, PP2A, PP2B (Calcineurin) or PP4 till PP7 [71] . Protein phosphorylation is mainly found on the amino acids serine (Ser, 86.4 %), threonine (Thr, 11.8 %) and in a minor amount on tyrosine (Tyr, 1.8 %) and mostly carried out (>90 %) by only two phosphatases of the PPP family: Protein phosphatase 1 (PP1) and Protein phosphatase 2A (PP2A) [68,71–73]. PP2A additionally accounts for almost 0.3-1 % of all cellular proteins and is therefore one of the most abundant and essential serine/threonine phosphatases in the cells which additional show a high conserved sequence homology between eukaryotes [71].

1.2.2 Structural composition and activation of PP2A

The majority of the PP2A holoenzymes form a trimeric structure, consisting of one connecting ~65 kDa structural (A), one ~36 kDa catalytic (C, PP2Ac) and one of various regulatory (B) units (Fig. 4a) [74]. For both, A and C domains, there exist two different isoforms α and β and although the two isoforms show a high sequence homology, the α-isoform of both is predominantly expressed [75,76]. The crystal structure reveals, that the structure resembles the catalytic domain of other Ser/Thr phosphatases (PP1 and PP2B, PP4 or PP6). In addition the C-terminal tail (AS 294-309, motif $TPDY_{307}$ FL_{309}) is conserved in these phosphatases and is required for both PP2A regulation and B unit binding [74]. In contrast to the structural and catalytic subunit, where only two isoforms exist, the regulatory subunits show great variability. So far, more than 20 isoforms of the B units are known, arising from different genes or gene splicing (Fig. 4b) [77]. They can be clustered based on sequence homology into the four major groups B (B55/PR55), B' (B56/PR61), B''(PR72/PR130/PR48/70/G5PR) and B'''(PR93/PR110). Among these, the B and B' family of proteins are much more evolutionary conserved [68,77,78]. The B subunits show tissue-specific expression, serve the substrate specificity of the PP2A holoenzyme complex and determine the physiological functions [79]. It is therefore obvious, that different variants of the protein phosphatase 2A are found in the cell and this mechanism explains, why less phosphatases in general can counteract the many kinase functions in protein phosphorylation regulation [71].

Because of the fact, that PP2A has a major role in diverse cellular functions, it has to be extremely regulated and therefore, PP2A must be activated before it exerts its function. As mentioned before, the activation of the catalytic subunit is necessary for formation of the trimeric holoenzyme and arises through methylation of the $PP2A_C$-tail [80]. Prior to activation, the regulatory α4 protein prevents nontarget dephosphorylation and additional stabilisation by binding the partially folded $PP2A_C$, inducing conformational changes that disturb the A-subunit binding site [81]. Also the α4 protein prevents $PP2A_C$ from ubiquitination through Midline 1 (MID1) and resulting degradation [82]. Altogether, this leads to an accumulation of potential $PP2A_C$ for the upcoming creation of trimeric holoenzymes. A decisive regulator for the activation of PP2A is the phosphotyrosyl phosphatase activator (PTPA), an ATP-dependent activation chaperone [83]. Together, $PP2A_C$ and PTPA form an ATP-binding pocket and catalyse ATP hydrolysis, which leads to an insertion of Mg^{2+} into the active site. In the end all of this leads to the activation of $PP2A_C$, whereupon $PP2A_C$ can bind to the structural unit $PP2A_A$ [76,83].The process of the B subunit binding to the AC dimer is again a highly regulated process involving post translational modifications like methylation and phosphorylation. For example methylation of the amino acid

Leu_{309} of $PP2A_C$ by S-adenosylmethionine-dependent leucine carboxyl transferase1 (LCMT1) was prerequisite for binding of PR55 family members to the catalytic domain and phosphorylation of the amino acid Tyr_{307} of $PP2A_C$ inhibits this binding [79,80,84,85]. In mammalian cells, both forms of PP2A (dimeric AC complex and trimeric ABC complex) could be found, but the dimeric shape makes only up to a third of the total PP2A holoenzymes in the cell [78,86]. In addition to the up to 80 different canonical complexes, a non-canonical PP2A complex lacking regulatory B subunits was described [87].

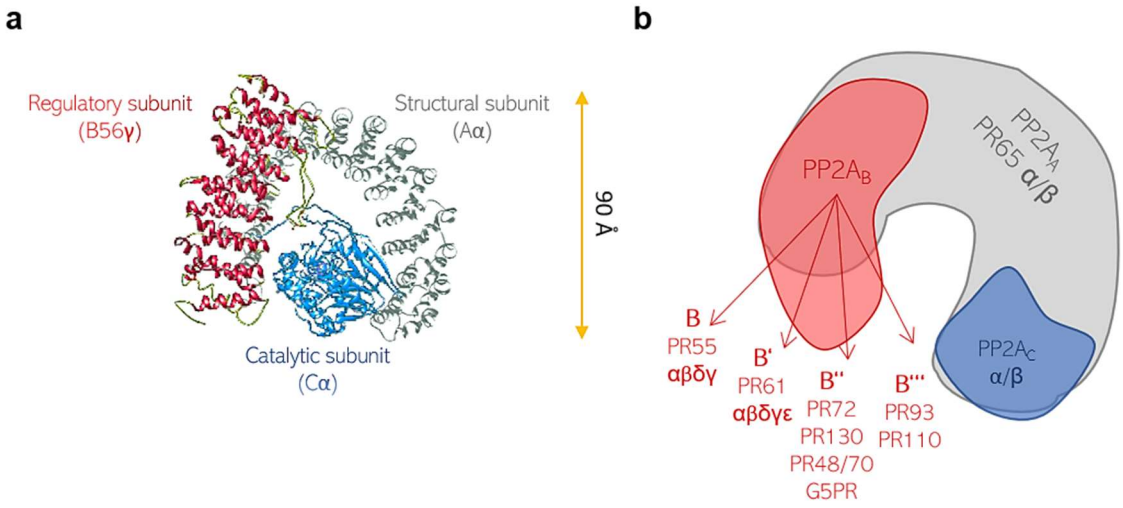

Figure 4 | Trimeric Structure of the Protein Phosphatase 2A

a, The Phosphatase Holoenzyme consists of three different subunits. Whereas the catalytic subunit (coloured in blue, Cα, ~36kDa) is necessary for the dephosphorylation event, the regulatory subunit (red, B56γ) determines the substrate specificity and also the cellular localisation of the protein. The Scaffolding/Structural subunit (grey, ~65 kDa) is formed like a horseshoe, holding the other subunits together. The overall size is about ~90 Â x 90 Â x 70 Â (crystal structure adapted from [74] using 2IAE (PDB) in UCSF Chimera 1.13.1) **b,** Only two isoforms (α & β) exist of the structural (A) and catalytic (C) subunit. The regulatory subunits can be clustered according to their sequence homology into four groups (B, B', B'' and B'''). More than 20 isoforms of the regulatory subunit are known so far. Figure created according to [88].

1.2.3 Function of PP2A as tumour suppressor and promoter

Belonging to the big family of phosphoprotein phosphatases, the protein phosphatase 2A has important and diverse cellular functions. PP2A is the crucial regulator of different physiological and cellular processes, including neuronal stabilization, cardiac muscle function, cell cycle, DNA replication, proliferation and apoptosis through formation of diverse heterotrimeric complexes after activation of $PP2A_C$ [76,83]. Further, PP2A can function as a cell metabolism controller, regulating the enzyme activity in glycolysis by

dephosphorylation, lipid metabolism and catecholamine synthesis by dephosphorylation [89]. Among all other functions, the regulation of normal cell division is a major role of the phosphatase. The PP2A regulation takes place during the G1/S transition to G2/M phase, mitotic spindle breakdown, chromatin decondensing, post-mitotic reassembly and is also found in the regulation of the mitotic exit. For the G1/S transition, the B56γ3 (PR61γ3)-containing PP2A complex is mainly found in the nucleus regulating the CDK inhibitor p27 protein for limiting cell proliferation [90]. The B55α-containing PP2A prevents G2/M phase transition by dephosphorylating the M phase-promoting factor MPF (Cdk1/cyclin B complex) and inhibiting of the Wee1 kinases [91]. Additionally, the complex consisting of PP2A/B56δ is necessary for mitotic exit and cell division; here PP2A/B56δ dephosphorylates the Cdc25 phosphatase which results in a hyperphosphorylation (inactivation) of the Cdk1 [91]. Moreover, PP2A can also directly phosphorylate MYC, preventing MYC from proteolytic degradation [92]. On the other hand, PP2A can also dephosphorylate MEK1 and ERK-family kinases, resulting in a decreasing stability and function of MYC or STAT5 and inhibition of mitogenic and anti-apoptotic signals [91]. PP2A can also be found in regulating pathways for pro-apoptotic stimuli and therefore gets into the role of the tumour suppressor. PP2A is able to directly phosphorylate Akt (negatively regulate PI3K/Akt pathway) and also phosphorylate the pro-apoptotic factor Bad, which translocate to the mitochondria and inhibits the anti-apoptotic function of Bcl-2 [93]. But there can also be found differences among the diverse subunits of PP2A. Whereas the stress-activated form PP2A-PR61/B'α dephosphorylates Ser70 of Bcl-2 which results in cell death, phosphorylation of Ser87 by a different PP2A holoenzyme promotes cell survival [93]. On one side it is therefore conclusive, that dysregulation of PP2A as a tumour suppressor can lead to several diseases like Alzheimer's disease, various autoimmune diseases, diabetes and cancer, PP2A activating drugs as a new treatment option are therefore an emerging field [94–97]. But to also underscore the tumour promoting functions of PP2A on the other side, PP2A inhibition has demonstrated enormous therapeutical potential already in cancer treatment [98,99].

1.2.3.1 Reactivation of PP2A tumour suppressor functions

In several diseases, PP2A was found to be inactivated by somatic mutations, phosphorylation or methylation of the $PP2A_c$ subunit or increased expression of the endogenous PP2A inhibitor protein SET or CIP2A (cancerous inhibitor of PP2A)[91,100]. The first hint for the predominantly tumour-suppressing functions of PP2A could be detected upon

application of the PP2A inhibitor okadaic acid in mice. Treatment of mice with this exogenous inhibitor leads to tumours on the skin, hinting to the tumour suppression and negative regulation of cellular growth of PP2A [101,102]. This thesis was also supported by the observation, that tumour-promoting viruses (like SV40) can displace the regulatory subunit and increases the cell proliferation and tumour development [71,103,104]. Another demonstration of PP2A as a tumour suppressor was achieved by the inhibition of the PP2A endogenous inhibitory proteins SET or CIP2A. FTY720 (Fingolimod/ Gilenya®) was shown to disturb the SET/PP2A interaction, leading to a reactivation of the phosphatase activity and apoptosis in different types of cancers, though mainly described for leukaemia's [91,96,105,106]. Decreased AKT and MYC gene expression led to a reduced cell proliferation and cancer progression. This was on one hand achieved by an agonist of PP2A methylation (Xylulose-5-phosphate, methylation of Leu_{309}) and a resulting higher affinity of the PP2A dimeric enzyme to its regulatory subunit [107,108], or on the other hand by CIP2A inhibition with Celasterol (tripterine) [109,110], the proteasome inhibitor Bortezomib [111,112] or derivates of the EGFR inhibitor Erlotinib [113], which leads to similar results and decreased tumour progression after PP2A activation. In non-small cell lung carcinoma (NSCLC), where hyperactivation of KRAS is often detectable, downregulation of CIP2A and simultaneous activation of PP2A sensitised the cells to different MAPK inhibitors, mainly by inhibiting MYC proliferation or other mechanisms of resistance [114,115]. Similar results were found in pancreatic cancer and T cell acute lymphoblastic leukaemia (T-ALL), where PP2A activators (Phenothiazine, Penfluridol) were found to sensitise cells to the inhibition with Dasatinib (SRC and BCR-ABL kinase inhibitor) or γ-secretase inhibitors, respectively [115–117]. Since PP2A is considered to have tumour suppression functions and was found to be inactivated in some types of cancers, PP2A activators in combination with other cancer inhibitors have the potential to inhibit tumorigenesis and have to be further investigated [115].

1.2.3.2 PP2A tumour promoting functions and inhibition as treatment option

Despite the quite well-known tumour suppressor function of PP2A, lots of studies also pointed to an adverse tumour promoting function of the phosphatase and therefore to its inhibition as a possible treatment option. One of the best examples could be demonstrated in the 5q-minus syndrome, a subtype of the myelodysplastic syndromes (MDS). This syndrome is characterised by a deletion of the 5q chromosome, ineffective erythropoiesis as well as an impaired haplodeficient $PP2A_C$ catalytic activity (due to location on 5q31.1 [118], HGNC: 9299). Treatment with Lenalidomide (Revlimid®, structural similar to

Thalidomide) resulted in the inhibition of the activity of $PP2A_c$, specifically in cells that carry the 5q- minus deletion and promoted cell cycle arrest and apoptosis. Further, Lenalidomide treatment led to a simultaneous stabilisation of MDM2, TP53 degradation and arrest in G2/M. Patients receiving this treatment option showed a significant overall survival, but despite that, they also acquired an over-expression of PP2A in most cases over treatment time which supported resistance to lenalidomide treatment [119–122]. In pancreatic cancer, a potent, but nonspecific PP2A inhibitor (Cantharidin) was also able to induce apoptosis and pro-apoptotic factors after PP2A inhibition. Activation of Caspase-8 and Caspase-9 together with TNF-alpha, TRAILR1, Bad, Bak and Bid was induced due to treatment, leading to G2/M cell cycle arrest and apoptosis [123]. Unfortunately, Cantharidin demonstrates strong side effects, which means, that it cannot be used any longer as a treatment option for patients. Analogues, like Norcatharidin or Demethylcantharidine, have less side effects and have also already demonstrated their effectiveness in different cancer models [122,124–128].

Summing up, PP2A therapy, either by activation or inhibition, can include two opposite functions depending on the tumour context and have to be further investigated in a deeply, context-specific manner [99].

1.3 LB-100 as a novel inhibitor of Protein Phosphatase 2A

1.3.1 LB-100 as a new phosphatase inhibitor

Kinases and phosphatases are the main regulators of all essential pathways in the cells and often the kinase itself is also regulated by dephosphorylation of a related phosphatase [129,130]. Since today, there are already 72 small molecules inhibitors of kinase activity approved by the FDA [131]. Six of them were solely approved in 2021 and, overall, kinases became the most important drug target of the 21st century [132,133].

On the other side, only about 10 inhibitors that target phosphatase activity are under clinical investigation for cancer treatment [134,135]. One of the most promising of them is a cantharidin analogue, the small water-soluble inhibitor LB-100 (Fig. 5a) and its lipid-soluble homolog LB-102, that target the Protein Phosphatase 2A catalytic subunit even at low micromolar concentrations and with less side effects [122,136–139]. In many preclinical *in vitro* and *in vivo* studies, the effectiveness could already be demonstrated. The first study of LB-100 was conducted for therapeutic targeting of glioblastoma and demonstrated that PP2A-inhibition by LB-100 led to phosphorylated Akt1 followed by nuclear

exportation of the N-CoR complex and therefore cellular differentiation of cancer stem cells [140,141]. The same group also carried out a study with LB-102 in glioblastoma and neuroblastoma xenografts. Here it could be demonstrated that drug administration of LB-102 activated polo-like kinase (Plk-1) and protein kinase B (Akt-1) and decreased TP53 expression, leading to apoptosis and blocking of cell cycle arrest. Additionally, LB-102 enhanced the effectiveness of other compounds (Temozolomide and Doxorubicin) as a chemo-sensitiser [138,141] . In the same year, Zhang et al. could demonstrate similar findings in murine mesenchymal stem cells of fibrosarcoma. Here, LB-100 also enhanced Doxorubicin, leading to a mitotic catastrophe, so therefore it enhanced the effectiveness of DNA-damage inducing chemotherapeutics [141,142]. The same could be demonstrated by Bai XL et al. in a hepatocellular carcinoma (HCC) tumour model. LB-100 alone did not alter the cell viability up to 5 µM, but a mitotic catastrophe could still be detected after treatment. Additionally, it potentiated standard-of-care agents for treatment of HCC, like Doxorubicin or Cisplatin by upregulating HIF-1a, promoting VEGF secretion and therefore increased the tumour angiogenesis and perfusion *in vivo*. LB-100 was hence described as chemo-sensitiser by upregulation of vascular permeability of other agents [141,143]. The same enhanced blood perfusion could also be shown for pancreatic cancer cell lines, when treated with LB-100 [144]. Additionally, a radio-sensitisation function of LB-100 could also be demonstrated for treating pancreatic cancer: the depletion of PPP2R1A inhibited the homologous recombination repair (HRR), activated CDK1/CDC25C and therefore lead to an accumulation of radiation-induced DNA damage [141,145]. Taken together, all these preclinical studies could demonstrate the effectiveness of LB-100 as an anti-cancer drug and chemo- and radio-sensitiser *in vitro* and *in vivo*.

1.3.2 Phase I clinical trial of LB-100

To test the possible clinical application of LB-100 as a therapeutic agent, a first human clinical trial was carried out for different relapsed solid tumours to determine the safety, maximum tolerated dose (MTD) and activity of LB-100 for further combination therapies [137]. The study was accomplished by treatment with LB-100 in a seven-dose escalation (0.25, 0.50, 0.83, 1.25, 1.75, 2.33, and 3.1 mg/m^2) over 3 consecutive days in a three-week cycle in 29 adult patients with advanced solid tumours, who failed to respond to standard treatment options. In this study, a MTD of 2.33 mg/m^2 was determined, although a low maximal plasma concentration (max. 34.7 ng/ml) and endothall were detected and comparable after day 1 and 3 of treatment [137]. The drug administration

showed different responses within the different solid tumour entities. Whereas an unexpected significant increase in tumour size could be detected in patients with duodenal and colonic adenocarcinoma, the rest of the patients (16) showed a cessation of the tumour (Fig. 5b). The only partial response to LB-100 (>30 % of maximum change in lesion size) could be detected in a patient with pancreatic cancer. Summed up, 50 % of the patients tolerated at least 2 cycles of LB-100 and their disease remained stable up to 15 cycles and the toxicity was low and comparable to the phase I trial of Fostriecin, another PP2A inhibitor [137,146]. Additionally, toxicity determined by animal studies in dogs and rats showed some haematuria and histological changes in the renal tubes and preclinical PP2A inhibition in xenografts showed a full recovery of PP2A occurring after only 24 hours [137,147,148]. Further Phase 1b/2 clinical trials of LB-100 for specific tumour entities are running at the moment (NCT03886662 for 5q- MDS syndrome, NCT04560972 for small cell lung cancer in combination with carboplatin/etoposide/atezolizumab, NCT03027388 for glioblastoma multiforme in combination with temozolomide) [149].

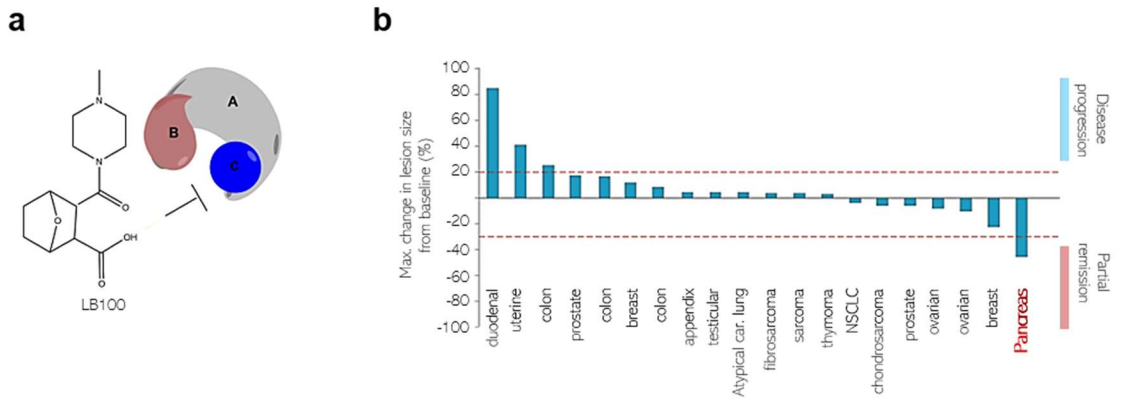

Figure 5 | LB-100 as a novel inhibitor of Protein phosphatase 2A

a, Chemical structure of LB-100, targeting the catalytical subunit of the protein phosphatase 2A. Figure according to [136,139]. **b,** Results from the Phase 1 clinical trial from LB-100. Represented are the max change in lesions size (%) from the different solid tumour patients. The only partial remission could be detected in a patient with pancreatic tumour. Figure adapted from [137].

1.4 Aim of this thesis

The high failure rate of a drug, from deciphering to clinical implementation and its adverse side effects, highlights the need for investigating drug-responses context-specifically. LB-100 was already demonstrated to have clinical value, but the mechanism of actions and context or subtype specificity remain low and have to be further investigated. With this work, using different cellular models and also pre-clinically patient-derived 3D-organoids, the mechanism of action of LB-100 and detailed molecular understanding will be further investigated in a context-and subtype specificity of PDAC and this work will shed light on why $PP2A_C$ is a high evident target in PDAC patients. The results of this thesis will help to further understand the mechanism of action of LB-100, provide evidence for a specific therapy option of pancreatic cancer and help to further investigate in PP2A-inhibitor based therapy options, either as single or synergistical rational combination therapies.

2 Materials

2.1 Technical equipment

Table 1 | Technical equipment with supplier information

Name	Supplier
Agarose Gel Chamber Compact L/XL	Biometra, Jena
AS2000 Maxwell® 16 instrument	Promega, Walldorf
Autoclave DX-45	Systec, Linden
Axiovert 25 Cell culture microscope	Zeiss, Jena
Cell culture Safety Cabinet HS18/21010942	Heraeus instruments, Hanau
Centrifuge 5415R	Eppendorf, Hamburg
CO2-Incubator NB-203XL	n-biotech, Korea
Electrophoresis Power supply EP5601	Amersham pharmingen, UK
FluoStar Optima Microplate Reader	BMG Labtech, Ortenberg
Gallios™ Flow Cytometer	Beckman Coulter, USA
Glass ware, Schott Duran	Schott AG, Mainz
Incubator B6 50042301	Heraeus instruments, Hanau
Inolab pH 720	WTW, Weilheim
Magnetic stirrer Ikamag RCT	IKA Werke, Staufen
Microwave	Siemens, Munich
Mini Protean Tetra System	BioRad, Munich
Multipipette E3X	Eppendorf, Hamburg
Multiscan FC Microplate Reader 51119000	Thermo Fisher, Munich
Neubauer counting chamber 10490171	Thermo Fisher, Munich
Odyssey XF Imaging system 2800	LI-COR Bioscience, USA
PCR Machine Tpersonal	Biometra, Gottingen
Pipettes Research plus	Eppendorf, Hamburg
Pipetus®	Hirschmann Laborgeräte, Eberstadt
Rotina 46R	Hettich Zentrifugen, Tuttlingen
Scales BP610	Sartorius, Goettingen
SP8 LIGHTENING Confocal	Leica, UK
Spectrophotometer NanoDrop 1000	Peqlab Biotechnologie, Erlangen
Thermal Cycler T100 621BR22596	BioRad, Munich

Thermomixer compact	Eppendorf, Hamburg
Thermoshaker	C.Gerhardt, Königswinter
UV Solo TS Imaging system	Biometra, Jena
Vorte× genius 3	IKA Werke, Staufen
Water bath 1003	GFL, Burgwedel
Welding machine	Severin, Sundern

2.2 Disposables

Table 2 | Disposables with supplier information

Name	Cat. Number	Supplier
24-well Polypropylene Microplates	142475	Corning, USA
384-well White/Clear Bottom Plates	3765	Corning, USA
5ml Polystyrene Round Bottom Tubes	352008	Corning, USA
96 well Costar Plate white bottom	3903	Corning, USA
96-well plates	353072	Corning, USA
Cell Scraper	83.1830	Sarstedt, Germany
CellStar Serologische Pipetten 5,10,25,50 ml		Greiner Bio-one, Austria
CELLSTAR®Polypropylen Röhrchen	227261	Greiner Bio-one, Austria
Combitips BioPur		Eppendorf, Hamburg
Costar® TC-Treated 6-well Plate	CLS3516	Corning, USA
Falcon 15mL Conical Centrifuge Tubes		Sarstedt, Nuremberg
Falcon 50mL Conical Centrifuge Tubes		Sarstedt, Nuremberg
Falcon™ Chambered Culture Slides	10364551	Thermo Fisher, Munich
Gel Saver-Tip II	GSII054R	Kisker Biotech, Steinfurt
Microplate PCR-96-LP-AB-C		Axygen / Corning, USA
Pipette tips		Sarstedt, Nuremberg
Platemax CyclerSeal Sealing Film		Axygen/Corning, USA
Protran 0.2µM Nitrocellulose Membrane	10600001	Amersham, UK
Safe-Lock Tubes, 1.5 mL	0030120086	Eppendorf, Hamburg

Safe-Lock Tubes, 2mL	0030120094	Eppendorf, Hamburg
Seahorse XFe96 Flux Pak	102416-100	Agilent Technologies, USA
Single use needles Sterican		B. Braun, Melsungen
Single use syringes Omnifix		B. Braun, Melsungen
Superfrost Plus Menzel Gläser		Thermo Fisher, Munich

2.3 Chemicals, Reagents and Buffer

2.3.1 Chemicals

Table 3 | Chemicals with supplier information

Name	Cat. Number	Supplier
16 % Formaldehyde Solution	28906	Thermo Fisher, Munich
80 % Ethanol Alkopharm 80	2109.98.99	Brüggemann, Heilbronn
Agarose	A9539	Sigma-Aldrich, Munich
Ammonium persulfate	A3678	Sigma-Aldrich, Munich
Ampicillin	11593027	Thermo Fisher, Munich
Bovine serum albumin	11930.03	Serva, Heidelberg
Bradford solution, 5×	39222.03	Serva, Heidelberg
Crystal Violet	C61158	Sigma-Aldrich, Munich
Dimethylsulfoxid	41640	Sigma-Aldrich, Munich
Dulbecco Phosphate Buffered Saline	56064C	Sigma-Aldrich, Munich
Glycerine	3783.1	Carl Roth, Karlsruhe
LB-Agar	X969.2	Carl Roth, Karlsruhe
LB-media	X968.1	Carl Roth, Karlsruhe
Methanol	46275	Carl Roth, Karlsruhe
Milk powder, Blotting grade,	T145.3	Carl Roth, Karlsruhe
MTT	M6494	Invitrogen, USA
PageRuler Prestained	26616	Thermo Fisher, Munich
Polybrene Transfection Reagent	TR-1003	Sigma-Aldrich, Munich
Polyethylengylcol	4000 95904	Fluka, Seelze
Propidium iodide	P4170	Sigma-Aldrich, Munich
PureLink RNAseq	12091-021	Invitrogen, USA
Rotiphorese Gel 30	30291	Carl Roth, Karlsruhe

Sodium Azide	S2002	Sigma-Aldrich, Munich
Sodium chloride	P029.2	Carl Roth, Karlsruhe
Sodium dodecyl sulfate	190072	Serva, Heidelberg
T4 DNA Ligase	M0202S	New England Biolabs, Frankfort-on-the-Main
T4 DNA Ligase Reaction Buffer	B0202S	New England Biolabs, Frankfort-on-the-Main
TEMED	2367.1	Carl Roth, Karlsruhe
Triton X100	T6878	Sigma- Aldrich, Munich
Tween20	9127	Carl Roth, Karlsruhe
Vectashiel Hardset mounting media with DAPI	H-1500	Vector Laboratories, USA

2.3.2 Inhibitors

Table 4 | Inhibitors with supplier information

Name	Cat. Number	Supplier
2-Desoxy-D-Glucose	CN96.3	Carl Roth, Karlsruhe
Antimycin A	A8674	Sigma-Aldrich, Munich
Bortezomib	5043140001	Sigma-Aldrich, Munich
Chloroquine diphosphate	C6628-25G	Sigma-Aldrich, Munich
Cycloheximide	S7418	Selleckchem, USA
FCCP	S8276	Selleckchem, USA
Indisulam	S9742	Selleckchem, USA
JNJ-64619178	S8624	Selleckchem, USA
LB-100	S7537	Selleckchem, USA
Oligomycin A	S1478	Selleckchem, USA
P276-00	S8058	Selleckchem, USA
Phenanthrolindion (Phendione)	496383	Sigma-Aldrich, Munich
Phosphatase Inhibitor Mix I	39050.01	Serva, Heidelberg
Protac CDK9 Degrader-1	HY-103628	MedChemExpress, USA
Protease Inhibitor complete	11873580001	Roche, Basle
Rotenone	S2348	Selleckchem, USA

SB-1317	S7002	Selleckchem, USA

2.3.3 Cell culture reagents and media

Table 5 | Cell culture reagents and media with supplier information

Name	Cat. Number	Supplier
3,3,5-Triiodo-L-Thyronine	T0821	Sigma-Aldrich, Munich
A83-01	2939	Tocris, UK
Advanced DMEM F12	12634-010	Life Technologies, USA
Bovine Pituitary Extract	P1167	Sigma-Aldrich, Munich
Cholera Toxin	C9903	Sigma-Aldrich, Munich
Dexamethasone	D1756	Sigma-Aldrich, Munich
D-Glucose	G8270	Sigma-Aldrich, Munich
DMEM-F12	11320033	Thermo Fisher, Munich
Dulbecco's Modified Eagle Media (DMEM)	D5796	Sigma-Aldrich, Munich
Dulbecco's Phosphate Buffered Saline (PBS)	D8537	Sigma-Aldrich, Munich
Fetal calf serum, cell culture grade	F0804	Sigma-Aldrich, Munich
ITS Premix	354350	Fisher Scientific
Nicotinamide	N3376	Sigma-Aldrich, Munich
NU-Serum IV	355500	Fisher Scientific
Opti-MEM+GlutaMax	51985-042	Life Technologies, USA
Penicillin Streptomycin	15140-122	Life Technologies, USA
Primocin	ant-pm05	Invitrogen, Karlsruhe
Recombinant Human Heregulin-1	100-03	Peprotech
Roswell Park Memorial Institute 1640 Media (RPMI)	61870-010	Life Technologies, USA
Seahorse XF DMEM Base Medium	103334-100	Agilent Technologies, USA
Trypsin-EDTA, 10×	LCF9012	Sigma-Aldrich, Munich

2.3.4 Cell culture media composition

Table 6 | Cell culture media composition

Name	Composition
Culture media (Murine & Human)	DMEM or RPMI, 10 % FCS, 1 % P/S
Freezing media	DMEM/RPMI, 20 % FCS, 10 % DMSO
Patient derived cell lines	Adv.DMEM F12, 20 % FCS, 1 % P/S
PDO-drug screen media	Matrigel 1:9 normal growth media, 10 µM Y-27632
PDO culture growth media	DMEM-F12, 5mg/ml D-Glucose, 0.5 % ITS Premix, 5nM 3,3,5-Triiodo-L-Thyronine, 1µM Dexamethasone, 100ng/ml Cholera Toxin, 1 % Pen/Strep, 5 % NU Serum IV, 25µg/ml Bovine Pituitary Extract, 10mM Nicotinamide, 100 µg/ml Primocin, 0.5 µM A83-01, 10 % RSPO1-conditioned media (R-spondin-1 overexpressing cell line HEK293FT, provided by the Hubrecht Institute (Uppsalalaan 8, 3584 CT Utrecht, Netherlands), 100 ng/ml Recombinant Human Heregulin-1

2.3.5 Buffer composition

Table 7 | Buffer compositions

Name	Composition
50× Tris acetate EDTA (TAE) buffer	2 M Tris, 50 mM EDTA, 5.71 % Acetic acid, pH 8.5
5× Protein loading buffer (Laemmli)	250 mM Tris-HCl (pH 6.8), 4 % (w/v) SDS, 40 % (v/v) Glycerol, 0.05 % (w/v) Bromphenolblue add 5 % (v/v) ß-Mercaptoethanol before usage
Blocking Buffer	5 % milk powder, 0.1 % Tween in TBS
KCM Buffer (5×)	0.5 M KCl, 0.15 M MCaCl2, 0.25 mL MgCl2
LB-Agar	4 % (w/v) LB-Agar in H_2O
LB-Medium	2.5 % (v/v) LB-Medium in H_2O
PBS (1×)	137 mM Sodium chloride, 270 µM Kalium chloride, 4.0 mM Disodium phosphate
Proteomics lysis buffer	2 % (v/v) SDC, 100mM Tris-HCL, pH 8.5
RIPA Buffer	50 mM Tris-HCl, 50 mM NaCl, 2 mM EDTA, 1 % (v/v) Triton X100, 1 % Sodium deoxycholate (w/v), 0.1 % (w/v) SDS, supplemented freshly with 1 x phosphatase Inhibitor Mix I and 1 x Protease complete Inhibitor cocktail
Running buffer 10×	25 mM Tris, 192 mM Glycine, 3.47 mM SDS
Separating gel (7.5 %, 10 %, 15 %)	390 mM Tris adjusted to pH 8.8 with HCl, 7.5 % (v/v) / 10 % (v/v) / 15 % (v/v) Acrylamide, 0.1 % (v/v) SDS, 0.05 % (v/v) APS, 0.05 % (v/v) TEMED
Stacking gel	125 mM Tris adjusted to pH 6.8 with HCl, 4.4 % (v/v) Acrylamide, 0.1 % (v/v) SDS, 0.05 % (v(v) APS, 0.2 % (v/v) TEMED
SOC media	2 % (w/v) Tryptone, 0.5 % (w/v) Yeast extract, 0.05 % (w/v) NaCl
Transfer buffer	25 mM Tris, 192 mM Glycine, 20 % (v/v) Methanol, pH 8.3

TSB-Buffer	10 % PEG4000, 5 % DMSO, 10 mM $MgCl_2$, 10 mM $MgSO_4$, LB Broth (pH 6,1) to 100 ml

2.4 Antibodies

2.4.1 Primary antibodies

Table 8 | Primary antibodies with dilution, RRID numbers and supplier information

Name, Host species, Cat. number	Dilution	RRID Number	Supplier
AMPK alpha, rabbit, #5832S	1:1000	RRID: AB_10624867	Cell Signalling, USA
ATF4, rabbit, #11815S	1:1000	RRID: AB_2616025	Cell Signalling, USA
ATF6, rabbit, #65880S	1:1000	RRID: AB_2799696	Cell Signaling, USA
a-Tubulin (T5168), mouse, #89494	1:2000	RRID: AB_477579	Sigma-Aldrich, Munich
Bak NT, rabbit, #06-536	1:1000	RRID: AB_310159	Sigma-Aldrich, Munich
BiP (C50B12), rabbit, #3177S	1:500	RRID: AB_2119845	Cell Signaling, USA
CDK9, rabbit, #32038		RRID: AB_2799017	Cell Signaling, USA
E-cadherin (H108), rabbit, #sc-7870	1:1000	RRID: AB_2076666	Santa Cruz, USA
eIF2alpha, rabbit, #9722S	1:1000	RRID: AB_2230924	Cell Signaling, USA
GATA-6 (H-92), rabbit, #sc-9055	1:1000	RRID: AB_2108768	Santa Cruz, USA
HSP90 alpha/beta (F8), mouse, #sc13119	1:2000	RRID: AB_675659	Santa Cruz, USA
INTS9, rabbit, #13945	1:1000	RRID: AB_2798351	Cell Signaling, USA
IRE1, rabbit, #ab48187	1:1000	RRID: AB_873899	Abcam, UK
Kap1 (A4), rabbit, #NB500-158	1:1000	RRID: AB_2256671	Novusbio, USA
LC3A/B, rabbit, #4108S	1:1000	RRID: AB_2137703	Cell Signaling, USA
mTOR, rabbit, #2972S	1:1000	RRID: AB_2799696	Cell Signaling, USA
p44/42 MAPK (ERK1/2), rabbit, #4695S	1:1000	RRID: AB_390779	Cell Signaling, USA
p-AMPK alpha, rabbit, #2535S	1:1000	RRID: AB_331250	Cell Signaling, USA
p-CDK9, rabbit, #2549	1:1000	RRID: AB_2077300	Cell Signaling, USA

p-eIF2 alpha (S51), rabbit, #3398S	1:1000	RRID: AB_2096481	Cell Signaling, USA
p-Kap1 (Ser824, A5), rabbit, #NB100-2350	1:2000	RRID: AB_10002723	Novusbio, USA
p-mTor, rabbit, #2976S	1:1000	RRID: AB_490932	Cell Signaling, USA
PP2A A subunit, rabbit, #2039	1:1000	RRID: AB_490763	Cell Signaling, USA
p-PP1 alpha (Thr320), rabbit, #2581	1:1000	RRID: AB_330823	Cell Signaling, USA
PPP1 alpha, rabbit, #2582	1:1000	RRID: AB_330822	Cell Signaling, USA
p-S2 RNA Pol II CTD repeat, rabbit, #ab5095	1:1000	RRID: AB_304749	Abcam, UK
p-S5 RNA Pol II CTD repeat, rabbit, # ab5131	1:1000	RRID: AB_449369	Abcam, UK
p-ULK1 (S757), rabbit, #6888S	1:1000	RRID: AB_10829226	Cell Signaling, USA
Puromycin (12D10)-AF647, mouse, #MABE343-AF647	1:1000	RRID: AB_10829226	Sigma-Aldrich, Munich
RNA polymerase II, rabbit, #ab264350	1:1000		Abcam, UK
TIA-1, goat, #sc-1751	1:1000	RRID: AB_2201433	Santa Cruz, USA
ULK1, rabbit, #8054S	1:1000	RRID: AB_11178668	Cell Signaling, USA
Vimentin, rabbit, #5741S	1:1000	RRID: AB_10695459	Cell Signaling, USA
β-Actin, mouse, #A5316	1:2000	RRID: AB_476743	Sigma-Aldrich, Munich

2.4.2 Secondary antibodies

Table 9 | Secondary antibodies with dilution, RRID numbers and supplier information

Name, Host species, Cat. number	Dilution	RRID Number	Supplier
AlexaFluor 647 goat anti-rabbit, #A21244	1:1000	RRID: AB_2535812	Invitrogen, Karlsruhe
Anti-Goat IgG 800, #SA5-10092	1:10.000	RRID: AB_2556672	Invitrogen, Karlsruhe
Anti-mouse IgG 680, #5470S	1:10.000	RRID: AB_10696895	Cell Signaling, USA
Anti-mouse IgG 800, #5257S	1:10.000	RRID: AB_10693543	Cell Signaling, USA
Anti-rabbit IgG 680, #5366S	1:10.000	RRID: AB_10693812	Cell Signaling, USA
Anti-rabbit IgG 800, #5151S	1:10.000	RRID: AB_10697505	Cell Signaling, USA
HRP Goat anti-mouse IgG, #926-80010	1:10.000	RRID: AB_2721263	LI-COR Bioscience, UK
HRP Goat anti-rabbit IgG, #926-80011	1:10.000	RRID: AB_2721264	LI-COR Bioscience, UK

2.5 Primers

2.5.1 Mycoplasma test primer

Table 10 | Sequence of mycoplasma test primers

Name	Sequence
Forward 5’ Primer	CGC CTG AGT AGT ACG TTC GC TGC CTG GGT AGT ACA TTC GC TGC CTG AGT AGT ACA TTC GC CGC CTG AGT AGT ATG CTC GC CAC CTG AGT AGT ATG CTC GC CGC CTG GGT AGT ACA TTC GC
Reverse 3’ Primer	GCG GTG TGT ACA AGA CCC GA GCG GTG TGT ACA AAA CCC GA GCG GTG TGT ACA AAC CCC GA

2.5.2 NGS sequencing primers of amplified library (CRISPR dropout screen)

Table 11 | Sequence of NGS-primers for **BRIE library**

Name	Sequence
sgRNA_NGS-P503	AATGATACGGCGACCACCGAGATCTACAC-tatcctCACCGACTCGGTGCCACTTTT
sgRNA_NGS-P504	AATGATACGGCGACCACCGA-GATCTACACagagtaCAC-CGACTCGGTGCCACTTTT
sgRNA_NGS-P506	AATGATACGGCGACCACCGA-GATCTACACactgcaCAC-CGACTCGGTGCCACTTTT
sgRNA_NGS-P701	CAAGCAGAAGACGGCATACGA-GATgccttaTTTCTTGGGTAGTTTGCAGTTTT
sgRNA_NGS-P702	CAAGCAGAAGACGGCATACGAGATagtac-gTTTCTTGGGTAGTTTGCAGTTTT
sgRNA_NGS-P703	CAAGCAGAAGACGGCATACGA-GATctgcctTTTCTTGGGTAGTTTGCAGTTTT

2.6 Plasmids

Table 12 | Plasmids with catalogue and RRID number with supplier information

Name	Cat. Number	RRID	Supplier
Human CRISPR knockout pooled library (Brunello)	73178	RRID: Addgene_73178	Addgene, USA
Lenti-Cas9-2A-Blast	73310	RRID: Addgene_73310	Addgene, USA
lentiGuide-Puro	52963	RRID: Addgene_52963	Addgene, USA
Mouse CRISPR Knockout pooled library (Brie)	73633	RRID: Addgene_73633	Addgene, USA

pMD2.G	12259	RRID: Addgene_12259	Addgene, USA
psPAX2	12260	RRID: Addgene_12260	Addgene, USA

2.7 Cell Lines

2.7.1 Prokaryotic cell lines

Table 13 | Prokaryotic cell lines with supplier information

Name	Cat. Number	Supplier
One Shot™ Stbl3™ Chemically, Competent E. coli	C737303	Thermo Fisher, Munich
Endura™ competent cells	71003	VWR, USA

2.7.2 Eukaryotic cell lines

2.7.2.1 Murine PDAC cell lines

All 38 murine *KRAS*^{G12D} cell lines were provided by Prof. Dr. Dieter Saur, TranslaTUM, Munich[37]. Shown are here only the genotypes of the most used murine cell lines.

Table 14 | Selected murine genotypes

Name	Cluster	*Cdkn2a* deletion	Genomic *KRAS* status	Histological grade
PPT-8248	C1	complete	CN-LOH	Undifferentiated
PPT-3250	C1	complete	heterozygote	Undifferentiated
PPT-8296	C2c	partial	heterozygote	G1
PPT-9591	C2b	complete	CN-LOH	G2

2.7.2.2 Human conventional PDAC cell lines

Authentication of all human conventional cell lines was performed in 2020 by short tandem repeat (STR) profiling (Mycrosynth, Balgach, Switzerland) or single Nucleotide Polymorphism (SNP)-Profiling by Multiplexion (Multiplexion GmbH, Heidelberg, Germany) [150].

Table 15 | Human conventional PDAC cell lines with culture collection information

Name	RRID Number	Culture collection
AsPC-1	RRID: CVCL_0152	ATCC, USA
HEK293FT	RRID: CVCL_6911	ATCC; USA
HPAC	RRID: CVCL_3517	ATCC; USA
HuP-T3	RRID: CVCL_1299	DSMZ, Leibniz Institute, Germany
HuP-T4	RRID: CVCL_1300	DSMZ Leibniz Institute, Germany
MIA PaCa-2	RRID: CVCL_0428	ATCC, USA
PANC 05.04	RRID: CVCL_1637	ATCC, USA
PaTu 8889S	RRID: CVCL_1846	Provided by Prof. Ellenrieder

2.7.2.3 Patient derived PDAC cell lines

Authentication of all patient derived cell lines was performed in 08/2022 by short tandem repeat (STR) profiling by Multiplexion (Multiplexion GmbH, Heidelberg, Germany).

Table 16 | Human patient derived PDAC cell lines with culture collection information

Name	RRID Number	Culture collection
B211		Provided by Prof. Dieter Saur
huPDAC11		Provided by Prof. Dieter Saur
huPDAC17		Provided by Prof. Dieter Saur
PaCaDD-119	RRID: CVCL_1848	DSMZ Leibniz Institute, Germany

PaCaDD-135	RRID: CVCL_1849	DSMZ Leibniz Institute, Germany
PaCaDD-137	RRID: CVCL_1850	DSMZ Leibniz Institute, Germany
PaCaDD-159	RRID: CVCL_M465	DSMZ Leibniz Institute, Germany
PaCaDD-161	RRID: CVCL_M466	DSMZ Leibniz Institute, Germany
PaCaDD-165	RRID: CVCL_M467	DSMZ Leibniz Institute, Germany
PDC117		Provided by PD Dr. Bo Kong
PDC40		Provided by PD Dr. Bo Kong
PDC49		Provided by PD Dr. Bo Kong
PDC56		Provided by PD Dr. Bo Kong

2.8 Commercially available kits

Table 17 | Commercially available kits with supplier information

Name	Cat. Number	RRID	Supplier
Blood & Cell culture DNA Maxi Kit	13362		Qiagen, Hilden
CellTiter-Glo® Luminescent Cell Viability Assay	G7570		Promega, Walldorf
Click-IT HPG Alexa594 protein synthesis assay	C10429		Invitrogen, USA
FITC Annexin V Apoptosis Detection Kit I (RUO)	556547	RRID: AB_2869082	Becton Dickinson, USA
Lipofectamine 3000 Transfection Kit	1923064		Invitrogen, USA
Maxwell® 16 LEV simplyRNA	AS1280		Promega, Walldorf
NucleoSpin Gel and PCR clean up	740609.250		Machery-Nagel, Duren

NucleoSpin Plasmid	740588.250	Macherey-Nagel, Duren
Purelink HiPure Plasmid Midiprep	8110225	Qiagen, Hilden

2.9 Software

Table 18 | Software with supplier information

Name	RRID	Supplier
FlowJo software	RRID:SCR_008520	FlowJo, USA
GraphPad Prism 9	RRID:SCR_002798	GraphPad Software, USA
Image studio Lite Version	RRID:SCR_013715	LI-COR Bioscience, UK
NanoDrop ND-1000 3.1		NanoDrop, Informer Technologies
R / R studio software	RRID:SCR_000432	R Core Team, GNU GPL
Windows Office 2019		Microsoft, USA

3 Methods

3.1 Protein biochemistry techniques

3.1.1 Isolation and concentration measurement by Bradford from whole cell lysates

To analyse changes in protein expression of untreated and treated cells, the cells have to be first lysed and the protein extracted. For this, 1.8×10^6 cells were seeded in 10 cm plates in 5 ml of media one day prior to treatment. The next day, LB-100 treatment was carried out as indicated, without media change. After treatment, the media was removed, the cells were washed one time with PBS and afterwards trypsinised for 3 minutes. Because lot of cells were already dead after the incubation periods, the media and solution of the washing step were collected and centrifuged together with the trypsinised cells for 5 min, 1000 × g, 4 °C. The supernatant was removed and the cell pellet lysed with 50 µl of cold RIPA buffer before storage at -80 °C (see buffer composition 2.3.5). Prior to use, the lysate was centrifuged in a precooled centrifuge (16.000 × g, 15 min, 4 °C) to remove cellular debris. To determine the protein concentration of the supernatant, a Bradford assay was done in triplicates [151]. For this, 1 µl of the supernatant was added to 300 µl of 1× Bradford solution in a 96-well plate, mixed well and afterwards the absorption was measured at 595 nM on the Multiscan RC Microplate Reader. For reference, a standard curve with defined concentrations of BCA was made. To bring all samples to equal protein amounts and charge the proteins negatively, each sample was adjusted with the addition of 5× Laemmli buffer [152] and water before boiling for 5 minutes at 95 °C to denature all proteins. Samples were then stored at -20 °C before further processing.

3.1.2 SDS-gel electrophoresis

To separate the proteins depending on their molecular weight, a SDS gel electrophoresis[153] was accomplished with the protein samples. To analyse high (100-300 kDa), middle (40-130 kDa) or small molecular weight proteins (10-40 kDa) a 7.5 %, 10 % or a 15 % separation gel with a thickness of 1.5 mm was used, respectively. On top of the separation gel, a stacking gel was placed. The compositions of the separation and stacking gel are listed in table 18. After polymerisation, 50 µg of protein sample were loaded simultaneously with a prestained standard protein ladder (PageRuler®) into the pockets and the proteins were separated for 3 hours at 80 V in 1× SDS running buffer.

Table 19 | SDS-gel buffer composition

Separation gel 2×				Stacking gel 2×
Composition	**7.5 %**	**10 %**	**15 %**	4.5 ml
H_2O	7.35 ml	6.15 ml	3.75 ml	
Stacking buffer				1.95 ml
Separation buffer	3.9 ml	3.9 ml	3.9 ml	
Rotiphorese® Gel30	3.75 ml	4.95 ml	7.5ml	1.125 ml
10 % SDS	150 µl	150 µl	150 µl	75 µl
10 % APS	75 µl	75 µl	75 µl	37.5 µl
TEMED	22.5 µl	22.5 µl	22.5 µl	15 µl

3.1.3 Immunoblotting by Western Blot

To visualize the protein of interest, the linearised proteins first had to be transferred to a nitrocellulose or PDVF membrane by electrophoresis. This wet transfer was carried out for either 1.5 hrs at 350 mA or overnight at 90 mA at 4 °C. Afterwards, the membrane was blocked with 5 % milk in TBS-T for at least one hour at room temperature to avoid unspecific binding before incubating with the first antibody at indicated concentrations overnight at 4 °C. The next day, the membrane was washed three times for five minutes each in TBS-T while gently shaking it and afterwards incubated with the secondary antibody (DyLight 680 or 800, 1:10.000) for one hour at room temperature. After washing the membrane again with TBS-T three times, the proteins were detected with the Odyssey® FC imaging system (Licor, Germany) and the signal intensity was calculated with the Image Studio Light Software.

3.1.4 SUnSET Assay: Measuring Protein Translation

For measuring protein synthesis, the SUnSET Assay was performed [154]. In this assay, puromycin will be incorporated into newly translated proteins due to its structural similarity to tyrosyl-tRNA. Puromycin can later be detected using an anti-puromycin antibody. For this, cells were seeded in 10 cm plates at a density of 1.7 x 10^6 cells in 5 ml media. After 24 hrs, the cells were treated as indicated (LB-100 at 20 µM for different time periods and Cyclohexamide as a negative control for one hour at 20 µM). When the incubation times were completed, the media was aspirated and the cells washed once with PBS

before incubating the cells with puromycin-containing media (final concentration 1 µM) for 30 min. At the end of the incubation time, the cells were washed three times with PBS and then lysed in RIPA buffer. Afterwards, the concentrations were measured by Bradford before Immunoblotting. Puromycin was detected with a conjugated antibody afterwards (1:1.000, anti-Puromycin, clone 12D10, AlexaFluor 647, Merck, Darmstadt).

3.2 Microbiology techniques

3.2.1 Preparation of competent bacteria

To prepare competent bacteria, One Shot™ Stbl3™ bacteria were streaked on agar-plates for colony purification and grown over night at 37 °C. The day after, an overnight culture was inoculated with one single colony in LB media and grown at 37 °C for 24 hours. The next day, 250 ml of LB media was inoculated with 4 ml of the overnight culture and the bacteria grown at 37 °C to early log phase (OD_{600} = 0.3 - 0.6, approximately 1 - 2 h) before placed on ice immediately. The solution was then centrifuged (10 min, 1000 × g, 4 °C), the supernatant discarded and the pellet resuspended in 25 ml cold TSB and incubated on ice for 10 minutes. Afterwards, aliquots of 100 µl were made and snap-frozen in liquid nitrogen before storage at -80 °C.

3.2.2 Bacterial Transformation and plasmid preparation

To transform bacteria with the plasmid of interest, competent One Shot™ Stbl3™ bacteria were used. First, 200 – 500 ng of the DNA plasmid were mixed with 20 µl KCM buffer (5×) and filled up to 100 µl with H_2O. After thawing the competent bacteria on ice, 100 µl of competent cells were gently mixed with the 100 µl of DNA solution and incubated on ice for 20 minutes. Afterwards, the solution was incubated at room temperature for 10 minutes, before adding 1 ml LB-media to the bacteria and let them grow for one hour at 37 °C, to permit expression of the resistance gene. After one hour, the bacteria were shortly centrifuged (300 × g, 1 min), the supernatant mostly removed and the bacteria plated on LB agar plates, containing respective antibiotics for selection (Carbenicillin: 100 µg/ml, Kanamycin 50 µg/ml). The plates were then incubated at 37 °C over night, before further processing. For the overnight culture, 1 colony was picked with a sterile pipette tip and inoculated in 5 ml LB containing respective antibiotics. Afterwards, either a glycerol culture was made for long-term storage or a Mini- or Maxi-Preparation of the plasmid was done afterwards.

For the glycerol culture, bacterial suspension was mixed with 50 % Glycerine (1:1) and immediately frozen at -80 °C.
Mini- and Maxi-Preparation were done with the NucleoSpin Kit from Macherey Nagel, according to manufacturing instructions.
All plasmids were then sequenced for correct insertion before further processing.

3.3 Cell biology techniques

3.3.1 Culturing and cryopreservation of PDAC cell lines

All used cell lines are adherent cell lines and were cultured in 37 °C, 5 % CO_2 and 100 % humidity in a CO_2- incubator under sterile conditions in cell culture flasks. Murine pancreatic cancer cell lines (see 2.7.2.1) were cultured in complete Dulbecco's Modified Eagle's Medium (DMEM) with 10 % (v/v) Fetal bovine serum (FBS) and 1 % (v/v) Penicillin/Streptomycin (Pen/Strep), whereas the conventional PDAC human cell lines (see 2.7.2.2) were cultivated in Roswell Park Memorial Institute media (RPMI), with the same additives. In contrast, patient-derived cell lines (PDCLs, see 2.7.2.3) were cultured in RPMI with 20 % (v/v) FBS and 1 % (v/v) Pen/Strep.
Passaging of cells was carried out when the cells were 80 - 90 % confluent, by washing once with PBS and detaching the cells with Trypsin/EDTA solution afterwards. Trypsinisation was stopped by addition of new media and the cell suspension was seeded out into new cell culture flasks or dishes, according to experimental conditions. All cells were counted with a Neubauer chamber beforehand.
For long-term storage and cryopreservation, the cell suspensions were centrifuged at 1.000 rpm for 5 min, the supernatant discarded and the pellet was resuspended in the freezing media (respective culture media without antibiotics, 20 % (v/v) FBS and 10 % (v/v) DMSO). For short- or long-term storage, they were stored at -80 °C or liquid nitrogen in Cryotubes, respectively.
Conventional human cell lines were authenticated before usage by Multiplexion (Multiplexion GmbH, Heidelberg, Germany) or Microsynth (Microsynth AG, Balgach, Switzerland).
The primary human PDAC organoid and cellular models were established and analysed in accordance with the declaration of Helsinki and approved by the local ethical committee TUM, Klinikum rechts der Isar (Project 207/15, 946/07, 330/19 and 80/17S). The written informed consent from the patients for research use was obtained prior to the investigation.

3.3.2 Cell viability assays for drug screen: MTT and CellTiter-Glo® to determine GI_{50} values or the synergy score

To determine cell viability after addition of several drugs in the drug screen, either the MTT (measuring reduction equivalents) or the CellTiter-Glo® assay (measures ATP, Promega) was performed.
The MTT assay is based on a colorimetric reaction, where the yellow, water soluble 3-(4,5-Dimethylthiazol-2-yl)-2,5-diphenyltetrazolium bromide (MTT) reagent gets reduced to a purple, water insoluble Formazan by a mitochondrial reductase. For this assay, 2.000 cells were seeded in 100 µl in a 96 well plate in triplicates. After 24 h, the cells were treated with the respective inhibitors in a 6- or 7- fold dilution (from 0 - 50 µM) and incubated for 72 h under normal cell culture conditions. After incubation with 10 µl MTT reagent for 4 h at 37 °C, the whole media was removed and the water insoluble Formazan was dissolved in 200 µl DMSO and EtOH (1:1) for 10 minutes on the shaker. After that, the optical density at 595 nm was measured by a microplate reader (Thermo Multiscan FC).
For the CellTiter-Glo assay, the same experimental design was accomplished, but instead of an addition of MTT, 25 µl of the CellTiter-Glo reagent were added to each well and instructions carried out according to the manufacturer's specifications. Afterwards, the quantification of ATP was recorded via luminescence by the FluoStar Optima microplate reader.
All measurements of MTT or CellTiter-Glo were accomplished in three technical and three independent biological replicates for each drug. For analysis, the mean value was formed from the technical replicates, normalised to the respective controls and the viability curves are depicted as the logarithmic relative growth values. The area under the curve (AUC) or the 20 % or 50 % growth inhibitory concentration (GI_{50} or GI_{20}) values were determined by GraphPad Prism 9 using a non-linear regression model (log inhibitor vs. response (three parameters)). For determining the synergy scores of multiple drugs, the web-application Synergy Finder (Version 2.0, https://synergyfinder.fimm.fi) was used for interactive analysis.

3.3.3 Clonogenic assay

To determine the colony formation, proliferation and survival possibility from different drugs, a clonogenic assay was implemented. For this, 1.000 cells / 400 µl were seeded into 24-well cell culture plates and treated with respective drugs. After long-term

treatment, but at least after 7 days of cultivation, the supernatant was removed, the cells washed once with PBS and then fixed and stained with 200 µl 0.2 % (w/v) crystal violet solution in 2 % (v/v) EtOH for 15 minutes. After washing three times with distilled water, the plates were air-dried overnight and scanned afterwards with a flatbed scanner. To quantify the colonies, 600 µl of 1 % (w/v) SDS was added to solubilise the stain and absorbance was measured at 595 nm with a CLARIOstar multiplate reader (BMG Labtech GmbH, Ortenberg, Germany). The values of a minimum of three independent biological replicates were calculated and normalised to the respective controls.

3.3.4 Flow cytometry assays: PI cell cycle & Annexin V/PI apoptosis measurement

For measuring the DNA content in the cell, Propidium Iodide (PI) was used. PI insertion is proportional to DNA content and reflects different stages of the cell cycle. Cells in G2/M phase will have double the amount of DNA than cells in G1 stage, whereas cells in S phase will have more PI insertion than G1 phase, because they already doubled their DNA amount. For the measurement, 1.8 x 10^6 cells were seeded in 10 cm plates one day before and then treated with the respective inhibitor as indicated. To stop cell cycle and fix the cells, the media was removed, the cells washed once with ice-cold PBS, trypsinised and centrifugated together with PBS × for 5 min, 4 °C and 1000 rpm. The pellet was then resuspended in 1 ml ice-cold 70 % Ethanol (-20 °C) and the cells fixated overnight at 4 °C. The day after, 1 ml PBS was added to the fixated cells (1:1), centrifuged as indicated before, the supernatant discarded and the pellet resuspended in 1 ml fresh PBS + 2 % FCS (% v/v). To prevent RNA contamination, 50 µg/ml RNaseA was added and incubated for 60 min at 37 °C in the dark. Shortly before FACS measurement, 25 µg/ml PI was added for 5 min. The samples were measured with the Gallios™ Flow Cytometer and the data analysed with FlowJo 10.7.1 afterwards.
For the determination of apoptosis, a Annexin V/PI measurement was done with the FITC Annexin V Apoptosis Detection Kit I (RRID: AB_2869082, # 556547, BD Biosciences, San Diego, USA). Cells were seeded in 10 cm plates one day prior to treatment, to be confluent the next day. After treatment with 20 µM LB-100, cells were incubated for 6 hours before the cells were washed with 4 ml PBS and trypsinised with 0.05 % (v/v) EDTA for 5 minutes. The liquids of all washing steps were collected together with the detached cells and afterwards centrifuged for 5 minutes (1000 × g). The supernatant was removed and the pellet resuspended in 500 µl 1× binding buffer with 5 µl FITC-Annexin and 2 µl PI according to manufacturer's instruction. Afterwards, the samples were

measured in a CytoFLEX S flow cytometer (Beckman Coulter, California, USA) and analysed using the FlowJo™ Software (RRID: SCR_008520, FlowJo, LLC, Ashland, Oregon, USA).

3.3.5 Lentiviral production and transduction

For lentiviral transduction of cells with the plasmid of interest, Lentivirus was first produced in HEK293FT cells. For this, 3 x 10^6 HEK293FT cells were seeded in 10 cm plates in DMEM media containing 10 % FSC and 1 % Pen/Strep. The next day, two tubes were prepared for the transfection mix: one tube containing 1.5 ml Opti-MEM™ with 40 µl Lipofectamine 3000 and for the other, 1.5 ml Opti-MEM™ was mixed with 35 µl P3000 Enhancer, 6.3 µg psPAX2 and 4.1 µg pMD2 (packaging plasmids) and 8.2 µg of the plasmid of interest. The tubes were mixed afterwards (1:1) and incubated at room temperature for 15 - 30 minutes. The solution was then added dropwise to the plate, evenly distributed and the cells were incubated at 37 °C 5 % CO_2 overnight. On day three, the media was changed with 4 ml fresh complete media, incubated again overnight and the first supernatant, containing the virus, was collected on day four. The same procedure was repeated and the second supernatant collected on day five, filtered together with the first supernatant through a 0.45 µM filter, aliquoted and stored at -80 °C.
To transduce the cells of interest, 200.000 cells were seeded in a 6 well plate in 2 ml media, including two wells for uninfected control (+/- antibiotic). 24 hours after seeding, the cells should have reached 50 % confluency. The media was removed and replaced with 1 ml of media containing 8 µg/ml Polybrene and 200 - 500 µl of virus, depending on the titer. The cells were spininfected (1000 × g, 30 min, 33 °C) and then further incubated at 37 °C. The next day, the virus containing media was removed and fresh media added. On day four, the antibiotic selection process was started by adding the lowest possible concentration for the specific cell line (determined before by titration). After two or three rounds of selection, the cells in the control well should all be dead and the selection process finished.

3.3.6 Seahorse assay

To measure the oxygen consumption rate (OCR) and extracellular acidification rate (ECAR) to determine mitochondrial respiration and glycolysis, respectively, a seahorse assay was performed. For this, 10.000 cells were seeded in 80 µl Seahorse XF DMEM medium in Seahorse Cell Culture Microplates (96-well) one day prior to treatment. An

additional black plate was prepared, which was treated the same way, to measure DNA content in the end as a reference probe. The Seahorse Extracellular Flux XFe96 cartridge was hydrated overnight with 200 µl H_2O, which was exchanged the next day to 200 µl Calibration solution before further processing. LB-100 treatment was carried out the next day for two, four and six hours with 20 µM in 20 µl of media, before exchanging the media to glucose Seahorse medium (180 µl per well, 5 g/L Glucose in DMEM Seahorse media, pH 7.4) for measuring OCR. For measuring ECAR, media was changed without the addition of glucose. The cells were then again incubated at 37 °C for 1 hour, without the addition of CO_2. Afterwards, the injection solutions were prepared in glucose free Seahorse media, irrespectively of OCR and ECAR measurements, as shown in table 19 and 20 and loaded into the cartridge according to port orientation illustrated in table 21.

Table 20 | Injection solutions for OCR measurement

Number / Port	Inhibitor	10 x [Port]	[Final well]	Volume per Port / Well
1 Port A	Oligomycin	25 µM	2.5 µM	20 µl
2 Port B	FCCP Pyruvate	10 µM 50 mM	1 µM 5 mM	22 µl
3 Port C	Antimycin A Rotenone	25 µM 25 µM	2.5 µM 2.5 µM	25 µl
4 Port D	Only Media		-	27 µl

Table 21 | Injection solutions for ECAR measurements

Number / Port	Inhibitor	10 x [Port]	[Final well]	Volume in Port / Well
1 Port A	Glucose	100 mM	10 mM	20 µl
2 Port B	Oligomycin	25 µM	2.5 µM	22 µl
3 Port C	2-Deoxyglucose	1 M	0.1 M	25 µl
4 Port D	Only Media		-	27 µl

Table 22 | Port orientation of the Seahorse XF96 flux analyser

Port orientation	
A	**B**
C	**D**

OCR and ECAR were measured using the XF96 Extracellular Flux Analyzer (Seahorse Bioscience) in cooperation with Dr. Michael Dudek in the lab of Prof. Dr. Percy A. Knolle (Insititute of Molecular Immunology, Technical University Munich, Klinikum Rechts der Isar). Calibration was performed for 20 minutes before starting four rounds of measurement cycles, each consisting of three mixing, waiting and measuring cycles before injecting the next solution. This results in three measurement points for each condition, which in the end were normalised to DNA content. The DNA content was measured by the addition of 1 µg/ml Hoechst 33342 to the black well plate, which was treated the same way and analysed afterwards with the FLUOstar OPTIMA fluorescent reader.

3.3.7 Mycoplasma test

To test routinely for possible mycoplasma contamination, cells were kept in complete cell culture media without the addition of antibiotics for a minimum of one week until they reached almost 100 % confluency. Afterwards, 2 ml of the supernatant was centrifuged for 2 min at 250 × g to remove the cellular debris. After transferring the supernatant into a new Eppendorf tube and an additional centrifugation step (10 min, 20.000 × g), the pellet was resuspended in 50 µl TE Buffer to solubilise the DNA and heat inactivated at 95 °C for 3 min. A polymerase chain reaction (PCR, 95 °C 15 min, [40 x 94 °C 1 min, 60 °C 1 min, 74 °C 1 min], 72 °C 10 min, 4 °C ∞), including positive and negative controls, was performed with the primers in table 2.5.1.

3.4 Imaging techniques

3.4.1 Immunocytochemistry

To visualise the proteins of interest and the distribution within the cell, indirect immunofluorescence staining was carried out. For this, 11.000 cells / 100 µl were seeded into a 18-well µ-slide (Ibidi). The day after, treatment was done as indicated before fixation of the cells. The cells were fixed with 4 % PFA for 10 min before washing 3 times with PBS.

Afterwards, the cells were permeabilised with 0.1 % PBS-Triton X-100 for 10 min and then blocked for one hour with Blocking buffer (1 % BSA /10 % normal goat-serum / 0.3 M Glycine in 0.1 % PBS-Tween20). When antibodies from goat origin were used, the cells were blocked in the same buffer without the addition of goat-serum. The cells were then incubated overnight at 4 °C with the primary antibody at 5 µg/ml concentration in Blocking buffer. The next day, the primary antibody was removed, the cells were washed three times with PBS and afterwards incubated with the secondary antibody for two hours at room temperature in the dark according to host species (1:1000 dilution in Blocking buffer). To visualise the nucleus, the cells were incubated with Hoechst33342 for 5 minutes (1 ug/ml in PBS) afterwards. In the end, the cells were kept at 4 °C in PBS in the dark until microscopy with the Leica SP8 Confocal microscope.

3.4.2 Autophagy measurement by LysoTracker®

To measure autophagy, LysoTracker® staining of acidic lysosomes was accomplished. 10.000 cells were seeded in an 18-well µ-slide (Cat# 81816, Ibidi, Munich, Germany) one day prior to the six-hour treatment with LB-100 (20 µM). After treatment, the media was changed to media containing 50 nM LysoTracker® reagent and incubated again for one hour at 37 °C, 5 % CO_2.Afterwards, 1 µg/µl Hoechst 33342 was added for 10 minutes, before imaging the cells via Live-cell imaging. The Live-cell imaging was done with a Leica SP8 Confocal microscope under a constant temperature of 37 °C. The median fluorescent intensity was calculated using the ImageJ software[155] (RRID:SCR_003070).

3.5 Organoid culture

3.5.1 Isolation and culturing of patient derived organoids

Generation, isolation and cultivation of human patient derived organoids from patient samples (biopsies or tissue) were recently described[156]. Organoid isolation and culture were done in cooperation with Felix Orben and Aylin Aydemir (AG Schneider, Technical University of Munich) or Constanza Tapia Contreras (AG Schneider, Georg-August-Universität Göttingen).

3.5.2 Drug Screen of PDAC-Organoids

To determine the drug sensitivity of patient derived organoids, 500 single cells per well were seeded in a 384-well plate in 20 µl PDO-drug screen media one day prior to treatment and centrifuged (10 sec, 500 rpm). The next day, LB-100 or Phendione was applied in a 9-fold dilution (0 - 200 µM), diluted in 4 µl PDO media / well and centrifuged (10 sec, 500 rpm). After 72 hours of incubation at 37 °C and 5 % CO_2, 5 µl CellTiter-Glo® Luminescent Cell Viability Reagent was added and the fluorescent signal measured with a FLUOstar OPTIMA microplate reader. Drug screening of patient derived PDAC-organoids was done in cooperation with Felix Orben (AG Schneider, Technical University of Munich) and described recently[156].

The primary human PDAC organoid and cellular models were established and analysed in accordance with the declaration of Helsinki and approved by the local ethical committee TUM, Klinikum rechts der Isar (Project 207/15, 946/07, 330/19 and 80/17S) or the University Medical Center Göttingen (UMG) (vote 11/5/17). The written informed consent from the patients for research use was obtained prior to the investigation.

3.6 RNA Techniques

3.6.1 RNA Isolation of cultured cells

For RNA sequencing, 1.8 x 10^6 cells were seeded in 10 cm plates and incubated overnight at 37 °C, 5 % CO_2. After respective treatment with LB-100 for 2, 6 or 24 hours, the cells were placed on ice, washed one time with ice cold PBS and then harvested in 200 µl chilled Homogenisation solution (20 µl of 1-Thioglyverol / ml of Homogenization solution) and further processed according to the manufacturer's instructions (Maxwell® 16 LEV simplyRNA Cells Kit, Promega). The RNA was eluted in the end in 30 µl H_20 to have a high concentrated eluate, before measuring the concentration with the NanoDrop.

3.6.2 Deep RNA Sequencing and bioinformatic analysis

For analysation of changes in gene expression, splicing and transcription, deep RNA Sequencing was done. For this, 300.000 cells were seeded in a 6-well plate one day prior to drug treatment with 20 µM LB-100 for either 2 or 6 hours. After that, the media was carefully removed and the cells washed one time with PBS and immediate

homogenised in 1-Thioglycerol Homogenisation solution from the Maxwell® RSC simplyRNA Tissue Kit (#AS1280, Promega, Walldorf, Germany). The further purification steps were done according to the manufacturer's instruction.

RNA Sequencing and quality control were done in collaboration with Dr. Rupert Öllinger and the lab of Prof. Dr. Roland Rad (TranslaTUM, Munich) as previously described [37,157]. To first purify the mRNA from total extracted RNA, poly-T oligo-attached magnetic beads were used. The first strand cDNA synthesis was then carried out using random hexamer primers before synthesising the second strand cDNA. As a second step, the library was prepared after end repair and A-tailing, followed by adapter ligation and size selection. To validate the insert size and quality of the library after amplification and purification, the Agilent 2100 bioanalyzer was used for the fragment analysis before quantified by Q-PCR. In the end, libraries were then sequenced to a depth of 15 Gbp on Illumina NovaSeq 6000 S4 flow cell with PE150 by Novogene (Novogene International Holding, Netherlands). All RNA samples were collected as technical triplicates.

Reanalysis of the sequencing data was performed with the help of Prof. Dr. Paul Boutz and Xueyang He (University of Rochester, Willmot Cancer Institute, NY, USA). Summed up, raw RNA-seq reads were mapped to the mouse mm10 genome build using the STAR aligner version 2.5.3a (RRID:SCR_004463)[158] with the parameters: STAR --runMode alignReads --runThreadN 4 --genomeDir mm10 --twopassMode Basic --outSAMtype BAM SortedByCoordinate --outFilterMultimapNmax 20 --outFilterMismatchNmax 999 --outFilterMismatchNoverLmax 0.033 --alignIntronMin 70 --alignIntronMax 500000 --alignMatesGapMax 500000 --alignSJoverhangMin 8 --alignSJDBoverhangMin 1 --outSAMstrandField intronMotif --outFilterType BySJout. To identify detained introns, reads mapped with STAR aligner as described above were filtered for contiguous genome alignment. Mapped reads were then filtered using BedTools 2.25.0 (RRID:SCR_006646)[159] remove reads overlapping expressed repeats from the UCSC genome browser (RRID:SCR_005780)[160] RNA repeats and Ensembl Mm10 annotations (RRID:SCR_002344) [161,162] and coding exons annotated in the Gencode Mm10 (RRID:SCR_014966) annotations. Reads attributable to alternative polyadenylation sites were removed based on known Gencode polyadenylation sites. DESeq (RRID:SCR_000154)[163] was used to normalise intronic read counts and to account for coverage depth and dispersion across replicates. Assuming all introns of a gene are represented equally abundant in the genome, the intronic reads were distributed and allocated proportional to its weight. For additional details see [164]. Afterwards, DESeq was used for differential analysis of enriched read coverage in intronic regions (read counts) and compared to expected counts by using the threshold of the p-value adjusted FDR of 0.01, together with and FC of 2. Custom Python (RRID:SCR_008394) scripts were

established and used to derive a transcriptome annotation, which is based on the Mm10 start and end lines of a gene. The same was done to determine the genomic locations of detained introns as described above, similar with the genomic locations of all splice junctions.

Detained introns: To quantify detained intron splicing differences between the conditions, 3 biological replicates were used for each treatment at each time point. The custom annotation described above was used as input to generate an 'exon part' gtf-file that is compatible with DEXSeq (RRID:SCR_012823) [165]. DEX-Seq analysis was then further used to determine the differential expression of the alternative splicing events and detained introns, always calculated with a padj <0.05 to mark the cutoff for significant changes.

Alternative splicing: the published algorithm rMATs (RRID:SCR_001583)[166] was used to quantify skipped/cassette exons, alternative 3' and 5' splice sites, and mutually-exclusive exons. A significance padj of < 0.05 was used to determine significant splicing events.

Gene expression: The feature "counts command" from the subread software (RRID:SCR_009803) tool was used to produce the gene count matrix with the original bam files and input junction consensus gtf [167]. Differential gene expression was analysed using DESeq2 (RRID:SCR_009803) between each treatment time and control samples. This derives a log2fold change and a corresponding adjusted p value for each gene in each treatment comparison. padj < 0.05 is used as cutoff for significant events.

All deep RNA Seq-Data from mesenchymal (PPT-8248) and epithelial (PPT-9591) cell line after treatment with LB-100 for 2 and 6 hours, were deposited in the European Nucleotide Archive (ENA: PRJEB59091) and are freely accessible.

3.7 CRISPR resistance screen

To conduct a CRISPR/Cas9 dropout screen following drug treatment for 14 days, a recently published protocol was carried out in murine and human cell lines [168]. The human CRISPR dropout screen with the human Brunello CRISPR knockout pooled library (library was a gift from David Root and John Doench (Addgene #73178) was done in cooperation with Matthias Wirth and Hazal Köse (Campus Benjamin Franklin, Charite-Universitätsmedizin Berlin) according to their protocol (see 3.7.2). To also establish the dropout screen in the murine cell lines, the protocol from Katia Sleimann (AG Dieter Saur, Technical University of Munich) and Sebastian Widholz (AG Roland Rad, Technical University of Munich) was adapted (see 3.7.1-3.7.4).

3.7.1 Resistance screen in murine PDAC cell lines

3.7.1.1 Library amplification

To amplify the mouse CRISPR knockout pooled library (BRIE, Mouse Brie CRISPR knockout pooled library was a gift from David Root and John Doench (Addgene #73633), 2 µl of 50 - 100 ng / µl library was added to 25 µl Endura Electrocompetent cells (#71003-032, VWR International, USA) in a pre-chilled electroporation cuvette (0.1 cm gap) and pulsed at 1.8 kV (EC1). Endura Rescue Media was added directly afterwards to resuspend the cells, before additional SOC media was added. Bacteria were recovered by rotating the bacteria at 250 rpm for 1 hour at 37 °C, before pooling all cells and plating them on pre-warmed LB-agar plates (+Ampicillin 100 ug/ml) overnight at 30 °C. On the next day, transformed bacteria were harvested by pipetting 10 ml of LB media on each plate and the colonies gently scraped off with a cell spreader, before spinning down the bacteria and extracting the plasmid DNA with the Plasmid Maxi Kit from Machery-Nagel.

3.7.1.2 Lentiviral production of pooled sgRNA library

The production of the lentivirus, containing all sgRNAs, was performed in HEK293FT cells. For this, 9.5 million cells were plated in 15 cm plates in 20 ml media (DMEM + 10 % FCS, 1 % P/S) one day prior to transfection. The next day, the media was exchanged to fresh media, before the transfection mix was added dropwise. The transfection mix contained 1900 µl Opti-MEM media with 15.6 µg psPAX and 10.2 µg pMD2 vectors and 170 µl TransIT-LT per plate, was incubated together for 30 minutes at room temperature, before it was added to the cells. The next day, the media was exchanged

with 11 ml fresh media. On day 4, the viral supernatant was collected, filtered with a 0.45 µm filter, aliquoted and stored at - 80 °C.

3.7.1.3 CRISPR library transfection and drug selection

For the CRISPR knockout screen, Cas9-expressing murine pancreatic cancer cell lines were used (PPT-9091, Sebastian Widholz, AG Rad, Technical University of Munich). These cells were stably transduced with the lentiCas9-Blast plasmid (lentiCas9-Blast was a gift from Feng Zhang (Addgene plasmid # 52962 ; http://n2t.net/addgene:52962 ; RRID:Addgene_52962) and selected with Blasticidin, as published recently [169]. Cas9 expression was confirmed by western blot and functionality tested with sgRNA transfection. For the CRISPR screen, 160 million cells per replicate (80.000 sgRNA x 500 coverage x 0.3 MOI) were seeded in 6-well plates at a density of 3 million cells / well. The respective amount of virus was added to each well (one well for control, no virus added) together with 8 µg/ml Polybrene transfection reagent. The cells were spin-infected at 1000 × g for 2 h at 33 °C before returning them into the incubator. The amount of virus needed for MOI = 0.3 was determined before by titration of the respective cell line. 24 hours after the end of the spin-infection, the selection with puromycin (5 µg/ml) was started. For this, the cells were washed with PBS and trypsinised with 100 µl to dissociate the cells. Two wells (~ 6 million cells) were seeded in one 15 cm plate in 20 ml media, containing 5 µg/ml Puromycin. After all cells died in the control (without virus, after around 4 to 5 days), the cells were split for the first time and recovered in normal growth media for 3 additional days. For the drug selection, the cells were then trypsinised, briefly spinned down and pooled together in one falcon. The cells were counted in a 1:10 dilution and ~35 million cells per replicate and treatment condition (3.5 mio per plate) seeded. The drugs were added at the respective GI_{30} concentration, 10 µM LB-100 and 100 nM Phendione. This was repeated every 3 to 4 days for 14 days of drug selection. After 14 days, the gDNA was extracted using the QIAGEN blood and cell culture DNA maxi kit.

3.7.1.4 Library prep of CRISPR Screen gDNA with Kapa HIFI

To prep the library of the gDNA extraction, a PCR with 500× coverage was done first. For this, 228 µg gDNA was mixed with 76 µl forward primer (10 µM, P50X, see 2.5.2for sequence), 76µl reverse primer (10 µM, P70X, see 2.5.2 for sequence), 950 µl Kapa HIFI Short Master Mix 2× (Roche, Switzerland, #08202923001) and water in 1.9 ml

reaction volume. This volume was distributed in 38 50 µl PCR tubes and the following cycle condition were performed:

Table 23 | CRISPR gDNA PCR cycler conditions

95 °C	3‘	
98 °C	20‘‘	X 28
62 °C	30‘‘	
72 °C	45‘‘	
72 °C	5‘	
10 °C	hold	

Afterwards, all 38 reactions were pooled in one tube and a 281bp band was confirmed on an agarose gel. 200 µl of pooled PCR product were cleaned with the Gel and PCR clean up kit from Macherey Nagel, but 5× more binding buffer was added and the column loaded multiple times. The cleaned product was eluted in 25 µl H2O in low binding tubes. Sequencing was performed in cooperation with Rupert Öllinger (AG Rad, Technical University of Munich) according to their previously published protocol [170].

3.7.2 Resistance screen in the human MIA PaCa-2 cell line

Following the manufacturer’s protocol, 400 ng of the library plasmid DNA was amplified using ElectroMAX™ D10HB cells (ThermoFisher, #18290015). Human Brunello CRISPR knockout pooled library was a gift from David Root and John Doench (Addgene #73178). The library was added and transferred into a chilled electroporation cuvette and pulsed (BioRad, Feldkirchen, Germany) at 1.8 kV, (Ec1). SOC medium was directly added after the pulse and the cells were shaken in an incubator for 1 h at 30 °C. Cells were then spread on prewarmed LB-agar bioassay plates (Thermo Fisher, #10489282) supplemented with Ampicillin 100 µg/mL at 30 °C for 16-18 hours. Transformants were pooled and plasmid DNA was extracted with the HiSpeed Plasmid Maxi Kit from Qiagen. Lentivirus production was conducted by seeding HEK293T cells (4-5 million cells in 10 cm dishes) in DMEM (Thermo Fisher Gibco, #41965062) supplemented with 10 % Fetal Bovine Serum (Thermo Fisher Gibco, #A5256701). 1 ml of Opti-MEM (Thermo Fisher Gibco, #31985-062) + 20 µL of Lipofectamine2000 transfection reagent (Thermo Fisher, #11668019) 10 µg of each plasmid (pPAX2; pMD2G; lentiCas9-blast; sgRNA library). lentiCas9-Blast was a gift from Feng Zhang (Addgene plasmid # 52962). The mixture was incubated 20 min at room temperature and then added to the HEK293T cells and

mixed gently. The medium was changed 12 hours post-transfection and viral supernatant was collected 36 hours after transfection and filtered using a 0.45 µm syringe filter. A total of 3 million MiaPaCa-2 cells were seeded in 6-well plates, one day prior to transduction. 3 mL of the spCas9 viral supernatant was added to the cells with polybrene 1 µg/mL (Merck, #TR-1003-G) and cells were spin-transduced 1 h at 2000 rpm at 32 °C. 24 hours later, cells were split and selected with Blasticidin S HCl 10 µg/mL (Thermo Fisher Gibco, #A1113903). Cas9 expression was confirmed by western blot and functionality was assessed by sgRNA transfection. MiaPaCa-2-Cas9 cells were seeded in 3 ml in 6-well plate at a density of 1 million cells / ml. To determine the multiplicity of infection (MOI) of the virus, various dilutions were conducted in each well: 1:15, 1:30, 1:60, 1:120 and 1:240. 1 µg/mL of polybrene was added (Merck, #TR-1003-G) and cells were centrifuged at 2000 rpm at 32 °C for 1 hour. One day after the spin-transduction, the cells were split in 2 groups and one group was selected with puromycin 1 µg/µL (Thermo Fisher, #A1113803). Calculation of the MOI: (Transfected cells treated with puromycin) / (Transfected cells without puromycin) x 100) - (untransfected cells treated with puromycin) / (untransfected cells without puromycin) x 100). Next, 3×10^8 MiaPaCa-2-Cas9 cells were seeded and transduced with the Brunello library which contains 19,112 targeted genes, 76,448 sgRNAs and 1000 controls aiming an MOI of 0.3. The transduction was conducted in the same conditions as the titer determination. The transduced cells were selected with 1 µg/mL of puromycin for 7 days. Pellets were harvested and frozen for genomic DNA analysis on day 0. Cells were split into two groups, one treated with vehicle and the other with LB100 (5 µM) for 14 days. At the end of the screen, cells were harvested for genomic DNA isolation (Macherey-Nagel, Tissue Kit, #740952.10). sgRNAs were amplified by PCR according to the manufacturer's protocol, PCR products were purified using AMPpure beads and samples were sent to Novogene for next-generation sequencing.

3.7.3 Bioinformatical analysis of both screens

The sequencing data was analysed using the MAGeCK pipeline from the Galaxy platform [171] in cooperation with Riccardo Trozzo (AG Rad, TranslaTUM) and Matthias Wirth (Charité Berlin). In brief, the CRISPR screen reads were assessed for quality using sequencing tools as FASTQC (RRID:SCR_014583), MultiQC [172] and were trimmed using the Trimmomatic tool [173] to maintain the base pairs containing the guide RNA. The detection of enriched and depleted guides was performed using MAGeCK mle algorithm [174] (CRISPR screen analysis, counting and testing). Subsequently, resulting significant

(FDR < 0.05) beta scores were used for pathway analysis. Here, Hallmark and Gene Ontology (Biological Process) pathways of the molecular signature database (MSigDb) were investigated using gene set enrichment analysis of GeneTrail [175].

3.8 Public available datasets

3.8.1 Overlap of LB-100-treated and INTS8-depleted gene expression pattern

To find overlapping gene expression patterns between previously published INTS8-depleted HEK293FTcells [176] and murine LB-100 treated epithelial and mesenchymal cell lines, all GeneID data was converted from human to mus musculus using the Orthology search tool (g:Orth) accessed from g:Profiler (https://biit.cs.ut.ee/gprofiler/orth). Afterwards, all significantly regulated genes (p< 0.05) in both datasets were compared independently of their log2FC. Concordant genes can be found in both datasets up- or down-regulated, discordant ones in only one of them.

3.8.2 Human and murine mRNA expression datasets, GSEA, Priority scores, correlation of GI_{50} with gene expression

Priority scores for identifying cancer dependencies and finding targets for precision cancer therapy were accessed from the Project Score (https://score.depmap.sanger.ac.uk) website[177] for pancreatic carcinoma (default settings). Human expression datasets and pharmacologic dependencies (Express public 22Q4) of CRISPR/Cas9 dropout screens and gene effects (Chronos[178]) were evaluated via the DepMap portal (https://depmap.org). Gene mRNA expression in cancer (n=179 PDAC) and normal tissues (n=171) were accessed from the GEPIA portal (http://gepia.cancer-pku.cn/, log2FC cutoff= 1, p-value cutoff = 0.01, match normal TCGA and GTEx data[179]), protein expression from PPP2CA (UniProt: P67775) was acquired from ProteomicsDB Expression dataset (MS1, iBAQ, https://www.proteomicsdb.org/[180]). RNA-expression dataset from 38 murine *KRAS*-^{G12D} driven murine cell lines were recently published [37]. GI50 values, calculated as described above, were correlated with overall gene expression (log2FC) in each cell line using Pearson correlation as recently described [181]. The Pearson correlation coefficient was used afterwards for a pre-ranked GSEA analysis (GSEA version 4.0.3) with default settings. mRNA expression datasets from human Pancreatic adenocarcinoma patients (QCMG, TCGA PAAD and CPTAC) were accessed from the cBioPortal (https://www.cbioportal.org/). Gene enrichments were performed using GSEA and

MSigDB (GSEA version 4.0.3 [182,183]), GeneTrail 3.2 (www.genetrail.bioinf.uni-sb.de) [175] or ShinyGo (http://bioinformatics.sdstate.edu/go/ [184]). Heatmaps, Venn analysis and graphical representation or illustrations were made with GraphPad PRISM 9.4.0, R-studio (V 1.4.1717) or jVENN (http://jvenn.toulouse.inra.fr/app/example.html), respectively. mRNA expression datasets of LB100-treated mesenchymal (PPT-8248) and epithelial (PPT-9591) cells can be freely accessed via the European Nucleotide Archive (ENA): PRJEB59091. Parts of figures were drawn by Servier Medical Art or using BioRender.com (https://biorender.com/). Servier Medical Art by Servier is licensed under a Creative Commons Attribution 3.0 Unported License (https://creativecommons.org/licenses/by/3.0/). For visualization of protein structures, UCSF Chimera 1.13.1 was used [185]. Grammarly was used as writing assistance to improve readability.

3.9 Statistics

Statistical tests, number of replicates and error bars are always explained in their respective figure legend. P-values marked with an asterisk are always determined as: * = $p < 0.05$, ** = $p < 0.01$, *** = $p < 0.001$.

4 Results

Parts of the results of this dissertation have been submitted for publication. Contributions and results, who were done in cooperation with Co-authors, are indicated in the respective figure legends or methods section.

4.1 The Protein phosphatase 2A is a highly relevant target in aggressive PDAC

Targeted and context-specific treatment will be the foundation for precision medicine in the future. The Project Score website was accessed, to find new and relevant targets for this kind of medicine for pancreatic adenocarcinoma (https://score.depmap.sanger.ac.uk/). This tool was established by comparing CRISPR/Cas9 Knockout fitness scores with genomic markers and patient genomic data, to find out cancer dependencies and new therapeutic targets [186]. By looking into the dataset for pancreatic adenocarcinoma, a lot of approved targets can be found, that are also already under clinical development. This includes for example the translational regulators *EIF4G1*, *CDK4* or *AURKA* [187–190]. Surprisingly and interestingly, the catalytic subunit of the Protein phosphatase 2A *(PPP2CA)* was ranked as one of the highest prioritized targets in PDAC (Fig. 6a). To further invest into the relevance of the phosphatase in different organs, the proteome expression tool from Proteomics. dB was consulted [180]. Indeed, the catalytical subunit of the phosphatase is a highly expressed protein, especially in pancreatic tissue (Fig. 6b). By further also comparing the normal pancreatic tissue to tumours, even higher mRNA expression could be detected in cancer tissue, manifesting a relevance of this phosphatase for specific PDAC treatment (Fig. 6c). Cox regression analysis provides a connection between mRNA overexpression and survival probability, thereby implementing a hazard ratio as variable when compared to Kaplan-Meier curve analysis [191]. The higher the score, the higher the increase in the hazard ratio and the less is the survival probability, correlating with the specific gene expression. Literally, PPP2CA expression is linked to shorter survival and worse prognosis in pancreatic cancer in the TCGA analysis (Fig. 6d). To strengthen this finding, clinical data and mRNA expressing sets from Bailey et al. [39] were implemented into the analysis as well. The data was curated as previously described [192], separated into quartiles and PDAC patients with a high PPP2CA expression (>75th percentile) were compared to low expressing ones (<75th percentile) using a log-rank test. Also in this analysis, PDAC patients carrying a higher PPP2CA expression were predicted to a worse overall survival rate. Implementing all these

results, the protein phosphatase PP2A is a highly relevant and therefore potential target in the treatment of aggressive pancreatic cancer.

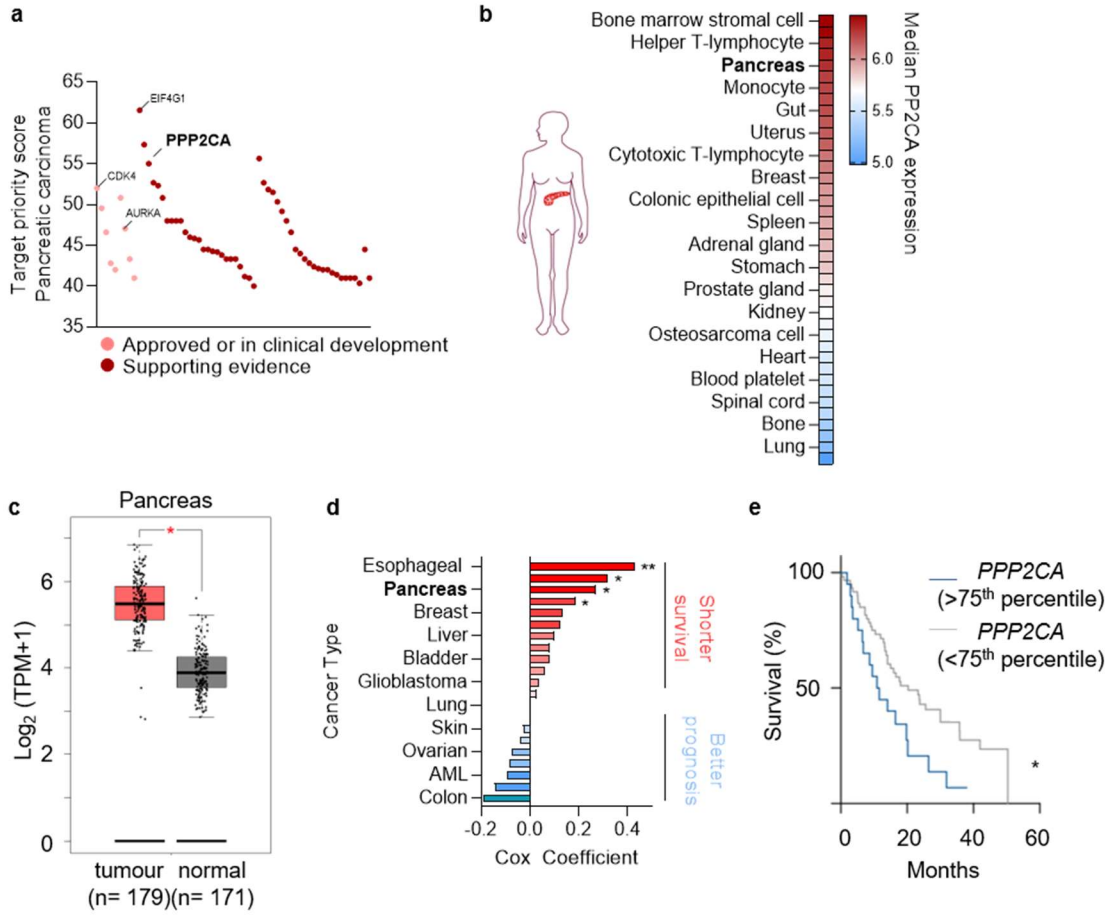

Figure 6 | PP2A is a highly relevant target in aggressive Pancreatic cancer

a, CRISPR/Cas9 Screens combined with patient genomic data and pathway annotations revealed possible targets for treating PDAC. Depicted are the priority scores from the Project score portal and highlighted is the Protein phosphatase 2A catalytical subunit as target with high supporting evidence. **b,** Colour-coded is the median PPP2CA expression in different organs, that were evaluated from the proteomics. dB website. **c**, PPP2CA mRNA expression (log_2 TPM+1) from tumour (n=179) or normal (n=171) pancreas tissue were accessed from the GEPIA portal (log2FC cut-off = 1, p-value cut-off = 0.01, match normal TCGA and GTEx data). **d,** Cox regression analysis of linked PPP2CA expression and TCGA survival data was done with the OncoLnc webtool in 21 cancer entities. **= <0.01, *= <0.05. **e,** Kaplan-Meier survival curves of patients with high (>75th quartile, blue) or low (<75th quartile, grey) PPP2CA expression. p-value: * = 0.02, log-rank test is indicated). Data was retrieved from [39] and curated as described [192]. The analysis was done with the help of Prof. Dr. Günter Schneider.

4.2 The mesenchymal subtype of PDAC is more sensitive to PP2A inhibition

4.2.1 PP2A inhibition in murine cell lines determines subtype specificity

To get more insights into PP2A related functions and determine possible biomarkers or relevant pathways for further combinatorial treatments, screening of *in vitro* PDAC model systems with the clinical-grade inhibitor LB-100 was done in a first step. For this, well characterised murine $Kras^{G12D}$-driven PDAC cell lines [37] were screened with the inhibitor and the cell viability and the half-maximal growth inhibition was determined (Fig. 7a). IC_{50} concentrations showed a high variability in all used cell lines, with a very sensitive (IC_{50} < 20µM), intermediate (IC_{50} between 20-60 µM) and a highly resistant group of cells (IC_{50} > 60 µM). To further determine potential selection criteria for inhibitor sensitivity, subgrouping of the cell lines was performed according to previous cluster formation [37]. The Cluster C1 represents all cell lines with mesenchymal morphology, a more undifferentiated histological grading and amplification of $Kras^{G12D}$, whereas the C2 Cluster is based on epithelial morphology, lower grading and less KRAS mRNA amplification. Interestingly, the C1 cluster shows higher sensitivity and lower cellular viability to LB-100 treatment when compared to the C2 cluster (Fig. 7b & c). This effect was additionally validated by colony formation assays, whereby also mesenchymal cell lines showed less ability to form cellular colonies after long term inhibitor treatment (Fig. 7d &e). By comparing all sensitivity data of the screened cells with the associated gene expression transcriptomic data, it was possible to establish a ranking of affected genes. For pre-ranking, a Pearson correlation coefficient was used and genes were analysed by gene-set enrichment analysis (GSEA) with the HALLMARK signatures afterwards. Positive enrichment scores go along with expression in more resistant cell lines, where negative scores predict genes leading to inhibitor sensitivity (Fig. 7f). Again, top negatively scored was the hallmark of epithelial to mesenchymal transition (EMT), underscoring the previous findings of phenotypic sensitivity. In line with that, also TGFβ and IL6/STAT3 signalling were found to be enriched in LB-100 sensitive cell lines, known as promoters of EMT [193,194]. Resistant cell lines are enriched in mTor signalling or p53-related pathways. These findings all together hint at different sensitivity across pancreatic cancer subtypes, where the mesenchymal one is more sensitive to PP2A inhibition by LB-100.

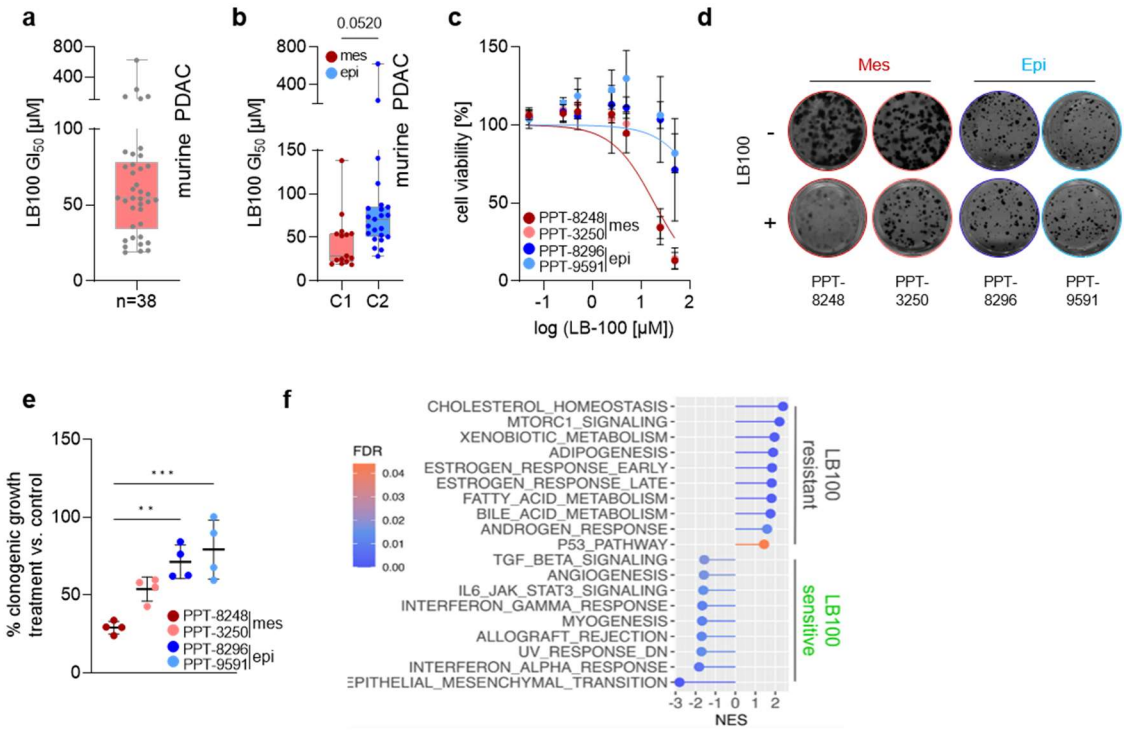

Figure 7 | Mesenchymal cell lines displayed a subtype specificity after LB-100 treatment

a, Depicted are the GI_{50} concentrations from murine $KRAS^{G12D}$-driven cell lines (n=38), determined by a 7-fold dilution screening approach with LB-100. Screening was done in cooperation with Daniel Göke. **b,** Comparison of GI_{50} values from **a** of the mesenchymal (cluster C1, red, n = 15) and epithelial (cluster C2, blue, n = 23) PDAC cell lines. *p* value of a Mann-Whitney test is indicated. **C,** Dose-response curves from treatment with LB-100 in a 7-point dilution of two epithelial (blue) and mesenchymal (red) cell lines from **b**. Cell viability was measured with CellTiter-Glo. Each dot represents the mean of three independent biological replicates in triplicates +/- SD. **d,** Clonogenic colony formation assay of LB-100 long term treated (14 days, 12.5 µM) mesenchymal (red) and epithelial (blue) cell lines from **c.** Pictures are taken by Daniel Göke. **e,** Quantification of minimum three independent replicates from **d** +/- SD, normalised to control. Displayed is the percentage of inhibition after treatment versus control. *p* asterisks from a Bonferroni one-way ANOVA are depicted (**= < 0.01, **= < 0.005). **f,** Gene expression from RNA sequencing data from murine $KRAS^{G12D}$-driven cell lines (n=38) were correlated with the corresponding GI_{50} values, using the Pearson correlation coefficient. Depicted are the HALLMARK signatures after a pre-ranked GSEA analysis. Represented are the normalised enrichment scores (NES) and the color-coded false discovery rate (FDR). Analysis was done in cooperation with Carolin Schneider and Prof. Dr. Günter Schneider.

4.2.2 Isogenic cell lines reflect phenotypic responses

To further validate the phenotypic sensitivity to LB-100 treatment, an isogenic cell line was used. For that, the cell line was separated into the mesenchymal and epithelial phenotype due to a differential trypsinisation protocol, whereby all cells carry the same genetic background [37] (Fig. 8a). Therefore, a direct correlation of cellular phenotypes to drug sensitivity is possible [195]. In line with the previous findings, the mesenchymal subtype of the isogenic cell line displayed higher sensitivity to PP2A inhibition in the cell viability or colony formation assay as compared to the epithelial opponent (Fig. 8b-d). With that, supporting evidence of a more LB-100-sensitive mesenchymal PDAC subtype exist.

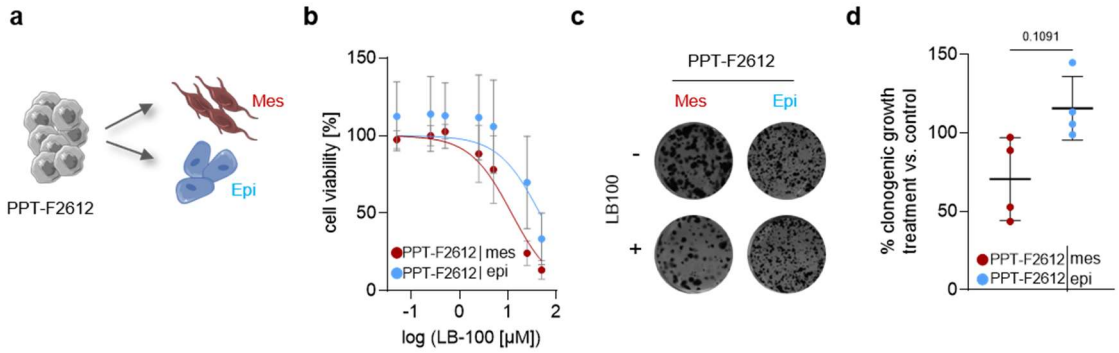

Figure 8 | Isogenic subtypes confirm mesenchymal sensitivity

a, Schematic representation of the isogenic cell lines. Both subtypes (epithelial ($F2612_{epi}$) and mesenchymal ($F2612_{mes}$)) carry the same genetic background, only a phenotypic separation due to differential trypsinisation was achieved. **b,** Cell viability from the cell lines from **a** was determined in a 7-point dilution with LB-100. Displayed is the cell viability with normalised response curves (GI_{50mes} = 9 µM, GI_{50epi} = 32 µM), each dot represents the mean +/- SD of minimum three independent replicates. **c,** Representative images from a clonogenic colony formation assay from the cell lines from **a** treated with 12.5 µM LB-100 for two weeks. **d,** Quantification of four independent biological replicates from **c** +/- SD. *p* value from a two-tailed paired t-test is indicated. Pictures were taken by Daniel Göke, colony formation and cell viability was determined in co-operation with him.

4.2.3 Cross-validation in human model systems and patient-derived organoids

Although there are a lot of similarities between human and mice and the mice serve well as model system for human disease with predictable genetic drivers, there are also significant limitations and physiological differences between these organisms [196]. To overcome this hurdle, a cross-validation of our previous findings was further validated in human conventional (human PDAC) and primary patient-derived cell lines (PDCL), as well as additional 3D patient derived organoids (PDO). PDO's are directly retrieved from PDAC patient biopsy samples as previously described [156]. Screening of the conventional human PDAC cell lines revealed a broad spectrum of growth inhibitory concentrations. Interestingly, the mesenchymal classified MIA PaCa-2 cell line was discovered as the most sensitive one, whereas the "classical" epithelial cell lines (HUPT4, HPAC or PATU8988S) are more resistant [197] (Fig. 9a). To further validate this finding, RNA sequencing data was evaluated for Vimentin (*VIM*) and E-catherin (*CDH1*) expression in these cell lines and correlated with the corresponding GI_{50} values using a Spearman coefficient (Fig. 9b&c). Sensitive cell lines displayed higher mesenchymal marker genes and the trend to negatively correlate, whereas resistant ones expressed more epithelial genes and had a positive correlation coefficient. To include not only conventional human cell lines, accessory primary patient-derived cell lines were screened with LB-100 and Phendione, another new PP2A inhibitor [198]. Screening with LB-100 resulted in a highly sensitive and resistant group (Fig. 9d). Whereas colony formation assay aided these findings (Fig. 9e&f), protein expression data again revealed the phenotypic differential response to LB-100 treatment (Fig. 9g). For the most cell lines from the sensitive group (<26µM LB-100), high Vimentin protein expression could be detected, whereas this accounts only for one of the resistant ones (Fig 9g & S9g). Additional screening of the same cell lines with Phendione (Fig. 9h) confirmed subtype drug-specificity. Sensitive cell lines of LB-100 showed overlapping sensitivity with the second PP2A-inhibitor Phendione (Fig. 9i) in low µM-range, which was further demonstrated with the colony formation assay (Fig. 9j)

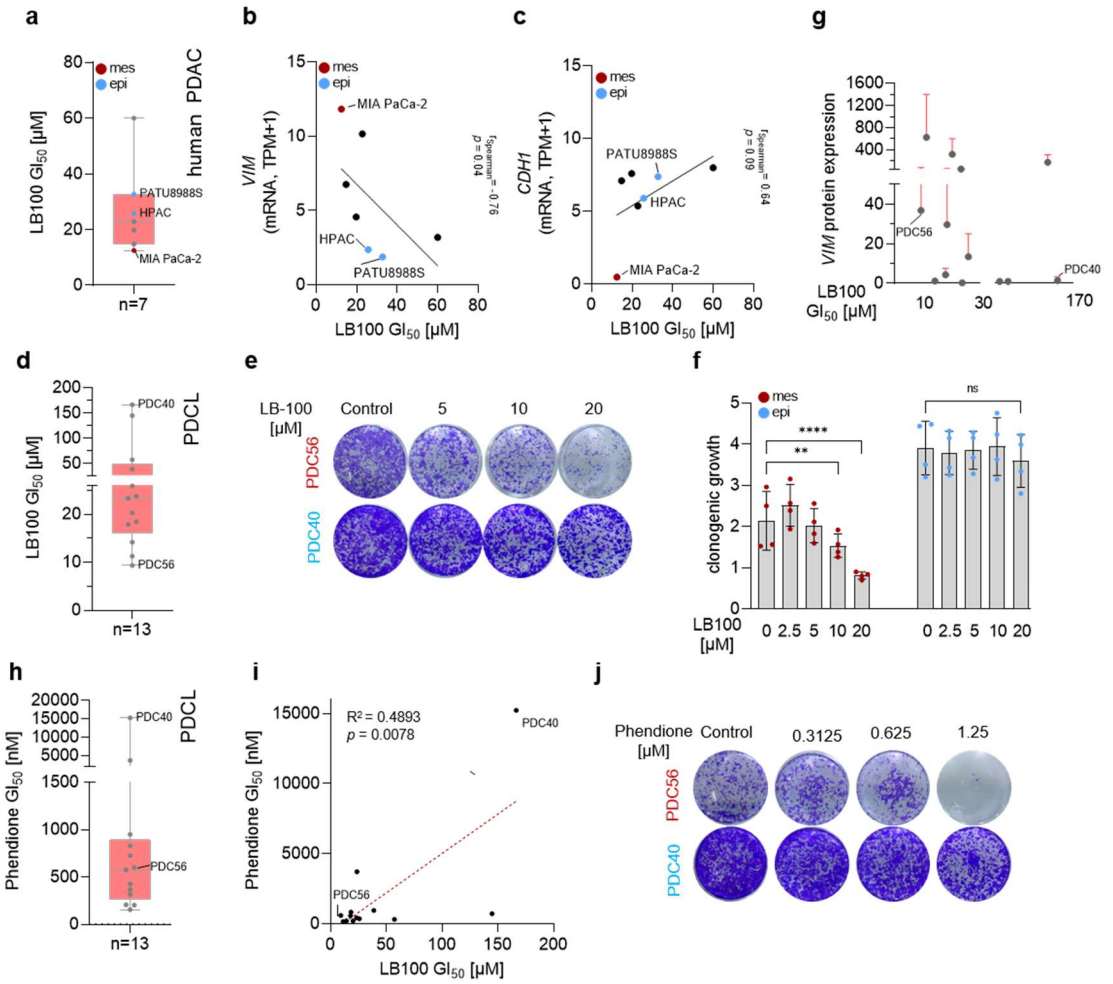

Figure 9 | Cross-validation in human systems validates subtype specificity

a, Displayed are the GI50 values of human conventional PDAC cell lines (n=7), determined by a 7-fold dilution treatment with LB-100 for 72h and analysis with CellTiter-Glo and by non-linear regression afterwards. Each treatment was done in minimum three technical and biological replicates. Highlighted are clear mesenchymal (MIA PaCa-2) and classical (HPAC, PATU8988S) cell lines[197]. Screening was done in cooperation with Daniel Göke. **b,** GI50 values were correlated with Vimentin (*VIM*) gene expression from publicly available datasets from the Depmap portal (21Q3). Highlighted are the cell lines described in **a**. Spearman correlation coefficient and *p* value are indicated. **C,** Same analysis as in **b** with the E-cadherin gene expression (*CDH1*). **d,** Screening of primary patient derived cell lines (n=13) as described in **a**. Labelled are the most sensitive and resistant cell lines. **e,** Representative images from clonogenic colony formation assay from the most sensitive and resistant cell line after treatment with LB-100 for 14 days with the indicated concentrations. **f**, Quantification of two independent experiments in duplicates from PDC56 (red, mesenchymal) and PDC40 (blue, epithelial). **g,** Vimentin (Vim) expression was determined in all screened PDCL by Western Blot and normalised to one cell line. Indicated are the relative expression with the corresponding GI50 value from **d** +/- SD**. h,** Cell lines from **d** screened with Phendione in a six-fold dilution. GI50 concentrations were determined after 72h by CellTiter-Glo and a non-linear regression analysis**. I,** Corresponding GI50 values from **d** and **h** were analysed by a simple linear regression. Dashed line: regression line. R^2= 0.4893, *p* = 0.0078. **j,** Clonogenic colony formation assay. One representative image out of three independent experiments is shown.

The major bottleneck in the drug discovery process from early research to clinical implementation is mainly promoted due to inadequate modelling systems. In the last years, 3D cell cultures, directly retrieved from patients material, have the potential to overcome this hurdle [199]. We therefore implemented 14 patient derived organoids from PDAC biopsies in the screening system with LB-100. Again, the PDOs displayed a variation from really sensitive, intermediate and resistant ones (Fig. 10a&b). By comparing RNA sequencing data of the sensitive quartile of the PDOs to the rest, the HALLMARK of epithelial-to-mesenchymal transition turned out to be highly enriched in the sensitive group (Fig. 10c). Altogether, also the cross-validation in human and patient-derived model systems promotes a subtype specific sensitivity of LB-100 as well, constituting for a useable patient stratification in the future.

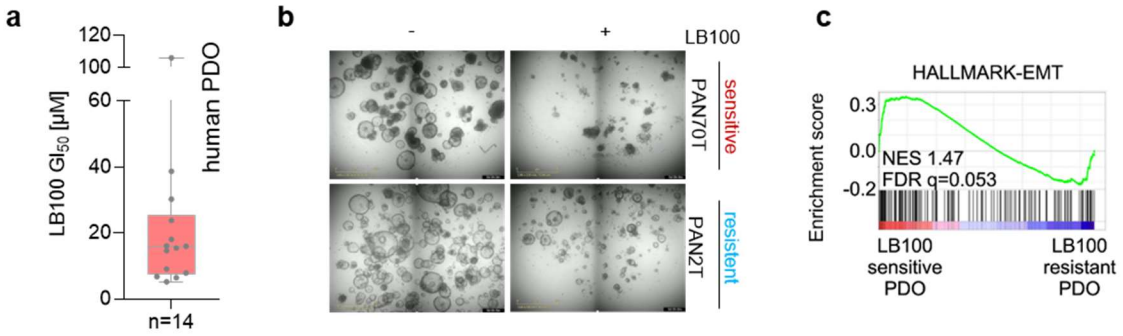

Figure 10 | PDO's screened with LB-100

a, 3D patient derived pancreatic organoids (PDO, n=14) were screened in a 9-fold dilution with LB-100 for 72 h and cell viability determined by CellTiter-Glo. Each dot represents the mean of three independent biological and technical replicates. Screening of the PDO was done in cooperation with Felix Orben. **b**, Representative images from PDO's treated with LB-100 (13.3 µM) or vehicle control for 5 days. Scalebar = 900 µM. Pictures were taken by Constanza Tapia Contreras in the framework of the KFO5002. **c,** Gene expression from the sensitive quartile of PDO from **a** displayed enrichment of the HALLMARK-EMT signatures in a GSEA analysis. False-discovery rate (*q*) and the normalised enrichment score (NES) are indicated.

4.3 Investigation in the LB-100 induced cell death in PDAC

4.3.1 Programmed cell death induction by apoptosis

From all drugs, that are enclosed in clinical trials, approximately only 8 % get approved by the FDA afterwards [200]. Therefore it is necessary to know more about the mechanism of action of the drug to increase the likelihood of certification beforehand [200]. As shown in the previous chapters, PP2A represents a highly interesting target in PDAC, especially for the mesenchymal subtype. By using the clinical grade inhibitor of PP2A (LB-100), both, the mechanism of action and further relevant PP2A-related pathways can be elucidated. For that, $KRAS^{G12D}$-driven murine cell lines were treated with the inhibitor LB-100 over a period of time. Already after two to four hours, a phenotypical change from the mesenchymal shape to rounded cells could be detected and was more prominent after 6 hours of treatment time (Fig. 11a, mesenchymal cells). In contrast to that, the epithelial cell lines showed a weaker response in the phenotypical changes and recovered already after six hours of treatment (Fig. 11a, epithelial cell line). To clarify a possible connection of the rounded phenotype with programmed cell death, apoptosis was measured with the Annexin V / PI staining (Fig. 11b). Whereas viable cells have no Annexin/PI staining, Annexin V can bind to exposed phosphatidylserines on apoptotic cells. In later stages, when the cell membrane gets disintegrated, PI can also enter the nucleus, stain DNA and mark late apoptotic cells. After treatment with LB-100, a significant increase in early and especially late apoptosis (Fig. 11b&c) could be detected in the mesenchymal subtype and is absent in the epithelial cell line. This finding could further be cross-validated in human mesenchymal MIA PaCa-2 cells, where treatment with LB-100 led to apoptosis specific induction of cleaved PARP (Fig. 11d). These results demonstrate, that LB-100 acts rapidly in the short time frame of six hours and leads to death by apoptosis only in the mesenchymal subtype.

4.3.2 Intracellular stress response after LB-100 treatment

4.3.2.1 ER stress destructs the cellular homeostatic system in mesenchymal cells

The discovery of stress granule formation after LB-100 treatment pointed to an emerging stress situation in the cell, which could be pursued further. Stress granules are membraneless cell compartments, where translationally stalled mRNAs, RNA-binding proteins or translation initiation factors are stored

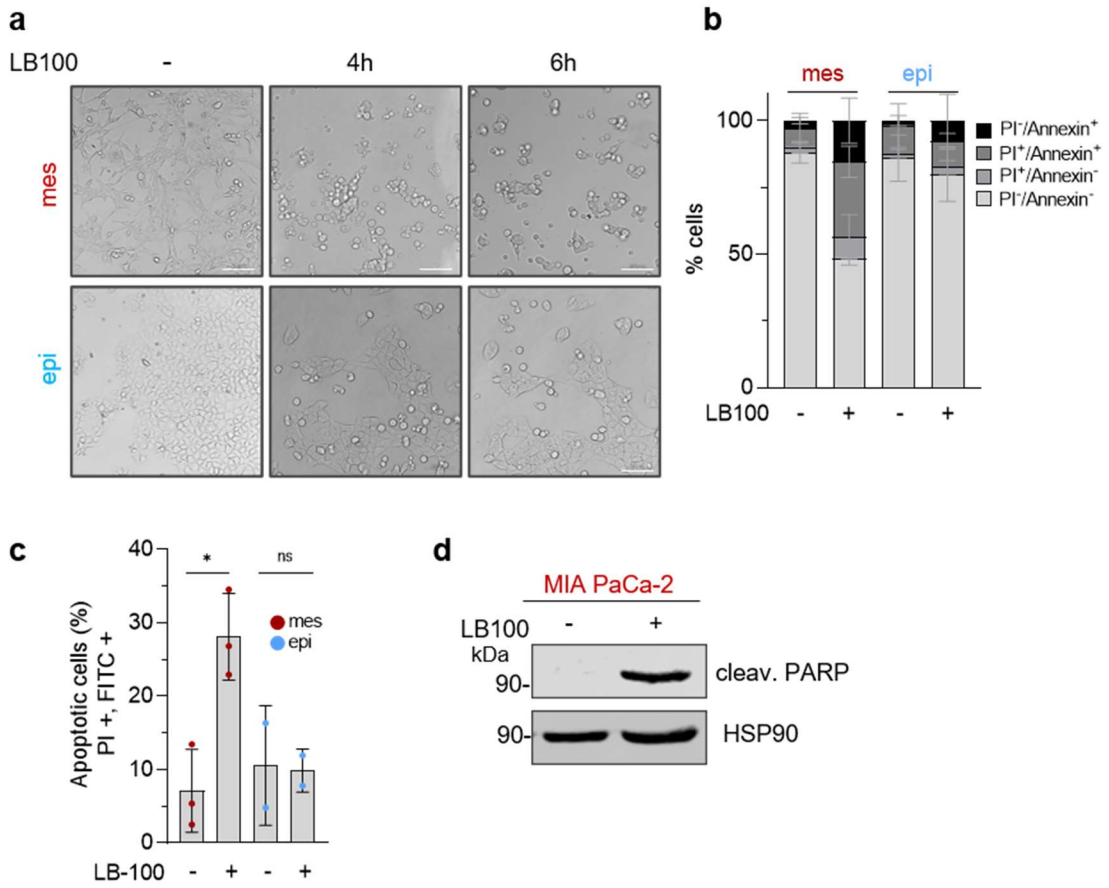

Figure 11 | LB-100 led to apoptosis in the mesenchymal subtype

a, Representative images from treatment with LB-100 in a mesenchymal and epithelial cell line after four and six hours of treatment time (20 µM LB-100, scalebar= 100 µM). **b,** Annexin V/ PI apoptosis measurement was done in epithelial and mesenchymal cell line after six hours of treatment (20µM LB-100). Displayed are the percentage of cells in the respective cluster with standard deviation (viable = Annexin-/PI-, early apoptosis = Annexin+/PI-, late apoptosis = Annexin V+/PI+, necrotic= Annexin-/PI+, n≥2). Annexin/PI analysis was done in cooperation with Carolin Schneider. **c**, Late apoptotic cluster (Annexin+/PI+) from B. *p*= 0.0213, Tukey's multiple comparison test, n≥2, +/- SD). **d,** Western Blot detection of cleaved PARP in human MIA PaCa-2 cells after treatment with LB-100 for six hours (10µM). HSP90: loading control. One representative Blot out of three experiments is shown.

in response to stress stimuli [201]. Staining of stress granules (SG) by the T-cell intracellular antigen-1 (TIA-1) revealed a dramatic increase in SG formation after already four hours of treatment with LB-100 in the mesenchymal subtype. Interestingly, epithelial cells showed even higher levels already under untreated basal conditions, but no further increase afterwards (Fig. 12a & b & c). Altogether, treatment with LB-100 induced a stress reaction in the cell.

To restore cellular homeostasis and alleviate the stressed condition, the integrated stress response (ISR) serves as the main stress defence after amino acid depletion, glucose

deprivation, viral infection, hypoxia, heme deficiency, ROS, DNA damage or also intrinsic stress from the endoplasmic reticulum (ER) [202,203]. It reduces stress and leads to restoration of the cellular homeostasis by the induction of stress granules, autophagy or also apoptosis after prolonged stress states [204]. The core event occurring in this pathway is the phosphorylation of p-eiF2α [203], which was indeed upregulated in both phenotypes after treatment with LB-100, facilitate an activation of the ISR. However, the endoplasmic reticulum stress markers like ATF4, ATF6, p-IRE1 or the ER chaperone BIP were only selectively induced in the mesenchymal subtype, both in human and murine systems (Fig 12 d & e murine system, Fig. 12 f & g human validation). This finding highlights a cell-identity-specific activation of the ISR pathway by ER stress and underscores the stress induction after LB-100 treatment specifically in the mesenchymal cells.

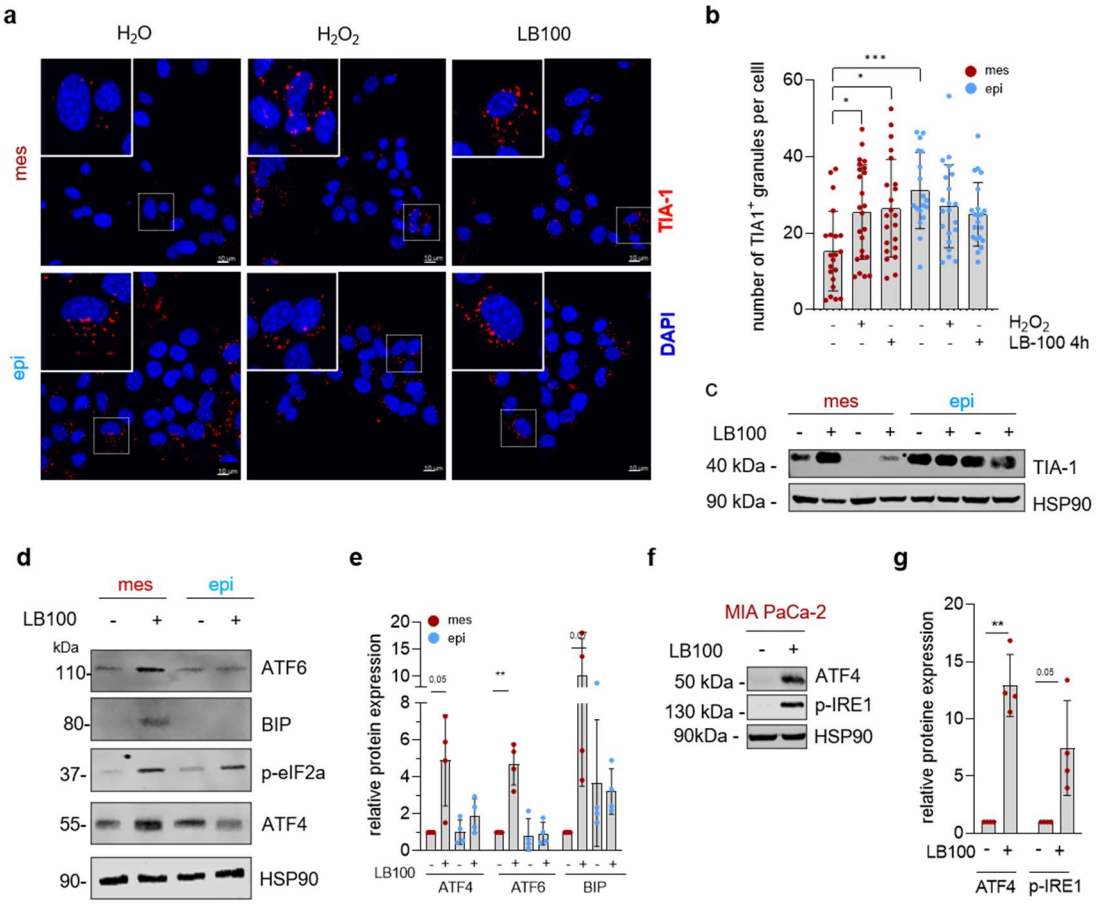

Figure 12 | Intrinsic stress led to activation of the ISR after LB-100 treatment

a, Representative images of the IHC staining of the T-cell intracellular antigen-1 (TIA-1) after four hours of treatment with LB-100 (20 µM) in mesenchymal (n=2) and epithelial (n=2) cell lines. H2O2 serves as positive control (1.5 mM, 24h). The nuclei are stained with DAPI. Scalebar = 10µM. **b,** Quantification of three independent replicates in two mesenchymal and epithelial cell lines from **a** +/- SD. TIA1 expression was normalised to DAPI signal. * = < 0.05, ***= <0.001, analysed with a Bonferroni multiple comparison test. **c,** Western

Blot of the TIA-1 protein in two mesenchymal and epithelial cell lines after six hours of LB-100 treatment (20µM). HSP90: loading control. One representative blot out of three experiments is shown. **d,** Representative Western blots from the main ISR and ER stress related pathways after six hours treatment (20µM). HSP90: loading control. n=3. **e,** Quantification of independent experiments from **d** (n≥3) +/- SD. **= 0.0073, other *p* values are indicated, analysed with a two-sided paired t-test. **f,** Western Blots of ATF4 and p-IRE1 after treatment with LB-100 (six hours, 10µM) in the mesenchymal MIA PaCa-2 cell line. HSP90: loading control. One representative blot out of three experiments is shown. **g,** Quantification from **f** from independent biological replicates (n=4) +/- SD. *p* values: **=0.0031 or indicated, analysed with a two-sided paired t-test.

4.3.2.2 Reduced mitochondrial function additionally promotes homeostatic imbalance

The three main apoptotic pathways that are known so far result from an extrinsic death receptor (DR) pathway, the intrinsic ER stress initiation pathway or from the mitochondrial damage pathway [205]. In healthy cells, the ER and mitochondria normally form structural networks (mitochondria-associated ER membranes [MAMs][206]) to maintain the cellular homeostasis and determine the cell fate [207]. Since we observed apoptosis and ER stress in the previous results (Fig. 11 & 12), a mitochondrial dysfunction could also contribute to the observed death response. Additionally, a gene set enrichment analysis of unbiased RNA sequencing data of the mesenchymal cells after LB-100 treatment showed a high depletion of metabolic pathways (Fig. 13a). To investigate in the mitochondrial apoptosis pathway, several pro-apoptotic effector proteins like Cytochrome c (*Cycs*), BAK or PUMA (*BBC3*) were verified in human and murine cellular systems (Fig. 13b-f). Overall, a high induction of all these effector proteins could be detected in the mesenchymal subtype after LB-100 treatment, either on mRNA or protein level and were absent or only low induced in the epithelial cell line. Mitochondrial fusion and fission are a critical determinant for cellular function and also for the stress response, whereby dysfunctional mitochondria are characterised by abnormal fission or fusion events [208]. By staining mitochondria with the mitoTracker® deep red substance, a differential pattern between mesenchymal and epithelial cells was detected. Mesenchymal cells showed a clear mitochondrial perinuclear clustering around the nucleus after already two hours of treatment, which was not visible in the epithelial cell lines (Fig. 13 g). To further strengthen the finding of dysfunctional mitochondria and determine the activity of the respiratory chain, a Seahorse assay was accomplished. For this, the oxygen consumption rate (OCR) and the extracellular acidification rate (ECAR) was analysed in a mitochondrial stress test with a Seahorse XF analyser. Indeed, treatment with LB-100 lead to a time-dependent reduction of the OCR and therefore a reduced ATP production and maximal respiration capacity of the mitochondria, selectively in the mesenchymal

subtype (Fig. 13 h-l). Overall, these results suggest an impaired function of the mitochondria after LB-100 treatment in the mesenchymal subtype.

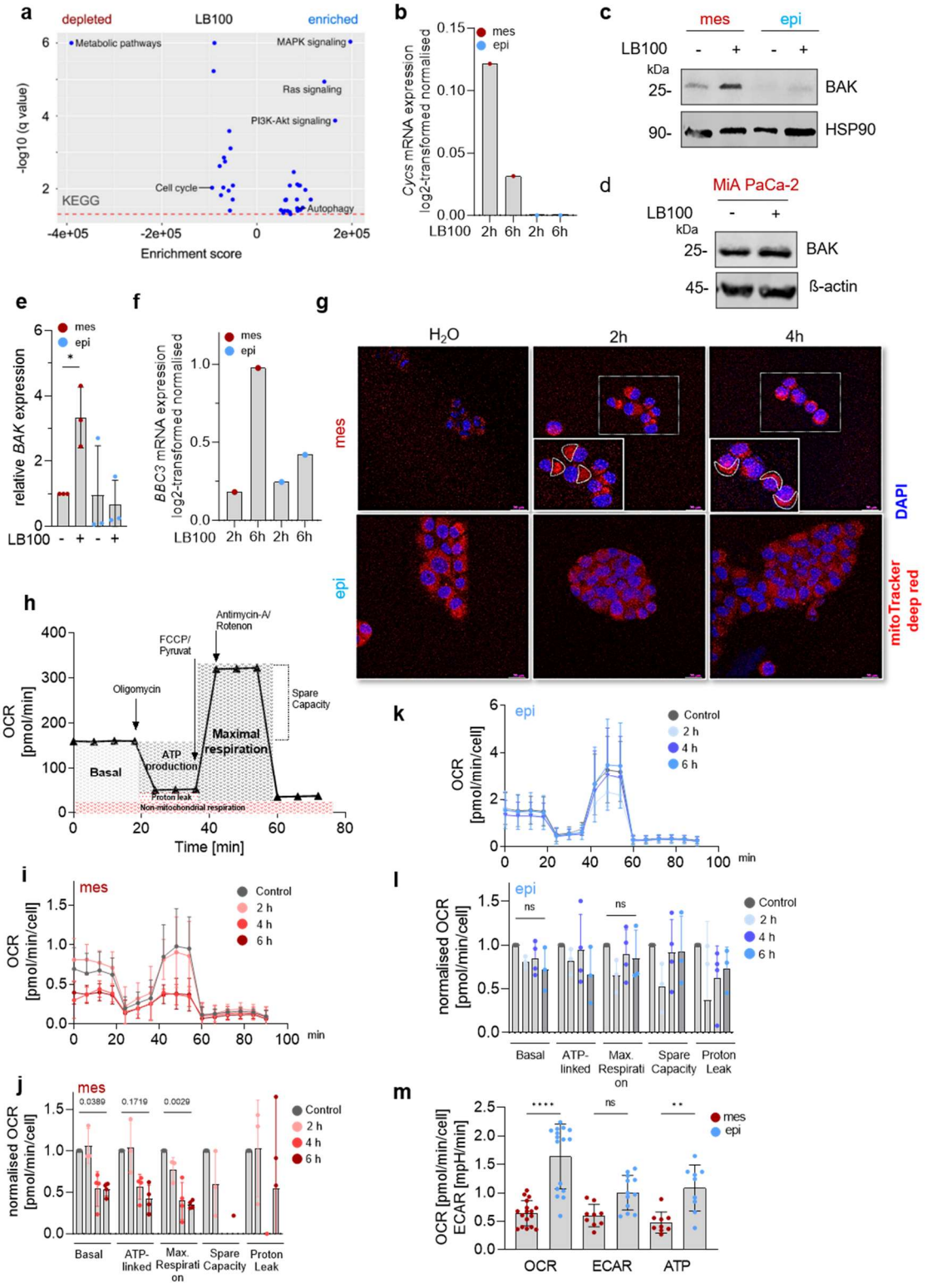

Figure 13 | Promotion of homeostatic imbalance through mitochondrial dysfunction

a, GSEA analysis of mRNA expression data of the mesenchymal cell line after treatment with LB-100 for six hours. Depicted are the enriched and depleted KEGG signatures with the corresponding enrichment scores and q-values ($-\log_{10}$). **b,** mRNA expression ($\log_2$FC) of Cytochome C (*Cycs*) in the mesenchymal and epithelial cell line after two- and six-hour treatment with LB-100. **c,** Western Blot analysis of BAK expression after a six hour LB-100 treatment in murine epithelial and mesenchymal cell lines (20µM). HSP90: loading control. One representative blot out of three experiments is shown. **d,** BAK western blot analysis of the human mesenchymal Mia PaCa-2 cell lines after six hours of treatment with LB-100 (10µM). ß-actin: loading control. One representative blot out of three experiments is shown**. e,** Quantification of three independent replicates of c +/- SD**,** * = 0.0488, two-tailed paired t-test. **f,** mRNA expression ($\log_2$FC) of the pro-apoptotic effector protein PUMA (*BBC3*) in the mesenchymal and epithelial cell line after two- and six-hour treatment with LB-100. **g,** Representative images of the mitochondria by mitoTracker® staining in an epithelial and mesenchymal cell line after two- and four hours of treatment with LB-100. Scalebar= 20 µM. Zoomed pictures are highlighted with dashed lines in the original picture. **h**, Schematic representation of the Mito stress OCR measurement and the calculated parameters. Figure according to [209]. **i,** Oxygen consumption rate of the Mito stress-test measurement in the mesenchymal cell line after two, four and six hours of LB-100 treatment. SD of replicates is indicated (n≥3). J**,** Quantification of minimum three independent replicates of **i** of the basal respiration, ATP-linked production, maximal respiration, spare capacity and proton leak. p-values are indicated +/- SD. **k** & **i,** same measurement and analysis as in **i** & **j** for the epithelial cell line. **m,** Basal values of the OCR, ECAR and ATP production of the mesenchymal and epithelial cell line from **i** and **k** +/- SD**.** ****= <0.0001, **= 0.01 of an ordinary one-way ANOVA with Bonferroni's multiple comparison. The seahorse assay was done in cooperation with Michael Dudek.

4.3.2.3 Autophagy as homeostatic rescue process

As described above, the ISR can also induce autophagy to regenerate the cell homeostasis after stress induction. Additionally, in an unbiased RNA sequencing of the mesenchymal subtype after treatment with LB-100, autophagy was one of the major upregulated and enriched hallmarks in a GSEA analysis (Fig. 13a). These two findings prompted further investigation in the autophagy process. Autophagy itself is activated by an initiation complex, consisting of ULK1/Atg1 and signalling from the energy sensor kinase AMPK, resulting in the elongation of the phagophore. The further steps of maturation include two ubiquitin-like conjugation systems (Atg12/Atg5/Atg6 and Atg8/PE/LC3 I/II), leading to the complete closing of the phagophore and autophagosome formation. In the end, fusion of the autophagosome with lysosomes is necessary for degradation of cytoplasmic components [210]. According to this autophagy induction process, all major steps were addressed. First, upregulation by phosphorylation of AMPK T172 could be detected in both subtypes after treatment with LB-100, but downstream reduction of the inhibitory phosphorylation of ULK1 S757 and therefore activation of ULK1 was selectively induced in the mesenchymal subtype (Fig. 14a). As next initiation step of the maturation of the phagosome, Atg12 mRNA was upregulated more than twofold in the mesenchymal cell line as compared to the epithelial line (Fig. 14b). Immunoblotting of the second autophagosome marker LC3 I/II revealed the similar pattern and autophagy was only induced in the mesenchymal cell line (Fig. 14c&d). Interestingly, also the human mesenchymal MIA PaCa-2 cell line showed an induction of autophagy after LB-100 treatment, whereby after six hours only the first cytosolic form of LC3 (LC3-I) increased (Fig. 14e&f). Lysosomes, which are formed at the end of the autophagy process, were stained with an LysoTracker® staining. The LysoTracker selectively stains the acidic compartments (lysosomes) in living cells. As positive control, treatment with Chloroquine was used, since Chloroquine is best known to inhibit autophagy, leading to an accumulation of lysosomes [211]. Indeed, a high induction of lysosomes could be detected in both cell lines after Chloroquine treatment, but LB-100 induced lysomes exclusively in the mesenchymal subtype (Fig. 14g&h). All in all, autophagy was induced in the stressed mesenchymal cell lines and could be an additional attempt to restore the homeostatic balance by removing damaged organelles.

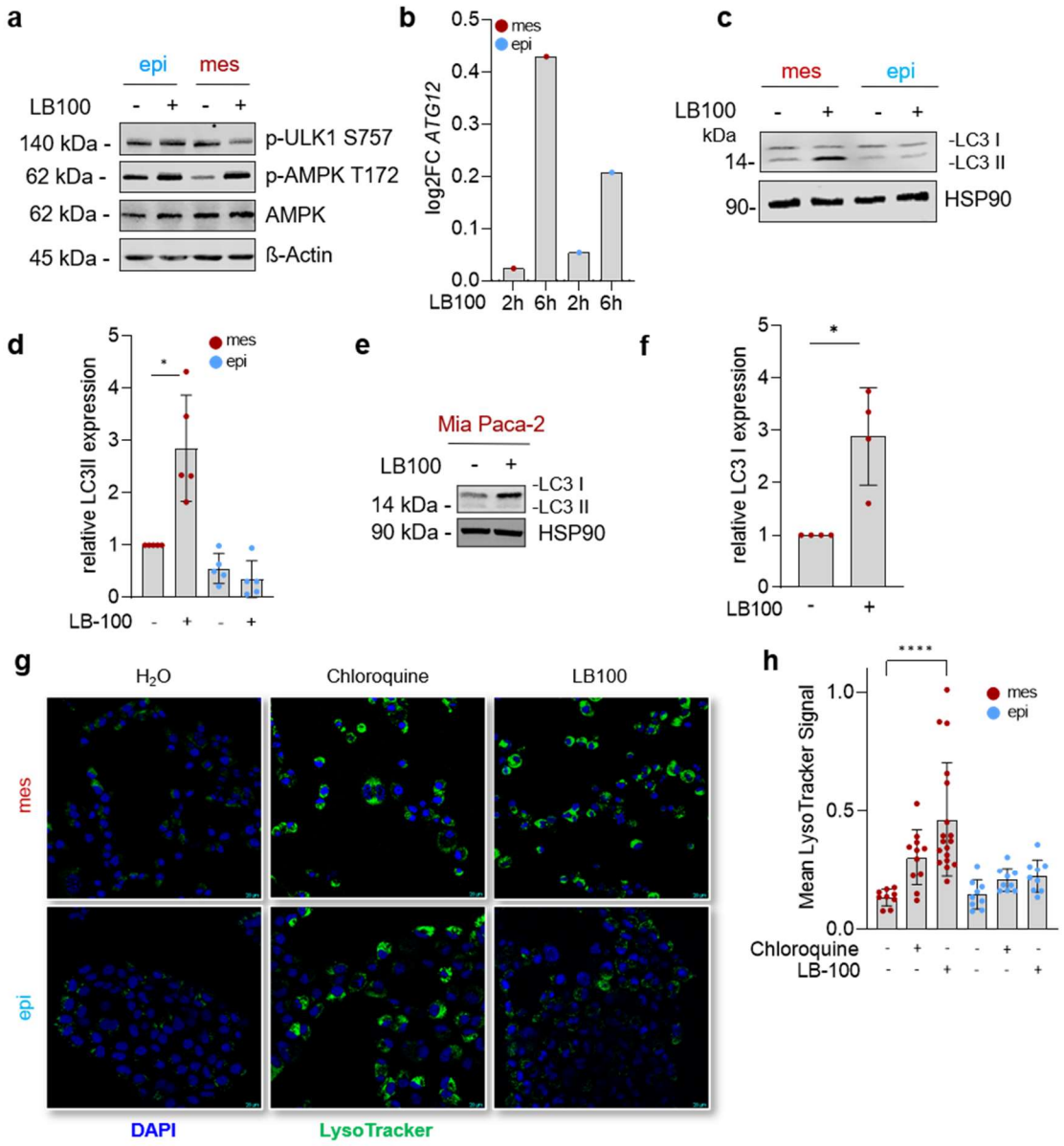

Figure 14 | Autophagy as attempt to restore cellular homeostasis

a, p-Ulk1 S757 (inhibitory phosphorylation), p-AMPK T172 and AMPK western blot analysis of a murine epithelial and mesenchymal cell line after treatment with LB-100 for six hours (20 µM). Representative blots of three independent replicates are shown. **b,** mRNA expression (log_2FC) of ATG12 in the mesenchymal and epithelial cell line after two- and six-hour treatment with LB-100. **c,** Representative blots of western blot analysis of the autophagy marker LB3 I / II (LB-100 20 µM, 6 hours). HSP90: loading control. n=5. **d,** Quantification of **c**, each dot represents one out of four independent replicates +/-SD, *= 0.015, two-tailed paired t-test. **e**, LB3 I / II western blot analysis in the mesenchymal Mia PaCa-2 cell lines after LB-100 treatment (10 µM, 6 hours). One representative blot out of four independent experiments is shown. **f,** Quantification of **e** of four independent experiments +/- SD (* = 0.0272, two-tailed paired t-test). **g,** Representative images of the LysoTracker® staining (green) in mesenchymal and epithelial cell lines after LB-100 (6h, 20 µM) and Chloroquine (24h, 20 µM) treatment. Chloroquine represents the positive control. **h,** Quantification of the mean Lysotracker® signal from **g** in relation to the corresponding DAPI signal +/- SD (n =3, ****= <0.0001, Bonferroni's multiple comparison).

4.4 Mechanistic insights into the mode of action of LB-100

4.4.1 CRISPR-drop out screen identifies sensitivity profiles

To discover the potential mechanism of action of LB-100, pooled CRISPR-Cas9 dropout screens are a powerful tool to detect the genetic underpinnings and the sensitivity profiles that confer resistance to the drug [212]. For this, the optimized pooled CRISPR Brunello guide RNA library [213] was lentivirally transferred into the human mesenchymal, stable Cas9-expressing MIA PaCa-2 cell line, thereby covering over 19.000 genes (Fig. 15a). These gene-edited cells, which carry mostly only one single genetic perturbation per cell, were challenged afterwards with the LB-100 drug treatment or vehicle control for 14 days at an GI_{30} concentration. The surviving cells are then pooled, the sgRNA isolated, sequenced and the representation bioinformatically analysed with the MAGeCKFlute pipeline, to calculate the respective beta scores (Fig. 15a). A positive beta score indicates genetic resistance and a selective advantage to the drug treatment, whereas a negative score depicts synergistic and synthetic lethal genes [174,212]. By analysing the beta scores of the vehicle and LB-100 treated MIA PaCa-2 cells and subtracting the first from the second, high delta beta scores (>1.5, resistance) and very small ones (< -1.5, synthetic lethal) could be detected and filtered as relevant for this experiment (Fig. 15b). To uncover the underlying molecular interactions and relation networks of the affected genes, a GSEA pathway analysis was performed (Fig. 15c&d). Whereas genes conferring synthetic lethality are connected to EMT and hypoxia, resistance genes are related to the oxidative phosphorylation, myc and E2F targets or the unfolded protein response in the HALLMARK analysis (Fig. 15c). Gene ontology showed no connection of resistance genes to pathway annotations, but interconnected resistance to splicing, translation and transcription (Fig. 15d). Network association tools have become powerful to identify protein-protein interactions and intracellular signalling pathways [214,215] and were therefore accomplished for the twenty highest ranking genes of resistance and synthetic lethality connection (Fig. 15e&f). Interestingly, while there was no STRING network detectable between the synthetic lethal genes (Fig. 15f), the resistance genes clustered around three main triggering nodes: CDK9, as the main transcriptional regulator, TUFM as the mitochondrial translation elongation factor and highest scored gene in the screen and third mitochondrial ribosomal proteins (Fig. 15e).

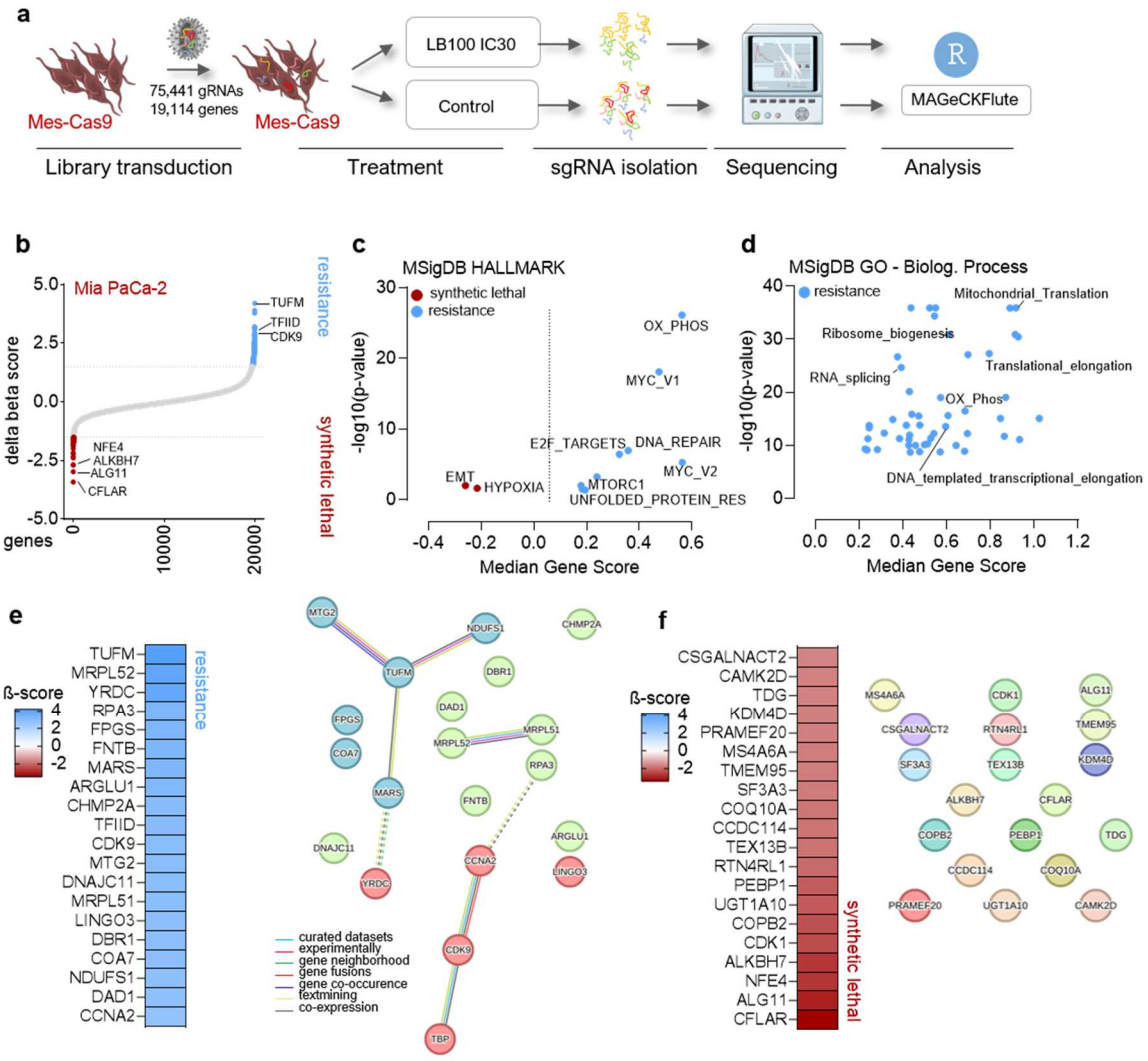

Figure 15 | CRISPR Drop out screen identifies LB-100-triggering nodes in human cells

a, Schematic representation of the CRISPR screen performance. Human MIA PaCa-2 cells, which are stably express Cas9, were lentiviral transduced with the pooled Brunello sgRNA library, covering over 19.000 genes. Cells were challenged afterwards either with vehicle control or LB-100 (GI_{30}, 5 µM) over 14 days. Remaining cells were pooled, sgRNAs isolated and analysed with the MAGeCKFlute pipeline after sequencing. **b,** All identified genes and the corresponding delta ß-score (ß score Treatment- ß score Control). Negative scores (red) indicate synthetic lethal genes after LB-100 treatment, positive scores (blue) represent resistance genes. Threshold: ±1.5. The screen was done in cooperation with Matthias Wirth, Hazal Köse and Ulrich Keller. **c,** GSEA analysis with the MSigDB HALLMARKS of the pre-ranked delta ß-scores. Indicated are the media gene score and the corresponding -log10(p-value) of the synthetic lethal or resistance enrichments. **d,** Illustrated are the MSigDB Gene ontology- Biological process enrichments from the analysis of **c. e,** left: Representation of the top 20 scored resistance genes and their corresponding delta ß-score. Right: STRING analysis of these genes. Cluster building by k-means clustering and indicated by colour (n =3). **f,** Top 20 genes accounting for synthetic lethality and their corresponding delta ß-score. Right: STRING analysis of these genes.

To corroborate the previous findings in a murine system as well, a second CRISPR-Cas9 dropout screen under LB-100 and additional under Phendione pressure was carried out in the murine mesenchymal, stable Cas9 expressing, PPT-9091 cell line (Fig. 16a). Overall, 37 overlapping genes favouring resistance and 1 gene (*PAF1*) facilitating synthetic lethality with the inhibitors could be detected overlapping in the three screens (Fig. 16b & c). Outstanding for favouring resistance was the previously detected *CDK9* (Fig. 16c). Gene set enrichment analysis with the KEGG database showed overlapping results with the previous findings, namely resistance gene sets were again enriched in ribosomal or transcriptional misregulation signatures (Fig. 16d).

Taken together these finding of all the screens, PP2A inhibition could trigger a transcriptional or splicing-dependent mechanism, accountable for the imbalance in the homeostatic systems and, in the end, death in the mesenchymal cells.

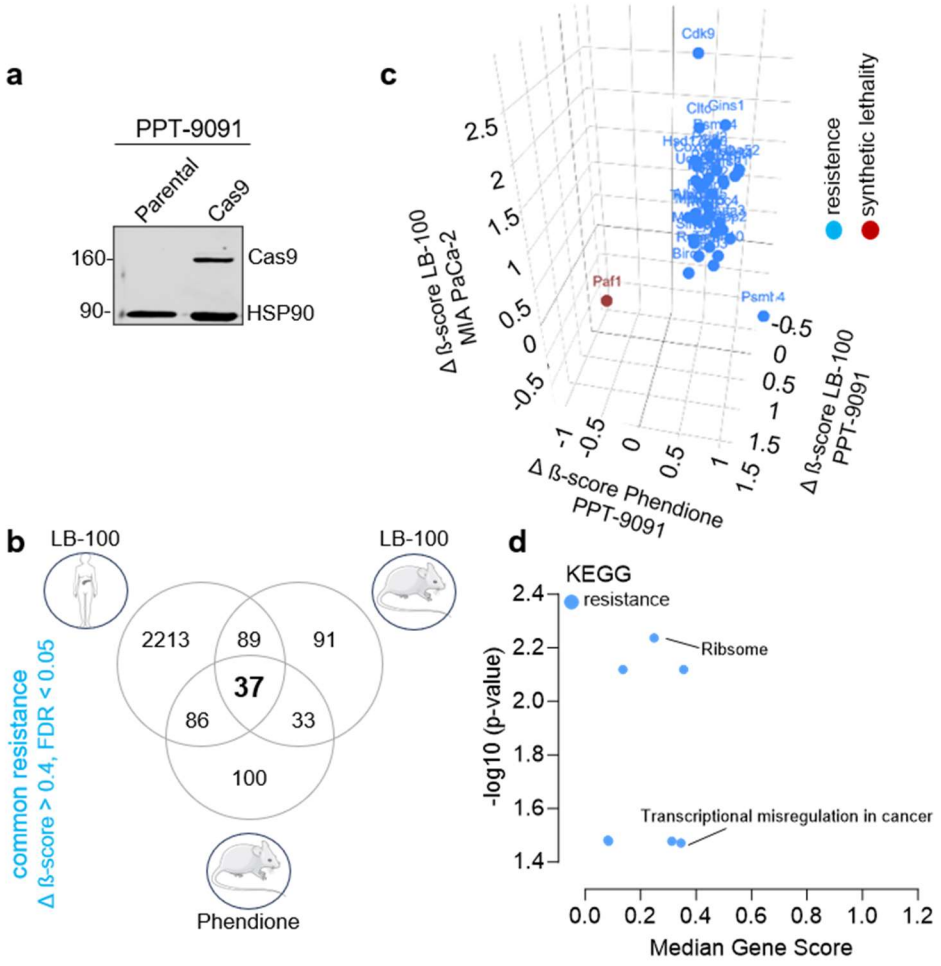

Figure 16 | Second Dropout screen confirms triggering nodes

a, Western Blot analysis of the parental and Cas9-expressing murine mesenchymal PPT-9091 cell line. HSP90: loading control. n=1. **b,** Venn analysis of all genes leading to inhibitor resistance in all three CRISPR screens (Δß-score > 0.4 & FDR < 0.05). 37 genes are overlapping. **c,** 3D plot illustration of the

Δß-scores of all significant (FDR < 0.05) overlapping synthetic lethal (Δß-score < -0.4, red, n = 1) and resistance favouring genes (Δß-score > 0.4, blue, n = 37) between the three screens. **d,** Overlapping genes were analysed using the Genetrail3 web interface and displayed are the KEGG signatures of resistance (blue) genes. The median gene score and -log10 (p-value) are indicated. Bioinformatical analysis was done with the help of Riccardo Trozzo.

4.4.2 Splicing as a secondary LB-100 effect

Since Splicing was found as one of the most prominent enriched gene signatures in LB-100 resistance genes in the previous CRISPR Cas9 dropout screens and is further described as one of the major regulators of cellular homeostatis and gene expression [216,217], investigation into mRNA gene expression and splicing changes was accomplished. For the analysis of splicing and gene expression changes, paired-end deep sequencing was applied and followed by bioninformatical analysis. Whereas in the log_2FC of expressed genes only low changes were detected in the epithelial cell line after two and six hours of LB-100 treatment, treatment in the mesenchymal cell line resulted in high gene expression turnovers already after two hours. This was even more prominent after six hours (Fig. 17a). Concordantly and discordantly induced genes can be detected by an overlay of all induced genes from the mesenchymal and epithelial cell line. Interestingly, big parts of LB-100 induced genes showed a concordant expression between the two phenotypes, but were more prominent and induced with higher turnoverrates in the mesenchymal cell line (Fig. 17 b&c). Splicing consists of many different isoformes, e.g. can differ by detained introns (DI), alternative polyadenylation sites (IPA), skipped exons in the transcript (SE), alternative 5' splice site (A5SS) or also alternative 3' splice sites (A3SS) [218] and all of them were analysed after two and six hours of LB-100 treatment in the mesenchymal and epithelial cell line. Whereas in the splicing isorms of the epithelial cell lines only mild changes could be detected, more then a 2.5 x increase was visible in the mesenchymal cell lines between two and six hours of treatment. Skipped exons were thereby the most prominent affected isoform, followed by A5SS and A3SS isoforms. Detained introns were hereby only affected in a minor amount (Fig. 17d). To discover, if the splicing changes are the main factors influencing the changed gene expression after two and six hours of treatment, an overlay from all expressed genes together with the corresponding measured splicing changes was made. Here it become clear, that all genes affected with splicing changes have only a low turnover rate. Genes with high gene expression and log2FC are barely ever affected by splicing changes. Taken together, high gene expression and splicing changes could

be detected only in the mesenchymal cell line, however, the massive splicing changes seem not be responsible for the significant major change in gene expression.

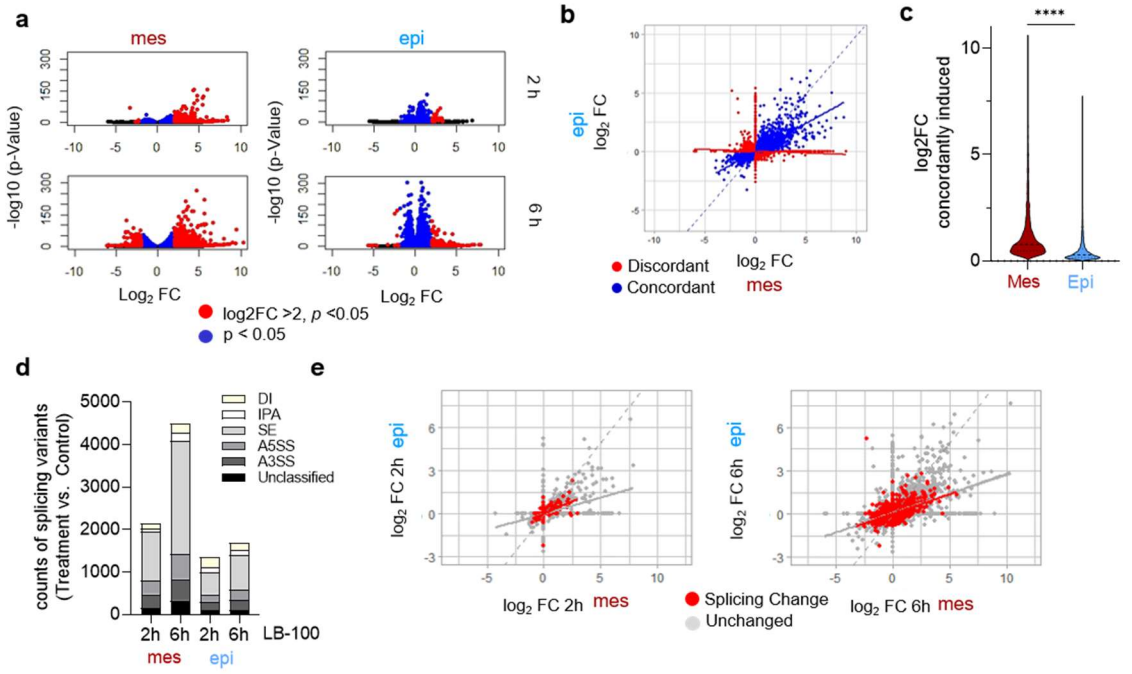

Figure 17 | Splicing does account secondary for major change in gene expression

a, Gene expression was determined by paired-end deep sequencing in mesenchymal (red) and epithelial (blue) cell lines after two and six hours of LB-100 treatment (20 µM). Displayed are the log_2FC values with the corresponding -log10 (p-values). Cobalt blue: all significantly changed genes ($p < 0.5$), Fiery red: significant genes with high log_2FC ($p<0.5$, log2FC >2). **b,** Overlay of all significantly changed genes (log_2FC) from the mesenchymal and epithelial cell line after six hours of LB-100 treatment. Cobalt blue: concordantly changes genes, fiery red: discordantly changed genes in one or the other cell line. Dashed line: hypothetical regression line. Solid line: actual regression line. **c,** Displayed are the log2FC from all concordantly expressed genes from **b** in the mesenchymal and epithelial cell line. ****=<0.001, two-tailed unpaired t-test. **d,** Counts of the different splicing variants after two and six hours of treatment (LB-100, 20 µM) in the mesenchymal (red) and epithelial (blue) cell lines. DI= detained introns, IPA= alternative polyadenylation, SE= skipped exons, A5SS= alternative 5'splice site, A3SS= alternative 3' splice site). **e,** Overlay from **e** and **d** after two (left) and six hours of treatment (right). Red: all genes that have a splicing change, grey: unchanged genes. Dashed line: hypothetical regression line. Solid line: actual regression line. Deep sequencing was done in cooperation with Rupert Öllinger, gene expression and splicing variants analysis with the help of Xueyang He and Prof. Dr. Paul Boutz.

4.4.3 Transcriptional program induced by LB-100-mediated PP2A inhibition

Since the previous results suggested a secondary role for splicing in the LB-100-mediated pathway and the CRISPR screens revealed a transcriptional misregulation , further effort was undertaken to discover the role of transcription. Transcription and splicing were shown to be functionally coupled. They can influence each other reciprocally and splicing occurs co-transcriptionally in most of the cases [219–221]. This results mainly due to the spliceosome assembly on the nascent mRNA on the C-terminal domain (CTD) of the RNA polymerase II and therefore are the spliceosome, the transcription machinery and the chromatin in close-proximity [221] (Fig. 18a). To uncover a transcriptional change, iRNAseq, a computational method to determine transcriptional regulation from the previous deep RNA-sequencing data, was utilized [222]. iRNAseq quantifies the transcriptional activity by assessing the intron coverage from total RNA sequencing data and thereby performing similar to common transcriptional activity techniques, like global-run-on sequencing (GRO-seq) or RNA Pol II ChIP-seq [222]. By doing so, an interesting difference in transcriptional activity after LB-100 treatment could be detected. A change of more than 1000 introns was already quantified in the mesenchymal cell line after two hours of treatment with LB-100, compared to the control. This increased even more after six hours (Fig. 18b, red). Also, the epithelial cell line showed a mild increase in intron coverage after inhibitor treatment, but overall, less than half of the mesenchymal cell line (Fig. 18b, blue). To gain insights into the transcription rate, the intron/exon ratio out of this dataset was calculated. In normal transcripts, the intron to exon ratio is usually around 1:1 [223], whereas this ratio already increased to more than 1.25 in the mesenchymal cell line after LB-100 treatment after two hours. An increase could also be detected in the epithelial cell line, but occurred here only in a 1.15 intron-exon ratio (Fig. 18c). Interestingly, on a basal level and without any treatment, mesenchymal and epithelial cell lines have overall a similar intron and exon quantification (Fig. 18d). All in all, this together points to a higher transcriptional output caused by inhibitor treatment in the mesenchymal cell line.
To finetune the promoter proximal pausing and elongation checkpoint of the transcriptional machinery by the RNA Polymerase II, the activity of the Integrator complex is also highly essential. The integrator complex consists of 14 subunits and furthermore is able to bind the protein phosphatase 2A with the INTS8 subunit. Together they are able to regulate transcription by dephosphorylating the CTD of the RNA Polymerase II [176,224]. Moreover, the Integrator not only helps to induce immediate early genes after a cell stimulus, but cleaves nascent RNA with the RNA endonuclease subunits (*INTS9*, *INTS11*, *INTS4*) on top of that [225,226]. Previously, the dataset of INTS8-knockout in HEK293T cells revealed reduced PP2A dephosphorylation activity with an increase in immediate early

gene expression and transcriptional pause release [176]. Indeed, a comparison of the LB-100 treated and the INTS8-knockdown dataset revealed a high PP2A and INTS8-controlled overlapping network, that induced immediate early genes like the AP1 transcription factors *Fos* and *Fosb*, *ATF3, Egr2* or *Dusp1* (Fig. 18e). The expression and intron coverage were already more prominent in the mesenchymal cell line after two hours when compared to the epithelial one (Fig. 18f-h). To further strengthen this finding, a dataset of integrator-dependent, EGF induced immediate early genes was compared with the iRNAseq dataset and analysed by a GSEA. Indeed, highly significant enrichment of IEG could be found in the mesenchymal and epithelial upregulated gene sets. In sum, all of the experiments point to a higher transcriptional output and induction of IEG after LB-100 treatment, which is more prominent in the sensitive, mesenchymal subtype.

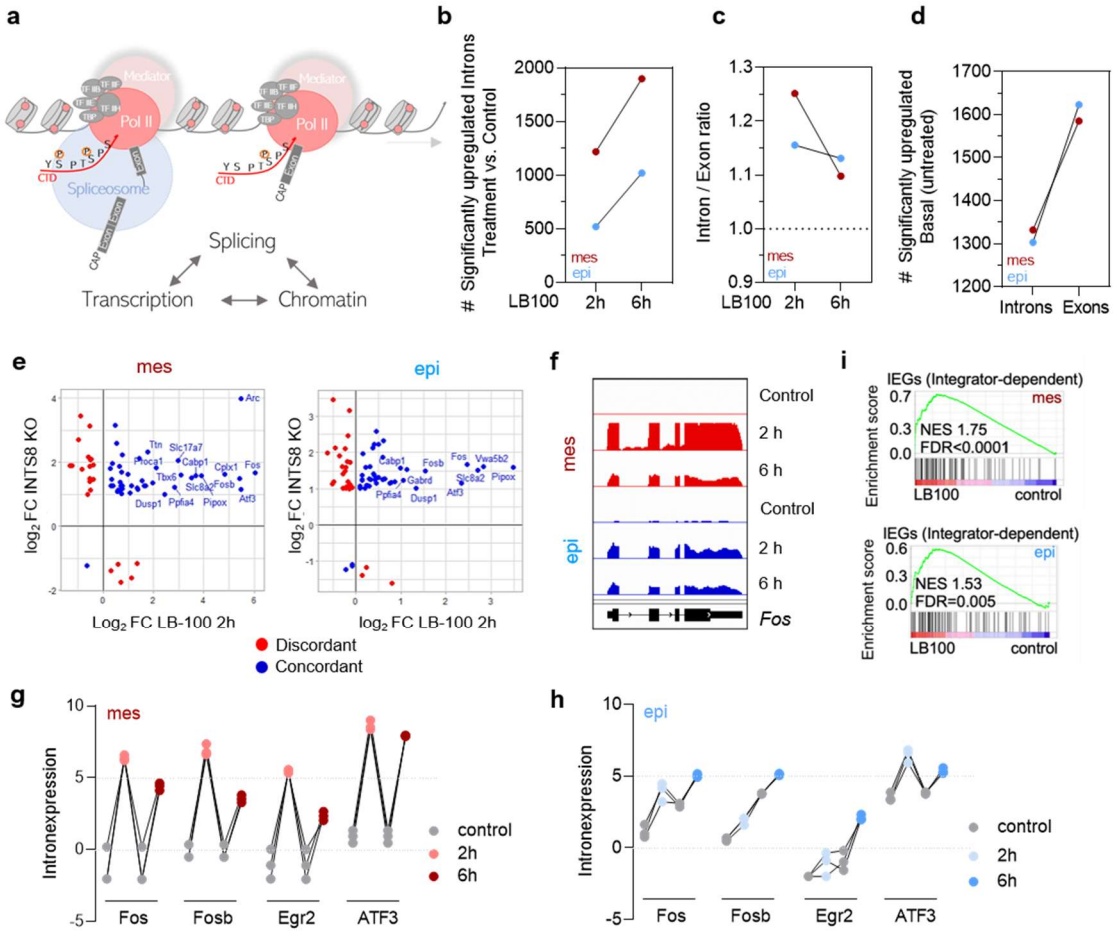

Figure 18 | LB-100 induces transcriptional program and activation of IEG

a, Schematic illustration of the RNA Polymerase II during the transcriptional process and the close proximity of the spliceosome, acting co-transcriptionally. Illustration according to [221,227]. **b,** iRNAseq analysis of the deep sequencing data revealed the significant upregulated introns after two and six hours of LB-100

treatment in the mesenchymal (red) and epithelial (blue) cell lines ($p < 0.05$, $log_2FC > 2$), compared to basal control coverage. **c,** Displayed are the ratio of upregulated introns and exons in mesenchymal and epithelial cell lines after two and six hours of treatment. **d,** Basal significantly upregulated introns and exons (untreated) between the mesenchymal (red) and epithelial cell line (blue). **e,** RNA deep sequencing data from **a** was compared with data after INTS8 knockdown [228]. Displayed are the discordantly (fiery red) and concordantly (cobalt blue) overlapping genes between the two datasets in mesenchymal (red) and epithelial (blue) cell lines. **f,** Illustration of changed IEG expression: IGV illustration of the change in *Fos* gene expression from control over two and six hours of LB-100 treatment in mesenchymal (red) and epithelial (blue). **g,** Pre-ranked GSEA analysis of the induced genes after two hours of treatment (log2FC) was done with a gene-set of IEGs , activated by an integrator dependent mechanism [229]. The normalised enrichment score (NES) and the false discovery rate (FDR) q are depicted. **h,** Intron expression in the mesenchymal cell line after two and six hours of treatment from divers IEGs from **d** are displayed. **i,** Same intron expression change in IEGs as in **g** from the epithelial cell line. iRNAseq analysis was done with the help of Anantharamanan Rajamani, INTS8 RNAseq comparison and IGV in cooperation with Xueyang He and IEG enrichment with the help of Prof. Dr. Günter Schneider.

4.4.4 Rescue of the transcriptional trigger by pharmacological CDK9 inhibition

Transcriptional regulation is a highly complex and tightly regulated cellular process, which involves many steps and assistant helper. As initial step, the pre-initiation complex (PIC) of the RNA Polymerase II is formed on the promoter starting sites. The PIC is composed of the TATA binding protein (TBP), general transcription factors (TFIIA,TFIIB, TFIID, TFIIE,TFIIF, TFIIH), the holoenzyme of the RNA polymerase II and the Mediator complex [230–232]. Shortly after initiation of the transcriptional process (after approximately 60-100 bp), the RNA Pol acquires a “paused” state at promoter-proximal regions stabilised by the DRB sensitivity inducing factor (DSIF, subunits SPT4 and SPT5) and the negative elongation factor (NELF-A, NELF-B, NELF-C, NELF-D) [233]. This mechanism controls and synchronises transcriptional events occurring in the cell [234]. To overcome the paused state into productive elongation, the activity of the positive transcription elongation factor b (P-TEFb) is needed. P-TEFb consists of a catalytic kinase (CDK9) and their regulatory subunit (Cyclin T1) and is part of three further larger complexes, namely the super elongation complex (SEC), a bromodomain-containing protein 4 (BRD4)-associated P-TEFb (BRD4–P-TEFb) and the 7SK small nuclear ribonucleoprotein (snRNP)-associated P-TEFb (7SK–P-TEFb) complex [235]. By phosphorylation of Ser2 of the RNAPII CTD and additional phosphorylation and dissociation of NELF and DSIF by the P-TEFb complex, the paused POL II is set free into productive elongation and gene transcription [228,236] . At the 3’ site of the coding regions, phosphatases are needed for RNAPol II dissociation and termination of the transcription process[237]. Due to the fact that, firstly, CDK9 plays the central role of the transcriptional elongation process detected

as hyperactivated after LB-100 treatment (Fig. 18b), and secondly, was one of the top scored genes in the CRISPR-drop out screen (Fig. 15&16), leads to further investigation into the CDK9-PP2A dependent process. For this, a highly specific CDK9 inhibitor (SB-1317, Fig. 19a&b), which showed the lowest half-maximal effective concentrations of all CDK9 inhibitors in a Kinobead assay (https://www.proteomicsdb.org/), was tested in epithelial and mesenchymal murine and human mesenchymal MIA PaCa-2 cell lines in combination with LB-100 treatment. Indeed, combinatorial treatment already rescued the morphological rounded phenotype, which is normally induced after six hours of LB-100 treatment (Fig. 19c). Interestingly, both the Ser2 hyperphosphorylation and the downstream effects of LB-100 (like ATF4 or ERK T202/204 activation), exclusively induced in the mesenchymal cell line, could be rescued by co-treatment with the CDK9 inhibitor (Fig. 19d&e). Since it was previously reported, that the protein phosphatase 1 is a negative regulator of the RNA Pol II elongation process and speed [238], further investigation into this process was undertaken. The inhibitory phosphorylation of the PP1 (Thr320) was indeed hyperactivated after LB-100 treatment and could again be restored after CDK9 inhibition (Fig. 19d). In addition to that, also the reduced cell viability of the mesenchymal cell lines after already six hours of LB-100 treatment could be rescued in a dose-dependent manner after co-treatment with SB-1317 (Fig. 19f). This could be further validated in the human MiaPaCa2-cell line, where the RNA Pol II Ser2 phosphorylation and the downstream induced integrated stress response were rescued after additional CDK9 inhibition (Fig. 19g). Since the co-treatment of LB100 and inhibition of CDK9 by SB-1317 reduced the morphological changes as well as the downstream effects detected after LB100 single treatment over all experiments, it can be assumed that the transcriptional elongation checkpoint is inactivated after LB100-mediated PP2A inhibition, favouring therefore a hyperactivated transcriptional machinery.

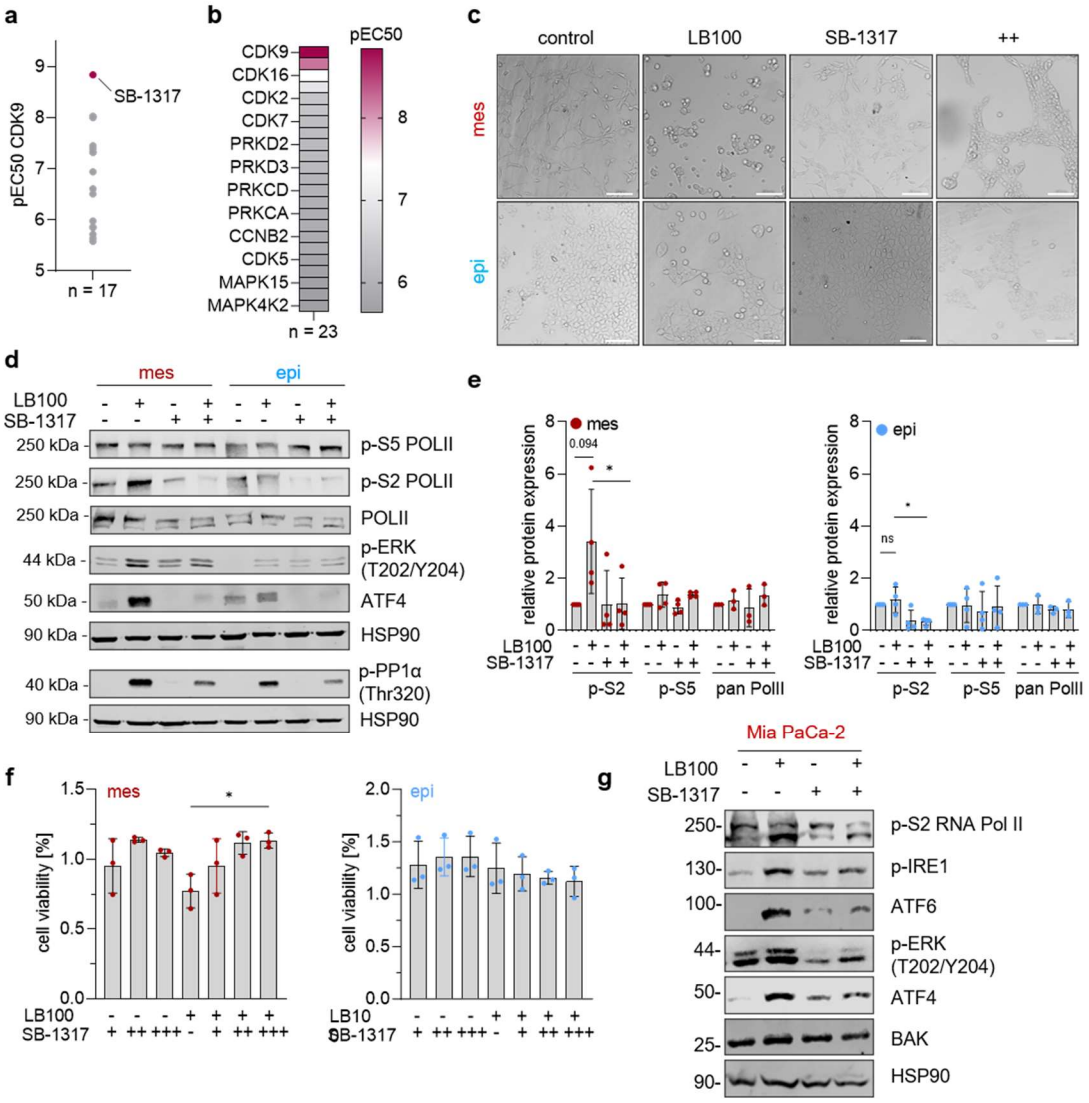

Figure 19 | Inhibition of CDK9 rescues LB-100 mode of action

a, CDK9 targeting inhibitors and their corresponding pEC50 values were analysed by a kinobead assay and retrieved from the proteomics. dB database. Highlighted is SB-1317, which has the highest affinity for targeting CDK9. **b,** All targets of the SB-1317 inhibitor and the corresponding pEC50 values. Data is retrieved from proteomics. dB. **c,** Representative brightfield images of an epithelial and mesenchymal cell line after six hours of treatment with LB-100 (20μM), SB-1317 (2 μM) or a combination of both. Scalebar = 100 μM. **d,** Western Blot analysis after six hours of LB-100 (20 μM), SB1317 (0.5 μM) or a combinatorial treatment in an epithelial (blue) and mesenchymal (red) cell line. Representative blots are shown (n ≥3). HSP90: loading control. **e,** Quantification of p-S2 RNA Pol II, p-S5 RNA-Pol II and total RNA Pol II from independent replicates (n≥3) from **d**. *(mes) = 0.0343, *(epi) = 0.045, two-tailed paired t-test. **f,** Cell viability was determined by CellTiter-Glo after six hours of treatment with LB-100 (25 μM) and increasing concentrations of SB-1317 (+ = 1 μM, ++ = 2 μM, +++ = 4 μM) in mesenchymal (red, left) and epithelial (blue, right) murine cell lines. * = 0.0232, two-tailed paired t-test. **g,** Western Blot analysis of MIA PaCa-2 cell line after six hours of treatment with LB-100 (10 μM), SB-1317 (2 μM) or a combination of both. HSP90: loading control. One representative blot out of three experiments is shown.

To strengthen that observation, another CDK9 inhibitor (P-276-00) was tested. Compared to SB-1317 before, P-276-00 has a reduced half-maximal concentration targeting CDK9 (Fig. 20a, determined via Kinobead assay, https://www.proteomicsdb.org/), but overall is predicted to have less off-targets (Fig. 20b). Cell viability, determined by CellTiter-Glo after co-treatment of LB-100 and P-276-00, partially rescued the single-treatment effect and reduced cell viability of LB-100 after six hours in the mesenchymal cell line. However, not significantly (Fig. 20c). On protein level, upregulated ISR components, autophagy and stress speckles marker and hyperphosphorylation of the Ser2 RNA Pol II in the mesenchymal cell line due to LB-100 single treatment could again be rescued with the co-treatment of the CDK9 inhibitor P-276-00 for six hours (Fig. 20d). This, again, promotes the hypothesis of CDK9 dependent translational elongation after LB-100 treatment.

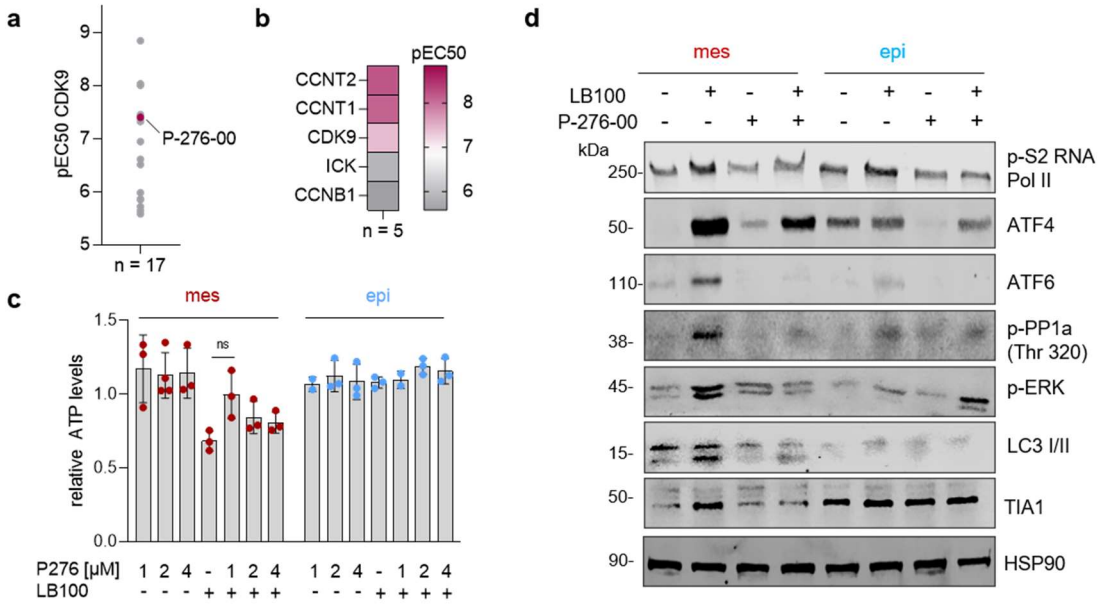

Figure 20 | Second CDK9 inhibitor confirms LB-100 rescue

a, CDK9 inhibitors and their responding pEC50 values. Highlighted is the inhibitor P-276-00. **b,** Targets of the inhibitor P-276-00 and their corresponding pEC50 are color-coded (n = 5). **c,** Cell viability was determined by CellTiter-Glo after six hours of LB-100 treatment (25 µM) with increasing indicated concentrations of P-276-00 in an epithelial (blue) and mesenchymal (red) murine cell line. **d,** Western Blot analysis of an epithelial (blue) and mesenchymal (red) cell line after treatment with LB-100 (20 µM, P-276-00 (2 µM) or a combination of both after six hours). HSP90: loading control. One representative blot out of three experiments is shown.

5 Discussion

Pancreatic ductal adenocarcinoma is still hardly treatable and personalised treatment options are of a high need for better patient outcomes in the future. Thereby, intra-tumour heterogeneity represents the greatest challenge to deal with [239]. With this thesis evidence is provided that the protein phosphatase 2A is a valuable target in the future treatment options for pancreatic cancer. The treatment of PDAC model systems, including patient derived pancreatic cancer organoids with the inhibitor of the protein phosphatase 2A, namely LB-100, revealed a subtype specific response. The aggressive, mesenchymal subtype responded overarching in a low micromolar range within only few hours of treatment with LB-100 compared to less response detected in the well differentiated epithelial subtype. This is supported not only by marker gene expression in the model systems and pathway analysis but also confirmed by the differential response of the mesenchymal and epithelial component of an isogenic cell line. Despite that, further PP2A inhibition by Phendione [198] verified not only the subtype specificness of LB-100, but further affirmed a specific PP2A-driven process. The short elimination half-life and effectiveness of LB-100 could also already be demonstrated in the first human clinical trial, whereby a low drug clearance, a low distribution volume and additionally a short half-life of the drug (1-2 hours) was observed [137]. This is well reflected in this study, where the effective period occurred already after four till six hours of treatment in all model systems. Despite the high GI_{50} LB-100 concentrations determined in the model systems, low micromolar single-digit inhibitor responsiveness in the PDAC organoids point to usable concentrations in further patient stratifications, since patient derived organoids can best mimic the patients tumour heterogeneity and therefore predict a possible successful treatment option early on [240–243]. The one PDAC-patient included in the first human clinical trial of LB-100 showed a significant partial response at one of the lowest used drug concentrations (0.83 mg/m^2) [137], thereby demonstrating the *in vivo* efficiency of LB-100 in PDAC patient treatment.

Regardless of the clinical efficiency and subtype specific patient relevance, further deep mechanistic understanding is beneficial for continuing applications, synergistical rational drug combinations and increasing success of the drug in the future [200,244]. Investigation into the mode of action of LB-100 by a CRISPR drop-out screen revealed a transcriptional and splicing based mechanism. Deep sequencing analysis of splicing patterns indeed confirmed massive splicing changes, selectively in the mesenchymal subtype. The

most affected category of the splicing changes was found in skipped exons, although the overlay of high turnover genes and splicing changes did not claim for splicing as the primary induced process. It is well known, that splicing occurs in close proximity to the RNA Polymerase II and mostly co-transcriptionally [220]. Therefore, the splicing process and the splice site availability is highly dependent on the RNA Pol II elongation rate [245]. Believing the “window of opportunity” model, fast elongation rates prime the splicing machinery for favouring exon skipping [246,247], as indeed observed in our experiments. Using iRNAseq, described as a comparable technique to CHiP, Gro or Pro-Seq to access the transcriptional activity [222], the discovery of higher transcriptional output in the mesenchymal cell lines after LB-100 treatment was actually made and supports the theory of faster elongation rates. Moreover, this finding was treatment-specific and not due to higher basal transcriptional profiles between mesenchymal and epithelial cell lines. Interestingly, the highest transcriptional output was detected in the first treatment hours and became less over time, reflecting thereby again the before described effective spectra of LB-100 detected in the clinical trial [137].

One of the first rapid induced and changed genes after a stimulus are immediate early genes (IEG). These genes are known to have short primary transcripts, high affinity TATA-boxes as well as enriched and stalled RNA Polymerase II directly downstream at the transcription start sites and are therefore the primary expressed genes without the need of protein synthesis [248,249249]. Most of the IEG consist of transcription factors, like *FOS*, *JUN*, *EGR-1 & EGR-2* or *ATF3* [250].

Previously, a coherence of the knockout of the Integrator subunit 8 and the expression of IEG was made [176]. The Integrator is a complex of minimum 14 subunits and has a described dual specificity of endonuclease and phosphatase activities [251]. INTS11 and INTS9 is known to have endonuclease activity for cleavage of non-coding small nuclear RNAs (snRNA) and transcription termination. Depletion of INTS9 or INTS 11 was shown to stimulate transcription elongation [252–254]. Further on, a noncanonical PP2A, which lacks the regulatory B subunits, forms the INTAC complex (phosphate module of the integrator) together with the subunits INTS8 and INTS6 to dephosphorylate the RNA Pol II and regulate promoter proximal pausing [255,256]. Additionally, disruption of INTS8 by a novel dTAG-13 system led to Pol II hyperphosphorylation, pause release of the RNA Pol II and additional transcriptional activation [256]. A correlation of our LB-100 treated gene expression profile with a previously published INTS8 depleted dataset indeed revealed a large-scale overlap of concordantly expressed genes between the two datasets. After already two hours of LB-100, massive induction of immediate early genes, regulated also after INTS8 disruption, were found. Interestingly, these transcriptions factors were up-regulated in both cell lines, whereby the mesenchymal one showed more than double

the change in expression. This assumes that inhibition of the phosphatase by LB-100 could block the phosphatase module of the INTAC complex and thereby promoting transcriptional elongation by pause release and IEG expression.

Accessory, the knockout of the Pol II associated factor *PAF1* was found to be synthetic lethal with LB-100 or Phendione treatment in all the CRISPR drop out screen. In addition to the previously described elongation stimulation after INTS9 disruption, PAF1 is also known as regulator of the promoter-proximal pausing event and disruption of it urges on the release of paused Pol II into productive elongation [257]. Recently, a coherency and direct interaction of the PP2A-INTAC complex with PAF1 was discovered, which serves as explanation for a reduced phosphatase activity after PAF1 loss and promoter-proximal pause release [258]. Therefore, it is conclusive, that inhibition of the phosphatase by LB-100 and CRISPR-knockout of PAF1 shows synergistic lethal effects. So far, there is no available drug targeting PAF1, but combinatorial treatment could improve patients' treatment options. Moreover, PAF1 involvement in the ADM and pancreatic cancer progression could already be demonstrated, which supports the clinical relevance [259].

The major driver of transcriptional productive elongation is the P-TEFb elongation complex, comprised of CDK9 and Cyclin T1, by phosphorylating the Ser2 of YSPTSPS repeat of the RNA Pol II CTD [260]. Whereas phosphorylation of Ser2 is associated with higher elongation rates, phosphorylation on Ser5 is related with paused Pol II and peaks around the transcription start site [257,261]. CDK9 moreover phosphorylates NELF and DSIF, leading to dissociation of the complex and productive elongation [262]. In line with higher transcriptional rates detected via iRNAseq, hyperphosphorylation of the CTD Ser2 repeat was indeed detected after LB-100 treatment selectively in the mesenchymal subtype. Furthermore, CDK9 was one of the 37 overlapping genes and its knockout favoured resistance to LB-100 in the three independent CRISPR dropout screens.

Clinical and therapeutical relevance of the CDK9-PP2A-Integrator complex was already additionally verified for leukemic and solid tumour models. Here, PP2A activation in combination with CDK9 inhibition showed enhanced paused Pol II, leading to cell death by high synergistical cooperation [263]. The finetuning of transcription is therefore known to be achieved between a balance of the kinase CDK9 and the phosphatase PP2A interplay.

Endogenously, the protein SET normally regulates the PP2A activity [264]. In a recent study, the balance of PP2A and CDK9 is also described for PDAC, while the protein SET was identified as the main factor for hyper-transcribed growth-essential genes by endogenously blocking PP2A activity [265].

CDK9 is further described to catalyse the inhibitory phosphorylation site of the phosphatase 1 (PP1) during productive elongation, normally involved in transcription termination

[266]. Indeed, the inhibitory phosphorylation of PP1 could be demonstrated after LB-100 treatment, reinforcing again the argument of activated elongation and show once more, how kinase and phosphatase interplay regulate the transcriptional process.

Next to the insight into the mechanistical triggering of LB-100, research in the downstream regulated pathways and effects took place. Errors of the protein synthesis can occur in different stages of the process, including transcriptional or splicing errors, translational misincorporation or also afterwards by protein misfolding or post-translational modifications [267]. The detected shift in mRNA abundance due to transcriptional elongation and additional massive splicing changes after LB-100 treatment suggests an error prone protein synthesis afterwards. Misfolded or error prone proteins are normally accumulating in the ER, leading to activation of the unfolded protein response to restore the ER protein homeostasis. The three main encompassing pathways of the UPR are activated by IRE1α, ATF6 or PERK signalling [268]. Autophagy as further mechanism supports thereby the UPR to recycle or degrade the misfolded components [269]. Protein analysis indeed confirmed an induced UPR from ER stress and autophagy selectively in the mesenchymal human and murine cell lines after LB-100 treatment. Additional, stress speckles as compartments of stalled mRNAs during stressed states [270] were accumulating over the treatment time in the mesenchymal cell lines. However, the epithelial subtype showed higher occurrence of stress speckles even at basal level, which didn't change over the respective treatment duration.

Prolonged ER stress could further have two main effects. On the one hand, it can induce the integrated stress response via the activation of p-eIF2α and ATF4 to restore the cellular homeostasis as an adaptive mechanism. On the other hand, in an inevitable situation or in severe stress conditions, it can also induce cell death via apoptosis in the end [271]. Both regulations were found, in fact, in the mesenchymal cell lines after prolonged treatment with the phosphatase inhibitor despite the additional activation of autophagy and stress speckles. These two findings prove the existence of erroneous translation, confirm a sustained disturbed cellular homeostasis and apoptosis as killing mechanism after LB-100 treatment for the mesenchymal subtype of pancreatic cancer. Interestingly, targeting PDAC by inducing prolonged and severe ER stress and the unfolded protein response is an emerging treatment option for prospective and already used chemotherapies in the clinic [272]. However, EMT may explain why mesenchymal cells are more susceptible to severe ER stress triggered responses, since EMT itself starts under stressed situations, as observed in colon cancer [273]. Blocking of the UPR in PDAC models resulted

moreover in less aggressive subpopulations of mesenchymal origin, arguing for a treatment option especially for pugnacious mesenchymal PDAC cancers [274].

That the two detected phenotypes of pause released RNA Pol II and disturbance of the homeostatic balance after LB-100 treatment are not independently induced events, could be clearly demonstrated with the inhibition of CDK9 by two different drugs. By inhibition of CDK9, all previously triggered downstream effects and morphological changes by LB-100 could be restored and normalised. Based on existing literature, until today there is no described connection of CDK9 and induction of ER stress, and the connection of transcriptional output to the capacity of cellular homeostatic systems is a novel concept. Knockout of CDK9 led to a survival advantage in our CRISPR genetic drop out screen and was further verified with restored cell viability in the simultaneous treatment, underscoring the transcriptional trigger as main mechanistical event. Whether other processes are involved cannot be completely ruled out and needs further research.

Although the phenotypic response of the mesenchymal subtype cannot be clearly assigned to this day, EMT is known to be induced by activation of several transcription factor networks and therefore possibly priming mesenchymal cells to a disturbance of a transcriptional mechanism [275]. Additionally, MYC expression was shown to correlate with enhanced pause release of the RNA Pol II by increasing the output of the transcriptional expression pattern, acting therefore as a universal transcriptional amplifier [276,277]. This is mainly described for the aggressive adenosquamos/basal-like PDAC and is associated with *myc* amplification [278,279]. In contrast to only MYC-driven transcriptional hyperactivation, most of the hypertranscription in primary cancers are a result of transcriptional suppression loss or increased glycolytic flux [280] . If these factors influence LB-100 susceptibility awaits experimental validation, however, a glycolytic subtype strongly overlaps with the mesenchymal /basal-like one [46]. Further on, an old study from 2009 already showed a different regulated gene program of the IEG in well differentiated fibroblasts and embryonic stem cell, mainly forced by the mediator complex knockout, leading to a paused RNA Pol II at the promoter proximal site exclusively in the ES [281].

6 Summary, Limitations and Outlook

Overall, by elucidating this unconventional treatment option, this thesis indicates that phosphatase inhibitors indeed represent a possible treatment option for a subtype of PDAC cancers. Further, this deep knowledge of the LB-100 induced cellular reaction could provide information for future biomarker development and synergistical rational combination therapies. Summed up, it is clearly demonstrated that a subtype specification has to be prerequisite in the future for specialized cancer treatment and will hopefully lead to purposeful treatment and therefore increased chance of survival for the patient.

However, the major limitation of this study is that LB-100 is only effective for a short period of time and therefore the described mechanism of action can only be detected and rescued during this period. For future applications it would be interesting to additional apply a sequential treatment for three consecutive days, similar to that used in the clinical trial and investigate, whether further treatable adaption and resistance pathways arise. Further, CDK9 and PP2A are highly essential genes and a genetic validation of the purposed mechanism turned out to be very difficult. To solve this problem, selectively inducible knockout models could be on the one hand a tool to mimic the LB-100 effect genetically and on the other side decipher the mode of action and the intricate relationship of CDK9 and PP2A more clearly. A tetracycline-regulated RNAi model is at the moment under development and awaits experimental confirmation.
Since glycolysis was recently described as the main factor for driving hypertranscription and overlapping with a human mesenchymal / basal-like subtype as discussed above, deeper investigation into altered glycolytic activity may give further crucial insights in the subtype sensitivity to LB-100.
Finally, fastGro- or Pro-seq of nascent RNA could additionally yield a much deeper understanding into the transcriptional rate and the described RNA-Pol II elongation turnover at nucleotide resolution.

7 Publications

Murr, J., Schneider, C. …., Wirth, M., Krämer, O., Schneider, G. (2024) Activating transcriptional elongation as a strategy to treat aggressive mesenchymal pancreatic cancer *In Revision for Cancer Research*

Nguyen, A., Leydecker, A., Mustafa, A., **Murr, J.**, Butter, F., Krämer, O. (2024) The protein phosphatse-2A subunit PR130 is involved in the formation of cytotoxic protein aggregates in pancreatic ductal adenocarcinoma cells.
In Revision for Cell Communication and Signaling

Orben, F., Lankes, K., Schneeweis, C., …**Murr, J.,** ...Reichert, M., Saur, D., Schneider G. (2022) Epigenetic Drug Screening Defines a PRMT5 Inhibitor Sensitive Pancreatic Cancer Subtype. **JCI Insight.** 7(10): e151353

Nguyen, A., Dzulko, M., **Murr, J**., Yen, Y., Schneider,G., Krämer, O. (2021) Class 1 Histone Deacetylases and Ataxia-Telangiectasia Mutated Kinase Control the Survival of Murine Pancreatic Cancer Cells upon dNTP Depletion. **Cells**. *10*(10), 2520

8 Appendix

8.1 Supplemental figures

Fig. S9g: Western Blots of PDCL

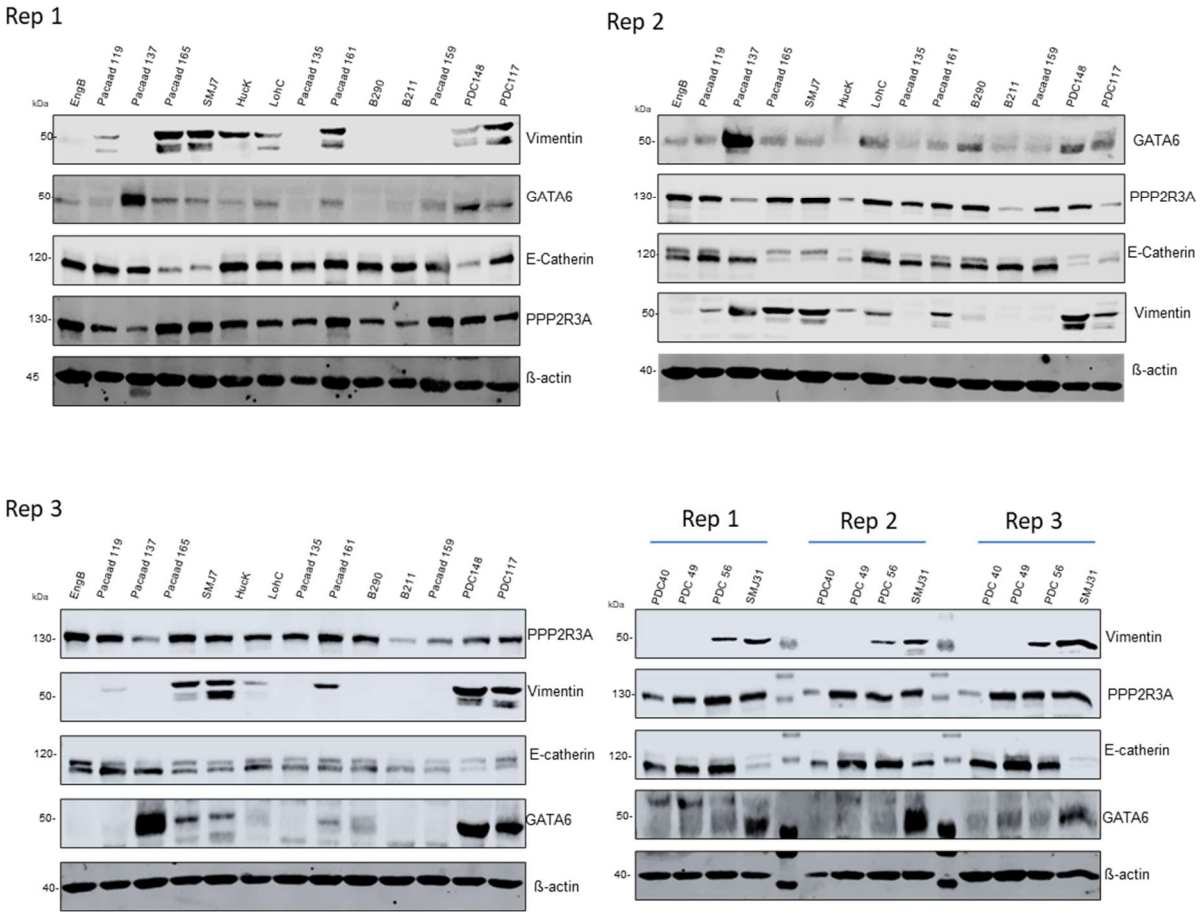

8.2 Uncropped Western Blots

7.2.1 Blots to Fig. 11d – Apoptosis in MIA PaCa2 after LB-100 treatment

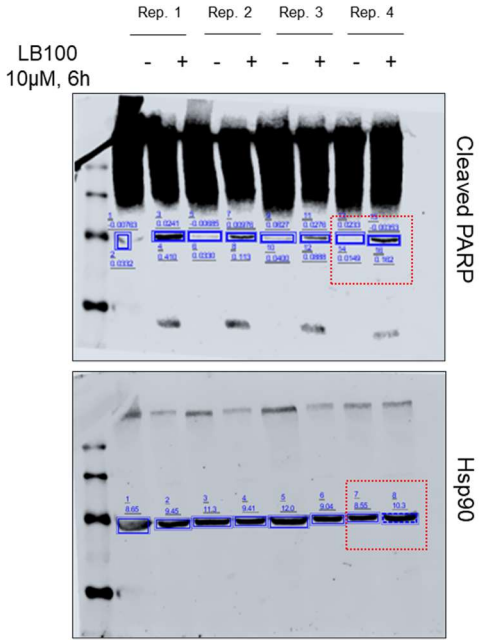

7.2.2 Blots to Fig. 12c – TIA-1 expression in mesenchymal and epithelial cells

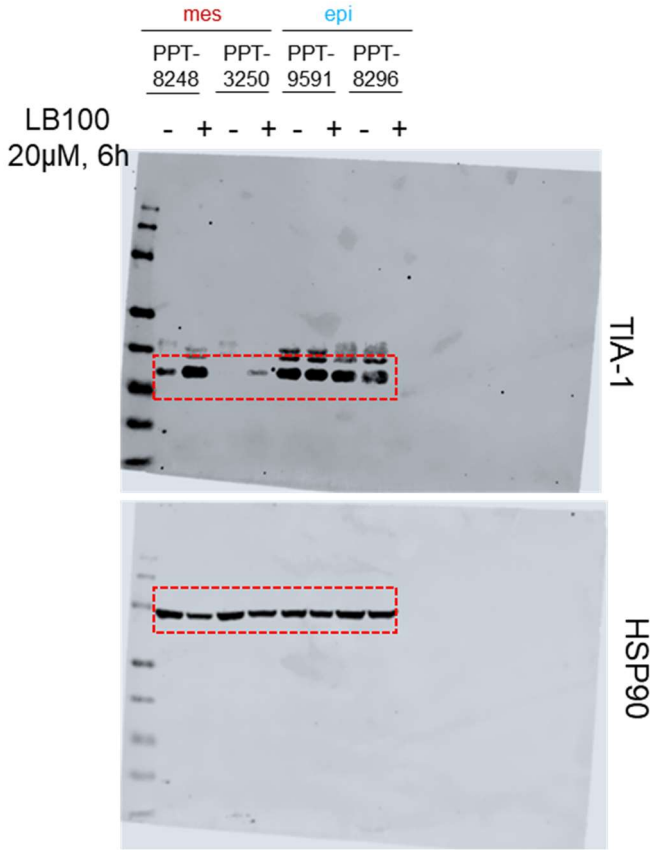

7.2.3 Blots to Fig. 12d – Integrated stress response

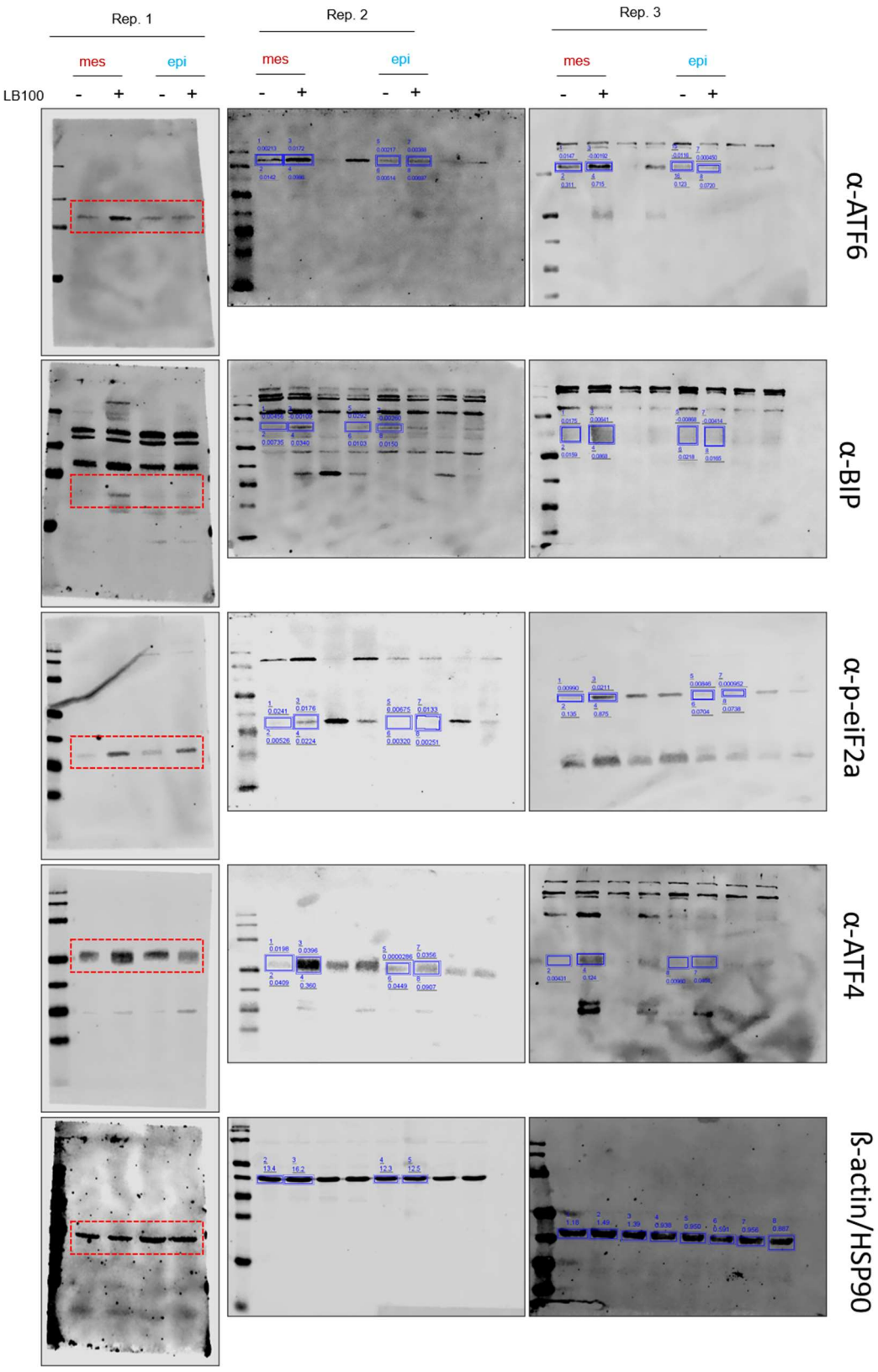

7.2.4 Blots to Fig. 12f – ISR in human cells

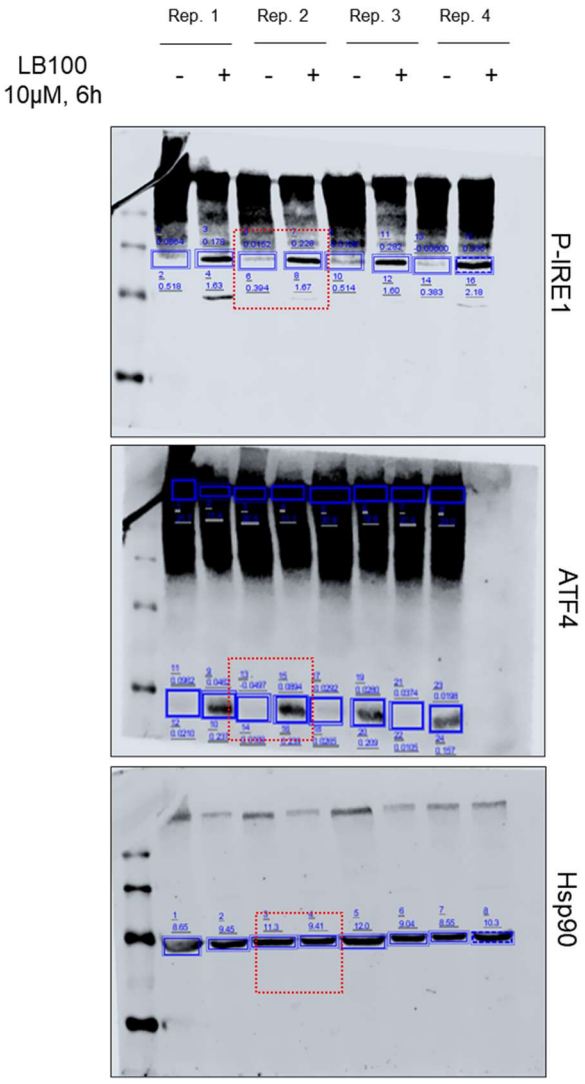

7.2.5 Blots to Fig. 13c - BAK expression

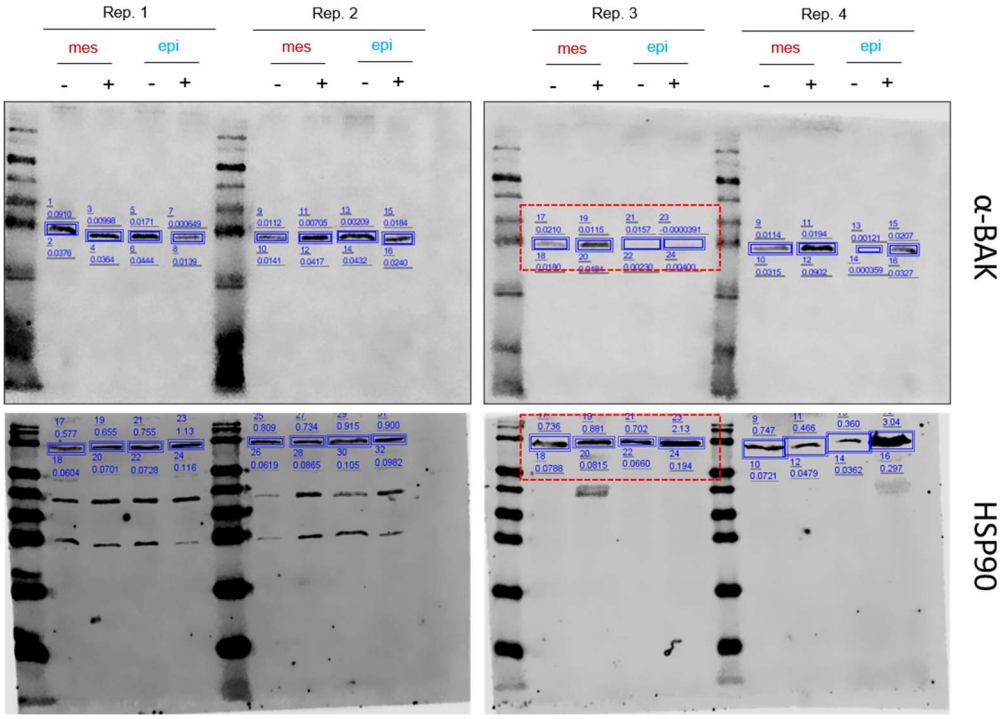

7.2.6 Blots to Fig. 13d – BAK expression in human cells

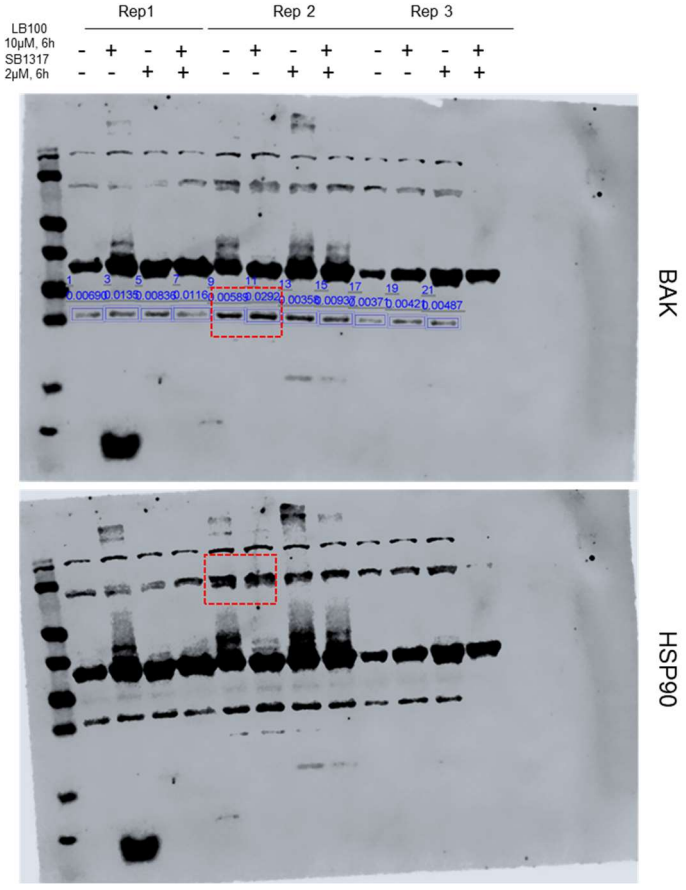

7.2.7 Blots to Fig. 14a & 14c - LB-100 induced pathways murine

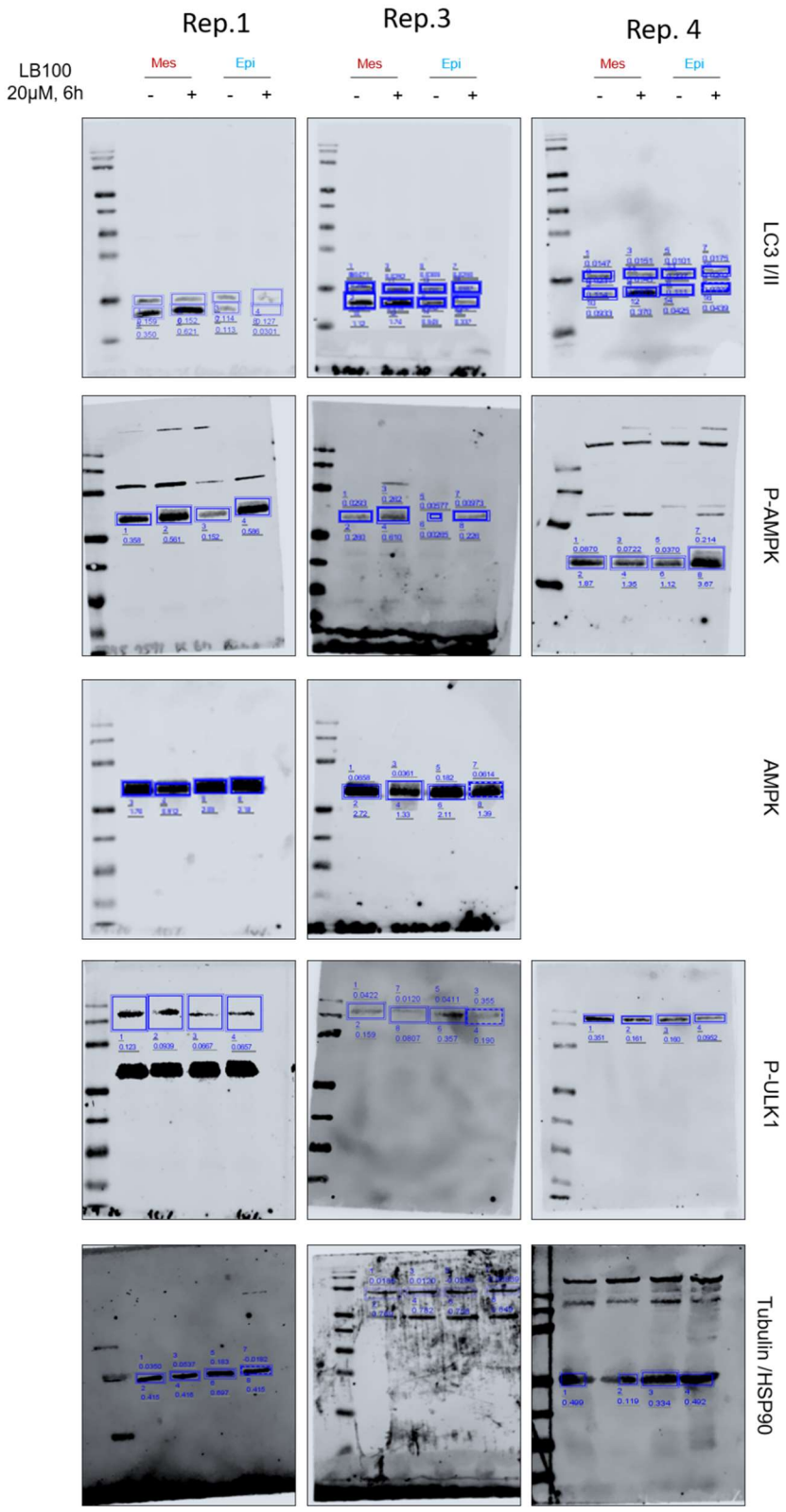

7.2.8 Blot to Fig. 14e - LB-100 induced pathways MIA PaCa-2

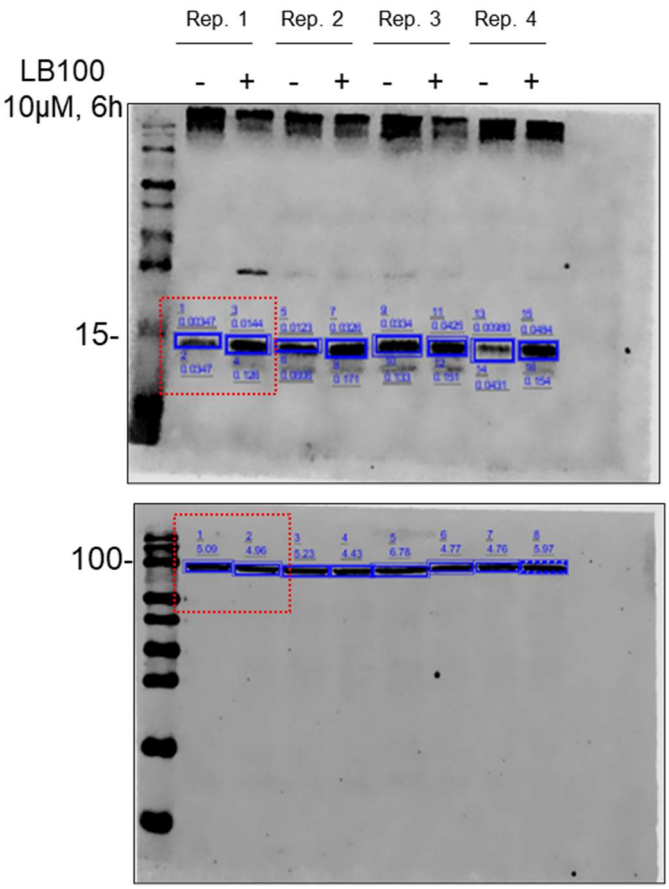

7.2.9 Blot to Fig. 16a - Cas9 expressing PPT-9091 cell lines

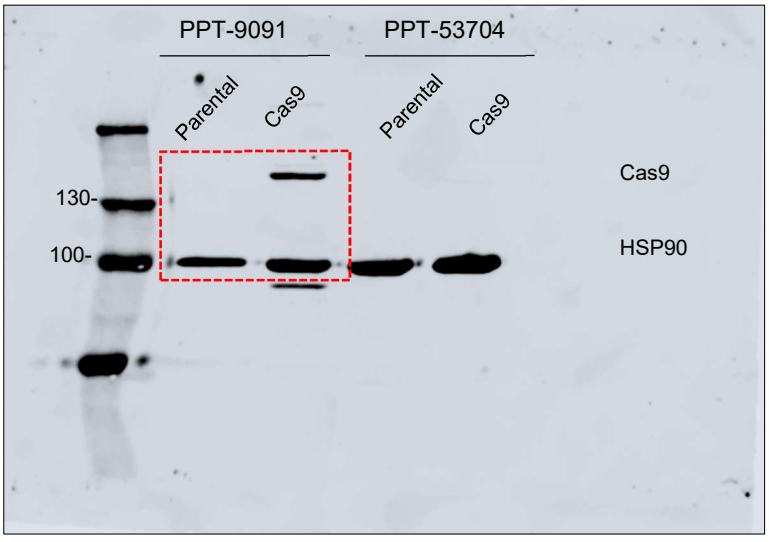

7.2.10 Blots to Fig. 19d – Transcriptional characterisation

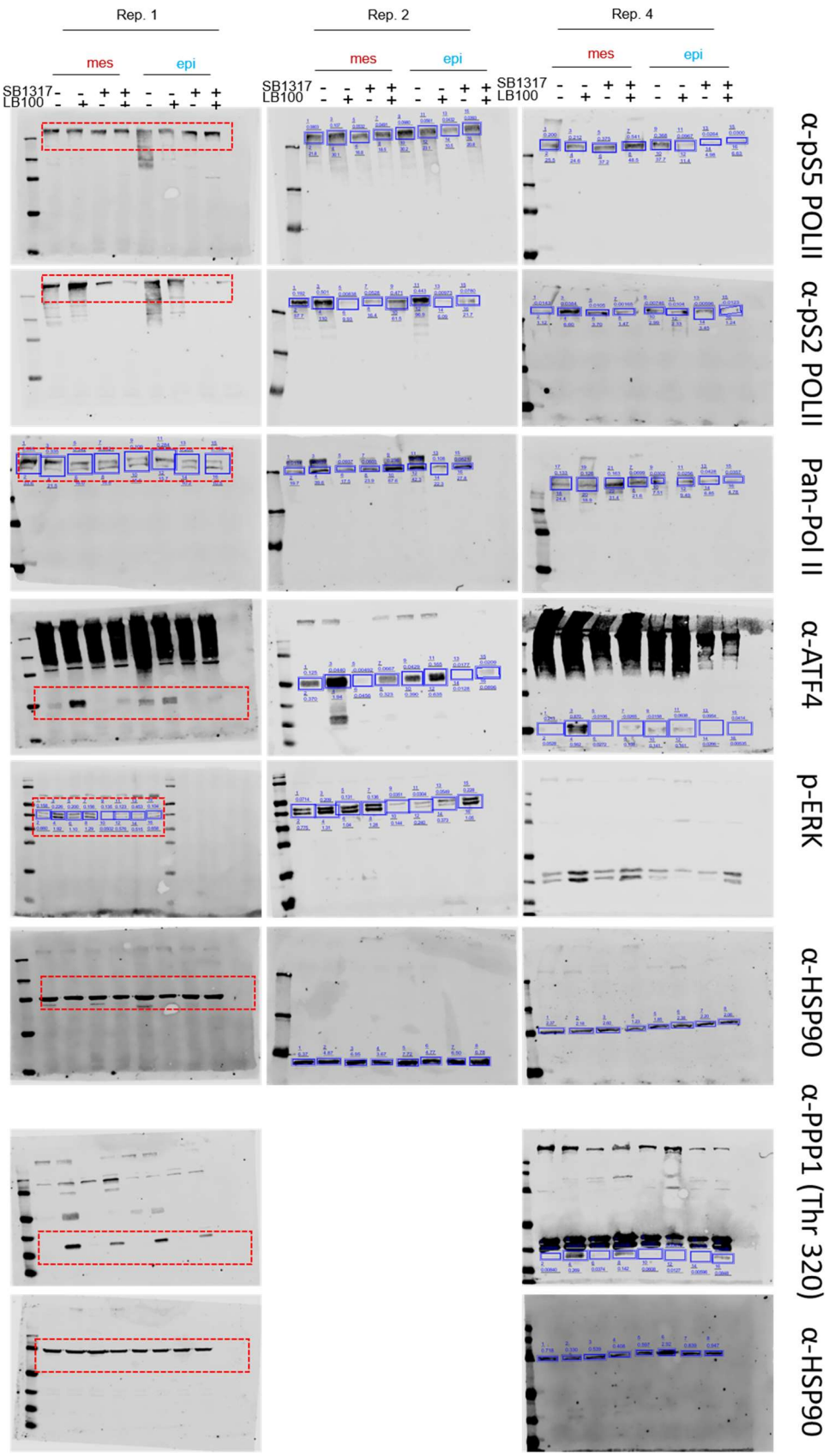

7.2.11 Blots to Fig. 19g – CDK9 inhibition by SB-1317

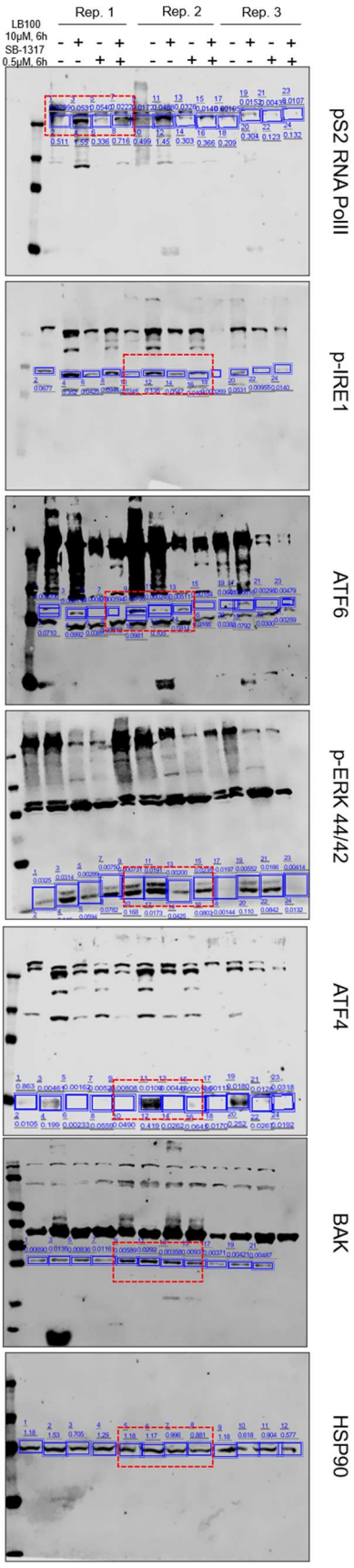

7.2.12 Blots to Fig. 20d – CDK9 inhibition by P-276-00

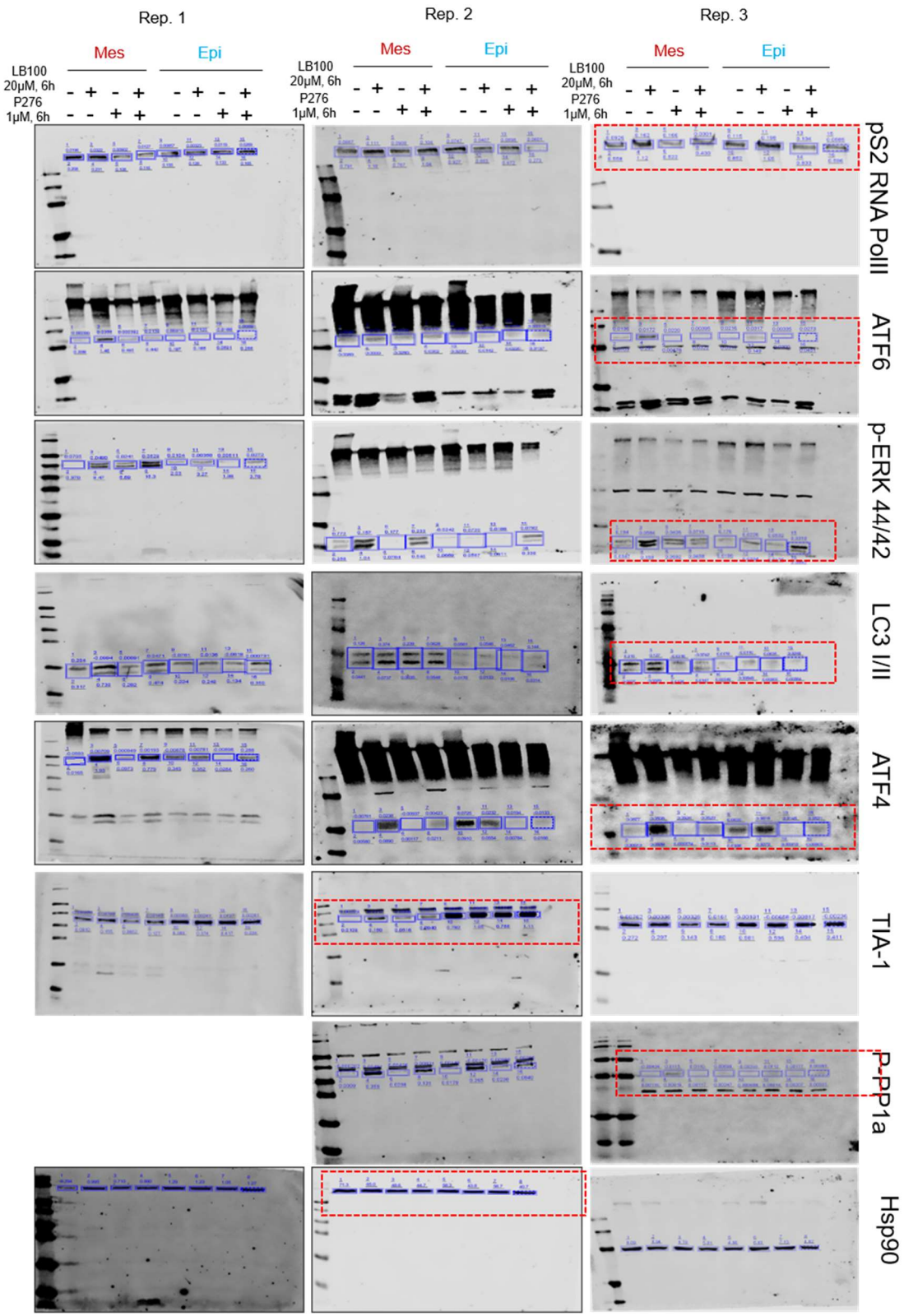

8.3 Target priority scores Project score

Original data from Fig. 6A

tractability b	gene id	score	symbol	analysis id	analysis name	Group
1	SIDG04147	52	CDK4	13	Pancreatic Carcinoma	Approved or in clinical dev
1	SIDG39916	49.5555556	TUBB4B	13	Pancreatic Carcinoma	Approved or in clinical dev
1	SIDG40031	46.6	TYMS	13	Pancreatic Carcinoma	Approved or in clinical dev
1	SIDG21627	42.8	NDUFB10	13	Pancreatic Carcinoma	Approved or in clinical dev
1	SIDG07457	42	EGFR	13	Pancreatic Carcinoma	Approved or in clinical dev
2	SIDG02179	50.8	BCL2L1	13	Pancreatic Carcinoma	Approved or in clinical dev
2	SIDG01979	47.0666667	AURKA	13	Pancreatic Carcinoma	Approved or in clinical dev
2	SIDG20992	43.3333333	MTOR	13	Pancreatic Carcinoma	Approved or in clinical dev
2	SIDG12412	41	IGF1R	13	Pancreatic Carcinoma	Approved or in clinical dev
4	SIDG07618	61.5384615	EIF4G1	13	Pancreatic Carcinoma	Supporting evidence
4	SIDG05669	57.3333333	CTNNB1	13	Pancreatic Carcinoma	Supporting evidence
4	SIDG25579	55	PPP2CA	13	Pancreatic Carcinoma	Supporting evidence
4	SIDG04102	52.6666667	CDH1	13	Pancreatic Carcinoma	Supporting evidence
4	SIDG37562	52.3076923	TFRC	13	Pancreatic Carcinoma	Supporting evidence
4	SIDG27184	50.8	RHOA	13	Pancreatic Carcinoma	Supporting evidence
4	SIDG04044	48	CDC25B	13	Pancreatic Carcinoma	Supporting evidence
4	SIDG34537	48	SLC2A1	13	Pancreatic Carcinoma	Supporting evidence
4	SIDG02150	48	BCAP31	13	Pancreatic Carcinoma	Supporting evidence
4	SIDG40091	48	UBC	13	Pancreatic Carcinoma	Supporting evidence
4	SIDG26502	46.6	RAB10	13	Pancreatic Carcinoma	Supporting evidence
4	SIDG04472	46	CFL1	13	Pancreatic Carcinoma	Supporting evidence
4	SIDG01801	45.8461539	ATP5F1A	13	Pancreatic Carcinoma	Supporting evidence
4	SIDG03339	45.6666667	CAD	13	Pancreatic Carcinoma	Supporting evidence
4	SIDG01327	44.5	ARF1	13	Pancreatic Carcinoma	Supporting evidence
4	SIDG03828	44.5	CCNB1	13	Pancreatic Carcinoma	Supporting evidence
4	SIDG26287	44.2666667	PTPN11	13	Pancreatic Carcinoma	Supporting evidence
4	SIDG10635	44.1818182	GRB2	13	Pancreatic Carcinoma	Supporting evidence
4	SIDG00429	43.8	ADAR	13	Pancreatic Carcinoma	Supporting evidence
4	SIDG17607	43.3333333	METAP2	13	Pancreatic Carcinoma	Supporting evidence
4	SIDG41294	43.3333333	YAP1	13	Pancreatic Carcinoma	Supporting evidence
4	SIDG29079	43.3333333	RNF4	13	Pancreatic Carcinoma	Supporting evidence
4	SIDG08839	42.4	FBL	13	Pancreatic Carcinoma	Supporting evidence
4	SIDG10267	41.1666667	GMNN	13	Pancreatic Carcinoma	Supporting evidence
4	SIDG05009	41	CNOT1	13	Pancreatic Carcinoma	Supporting evidence
4	SIDG07619	40	EIF4G2	13	Pancreatic Carcinoma	Supporting evidence
5	SIDG04595	55.6363636	CHMP4B	13	Pancreatic Carcinoma	Supporting evidence
5	SIDG40096	52.6666667	UBE2C	13	Pancreatic Carcinoma	Supporting evidence
5	SIDG01188	51.8181818	AP2M1	13	Pancreatic Carcinoma	Supporting evidence
5	SIDG12098	51.5	HSPD1	13	Pancreatic Carcinoma	Supporting evidence
5	SIDG01809	50.3333333	ATP5F1B	13	Pancreatic Carcinoma	Supporting evidence
5	SIDG00262	49.1666667	ACTB	13	Pancreatic Carcinoma	Supporting evidence
5	SIDG10611	48	GPX4	13	Pancreatic Carcinoma	Supporting evidence
5	SIDG13318	46.6	ITGB5	13	Pancreatic Carcinoma	Supporting evidence
5	SIDG00321	44.5	ACTR1A	13	Pancreatic Carcinoma	Supporting evidence
5	SIDG01811	44	ATP5F1C	13	Pancreatic Carcinoma	Supporting evidence
5	SIDG07307	43.3333333	EDF1	13	Pancreatic Carcinoma	Supporting evidence
5	SIDG40132	42.8235294	UBE2L3	13	Pancreatic Carcinoma	Supporting evidence
5	SIDG37258	42.4	TBCA	13	Pancreatic Carcinoma	Supporting evidence
5	SIDG04945	42.1666667	CMPK1	13	Pancreatic Carcinoma	Supporting evidence
5	SIDG34615	42	SLC7A5	13	Pancreatic Carcinoma	Supporting evidence
5	SIDG01855	42	ATP5PB	13	Pancreatic Carcinoma	Supporting evidence
5	SIDG12201	41.6363636	HUWE1	13	Pancreatic Carcinoma	Supporting evidence
5	SIDG25150	41.4117647	PNN	13	Pancreatic Carcinoma	Supporting evidence
5	SIDG07625	41	EIF5A	13	Pancreatic Carcinoma	Supporting evidence
5	SIDG21127	41	MYH9	13	Pancreatic Carcinoma	Supporting evidence
5	SIDG06194	41	DDX3X	13	Pancreatic Carcinoma	Supporting evidence
5	SIDG40227	41	UBR4	13	Pancreatic Carcinoma	Supporting evidence
5	SIDG06197	40.3636364	DDX5	13	Pancreatic Carcinoma	Supporting evidence
6	SIDG37265	44.5	TBCD	13	Pancreatic Carcinoma	Supporting evidence
6	SIDG25256	41	POLRMT	13	Pancreatic Carcinoma	Supporting evidence

8	SIDG09267	53.25	FOSL1	13	Pancreatic Carcinoma	Weak or no supporting evi
8	SIDG16779	48	LRR1	13	Pancreatic Carcinoma	Weak or no supporting evi
8	SIDG22473	42	NUP153	13	Pancreatic Carcinoma	Weak or no supporting evi
9	SIDG13821	56.4	KLF5	13	Pancreatic Carcinoma	Weak or no supporting evi
9	SIDG24385	51.5	PFDN5	13	Pancreatic Carcinoma	Weak or no supporting evi
9	SIDG12265	51.3333333	ID1	13	Pancreatic Carcinoma	Weak or no supporting evi
9	SIDG07935	51.2	ERCC2	13	Pancreatic Carcinoma	Weak or no supporting evi
9	SIDG36414	48	SREBF1	13	Pancreatic Carcinoma	Weak or no supporting evi
9	SIDG08993	48	FDXR	13	Pancreatic Carcinoma	Weak or no supporting evi
9	SIDG37262	48	TBCB	13	Pancreatic Carcinoma	Weak or no supporting evi
9	SIDG35088	46.6	SMARCB1	13	Pancreatic Carcinoma	Weak or no supporting evi
9	SIDG21711	45.6666667	NELFB	13	Pancreatic Carcinoma	Weak or no supporting evi
9	SIDG35136	45.375	SMG5	13	Pancreatic Carcinoma	Weak or no supporting evi
9	SIDG03585	45.2	CBX3	13	Pancreatic Carcinoma	Weak or no supporting evi
9	SIDG04324	45.2	CENPA	13	Pancreatic Carcinoma	Weak or no supporting evi
9	SIDG37545	44.8	TFDP1	13	Pancreatic Carcinoma	Weak or no supporting evi
9	SIDG36488	44.1818182	SRSF6	13	Pancreatic Carcinoma	Weak or no supporting evi
9	SIDG05350	44.1818182	CPSF1	13	Pancreatic Carcinoma	Weak or no supporting evi
9	SIDG11462	43.8823529	HMGA1	13	Pancreatic Carcinoma	Weak or no supporting evi
9	SIDG42464	43.8	ZWINT	13	Pancreatic Carcinoma	Weak or no supporting evi
9	SIDG21091	43.3333333	MYBL2	13	Pancreatic Carcinoma	Weak or no supporting evi
9	SIDG37726	43.3333333	TIMM23	13	Pancreatic Carcinoma	Weak or no supporting evi
9	SIDG06136	42	DCP2	13	Pancreatic Carcinoma	Weak or no supporting evi
9	SIDG11980	42	HSCB	13	Pancreatic Carcinoma	Weak or no supporting evi
9	SIDG07298	41	EDC4	13	Pancreatic Carcinoma	Weak or no supporting evi
9	SIDG13420	41	JUNB	13	Pancreatic Carcinoma	Weak or no supporting evi
10	SIDG05173	48.8235294	COPG1	13	Pancreatic Carcinoma	Weak or no supporting evi
10	SIDG37078	48	TAF1C	13	Pancreatic Carcinoma	Weak or no supporting evi
10	SIDG21829	48	NHP2	13	Pancreatic Carcinoma	Weak or no supporting evi
10	SIDG17493	45.25	MED12	13	Pancreatic Carcinoma	Weak or no supporting evi
10	SIDG33997	45	SEH1L	13	Pancreatic Carcinoma	Weak or no supporting evi
10	SIDG36783	44.5	STT3A	13	Pancreatic Carcinoma	Weak or no supporting evi
10	SIDG33483	44	RTCB	13	Pancreatic Carcinoma	Weak or no supporting evi
10	SIDG40160	43.6923077	UBE2S	13	Pancreatic Carcinoma	Weak or no supporting evi
10	SIDG04600	43	CHMP7	13	Pancreatic Carcinoma	Weak or no supporting evi
10	SIDG08530	42.4	CIAO2B	13	Pancreatic Carcinoma	Weak or no supporting evi
10	SIDG04389	42	CEP192	13	Pancreatic Carcinoma	Weak or no supporting evi
10	SIDG10781	41.4666667	GTF2F1	13	Pancreatic Carcinoma	Weak or no supporting evi
10	SIDG08224	40.5333333	EXOSC8	13	Pancreatic Carcinoma	Weak or no supporting evi
10	SIDG25288	40.3636364	POP7	13	Pancreatic Carcinoma	Weak or no supporting evi

8.4 GI50 values of LB-100 screened PDAC models

PDCL	GI_{50} [µM]
PDC56	9.317
PDC117	11.27
PaCaDD-159	14.18
PaCaDD-135	17.89
PaCaDD-119	18.43
PaCaDD-165	20.27
huPDAC17	23.31
PDC49	23.72
PaCaDD-137	25.87
B211	38.87
huPDAC11	57.32
PaCaDD-161	144.8
PDC40	166.5

Organoids	GI_{50} [µM]
B203	5.181
B250	6.42
B415	6.76
B188	7.824
B121	9.094
B253	14.596
B320	15.428
B358	15.928
B211	16.08
B379	18.052
B226	23.765
B273	30.235
B288	38.649
B169	105.968

Human PDAC	GI_{50} [µM]
MIA PaCa-2	12.54
HUPT3	14.83
PANC0504	19.83
ASPC1	22.87
HPAC	25.76
PATU8988S	32.82
HUPT4	60

Murine PDAC	GI_{50} [µM]
8248	18.81
8513	19.53
3250	20.07
S411	22.38
S914	24.04
16992	25.07
S134	26.44
8442	28.33
8349	28.88
8661	35.69
53631	37.42
16990	47.09
B590	47.99
4072	50.62
3202	52.04
5671	52.58
8570	53.22
8028	54.03
5123	54.34
4706	54.61
9091	57.02
53646	58.6
4900	60.33
5748	63.12
53578	70.96
S302	73.7
8182	75.02
2259	75.42
5320	76.55
6075	82.34
53704	83.36
S821	84.8
8305	87.2
9203	111.8
S559	138.1
R1035	140.8
8296	232.5
9591	622.7

9 References

1. Siegel, R. L., Miller, K. D., Fuchs, H. E. & Jemal, A. Cancer statistics, 2022. *CA. Cancer J. Clin.* **72**, 7–33 (2022).
2. Sung, H. *et al.* Global Cancer Statistics 2020: GLOBOCAN Estimates of Incidence and Mortality Worldwide for 36 Cancers in 185 Countries. *CA. Cancer J. Clin.* **71**, 209–249 (2021).
3. Siegel, R. L., Miller, K. D., Fuchs, H. E. & Jemal, A. Cancer Statistics, 2021. *CA. Cancer J. Clin.* **71**, 7–33 (2021).
4. Siegel, R. L., Miller, K. D. & Jemal, A. Cancer statistics, 2019. *CA. Cancer J. Clin.* **69**, 7–34 (2019).
5. Miller, K. D. *et al.* Cancer treatment and survivorship statistics, 2016. *CA. Cancer J. Clin.* **66**, 271–289 (2016).
6. Maisonneuve, P. Epidemiology and burden of pancreatic cancer. *Press. Medicale* **48**, e113–e123 (2019).
7. Siegel, R. L., Miller, K. D., Wagle, N. S. & Jemal, A. Cancer statistics, 2023. *CA. Cancer J. Clin.* **73**, 17–48 (2023).
8. Lambert, A. *et al.* An update on treatment options for pancreatic adenocarcinoma. *Ther. Adv. Med. Oncol.* **11**, (2019).
9. Mizrahi, J. D., Surana, R., Valle, J. W. & Shroff, R. T. Pancreatic cancer. *Lancet* **395**, 2008–2020 (2020).
10. Grossberg, A. J. *et al.* Multidisciplinary standards of care and recent progress in pancreatic ductal adenocarcinoma. *CA. Cancer J. Clin.* **70**, 375 (2020).
11. Park, W., Chawla, A. & O'Reilly, E. M. Pancreatic Cancer: A Review. *JAMA* **326**, 851–862 (2021).
12. Ducreux, M. *et al.* Cancer of the pancreas: ESMO Clinical Practice Guidelines for diagnosis, treatment and follow-up. *Ann. Oncol.* **26**, v56–v68 (2015).
13. Stolzenberg-Solomon, R. Z. & Amundadottir, L. T. Epidemiology and Inherited Predisposition for Sporadic Pancreatic Adenocarcinoma. *Hematol Oncol Clin N Am* **29**, 619–640 (2015).
14. Becker, A. E., Hernandez, Y. G., Frucht, H. & Lucas, A. L. Pancreatic ductal adenocarcinoma: Risk factors, screening, and early detection. *World J. Gastroenterol.* **20**, 11182 (2014).
15. Klein, A. P. Genetic susceptibility to pancreatic cancer. *Mol. Carcinog.* **51**, 14–24 (2012).
16. Rebours, V. *et al.* Obesity and fatty pancreatic infiltration are risk factors for pancreatic precancerous lesions (PanIN). *Clin. Cancer Res.* **21**, 3522–3528

(2015).

17. Gandini, S. *et al.* Metformin and cancer risk and mortality: A systematic review and meta-analysis taking into account biases and confounders. *Cancer Prev. Res.* **7**, 867–885 (2014).
18. Park, W., Chawla, A. & O'Reilly, E. M. Pancreatic Cancer: A Review. *JAMA - J. Am. Med. Assoc.* **326**, 851–862 (2021).
19. Raptis, D. A., Fessas, C., Belasyse-Smith, P. & Kurzawinski, T. R. Clinical presentation and waiting time targets do not affect prognosis in patients with pancreatic cancer. *Surg.* **8**, 239–246 (2010).
20. Porta, M. *et al.* Exocrine pancreatic cancer: symptoms at presentation and their relation to tumour site and stage. *Clin. Transl. Oncol.* **7**, 189–197 (2005).
21. Tempero, M. A. *et al.* NCCN Guidelines Insights: Pancreatic Adenocarcinoma, Version 1.2019: Featured Updates to the NCCN Guidelines. *J. Natl. Compr. Cancer Netw.* **17**, 202–210 (2019).
22. Neoptolemos, J. P. *et al.* Therapeutic developments in pancreatic cancer: current and future perspectives. *Nat. Rev. Gastroenterol. Hepatol. 2018 156* **15**, 333–348 (2018).
23. Burris, H. A. *et al.* Improvements in survival and clinical benefit with gemcitabine as first- line therapy for patients with advanced pancreas cancer: A randomized trial. *J. Clin. Oncol.* **15**, 2403–2413 (1997).
24. Goldstein, D. *et al.* nab-Paclitaxel plus gemcitabine for metastatic pancreatic cancer: long-term survival from a phase III trial. *J. Natl. Cancer Inst.* **107**, (2015).
25. Conroy, T. *et al.* FOLFIRINOX versus Gemcitabine for Metastatic Pancreatic Cancer. *N. Engl. J. Med.* **364**, 1817–1825 (2011).
26. Gourgou-Bourgade, S. *et al.* Impact of FOLFIRINOX compared with gemcitabine on quality of life in patients with metastatic pancreatic cancer: Results from the PRODIGE 4/ACCORD 11 randomized trial. *J. Clin. Oncol.* **31**, 23–29 (2013).
27. Springfeld, C. *et al.* Chemotherapy for pancreatic cancer. *Press. Medicale* **48**, e159–e174 (2019).
28. Puri, S., Folias, A. E. & Hebrok, M. Cell Stem Cell Perspective Plasticity and Dedifferentiation within the Pancreas: Development, Homeostasis, and Disease. (2015) doi:10.1016/j.stem.2014.11.001.
29. Orth, M. *et al.* Pancreatic ductal adenocarcinoma: biological hallmarks, current status, and future perspectives of combined modality treatment approaches. *Radiat. Oncol.* **14**, 141 (2019).
30. Kopp, J. L. *et al.* Identification of Sox9-Dependent Acinar-to-Ductal Reprogramming as the Principal Mechanism for Initiation of Pancreatic Ductal

Adenocarcinoma. *Cancer Cell* **22**, 737–750 (2012).

31. Friedlander, S. Y. G. *et al.* Context-Dependent Transformation of Adult Pancreatic Cells by Oncogenic K-Ras. *Cancer Cell* **16**, 379–389 (2009).
32. Jones, S. *et al.* Core signaling pathways in human pancreatic cancers revealed by global genomic analyses. *Science* **321**, 1801–1806 (2008).
33. Kanda, M. *et al.* Presence of Somatic Mutations in Most Early-Stage Pancreatic Intraepithelial Neoplasia. *Br. REPORTS Gastroenterol.* **142**, 730–733 (2012).
34. Morris, J. P., Wang, S. C. & Hebrok, M. KRAS, Hedgehog, Wnt and the twisted developmental biology of pancreatic ductal adenocarcinoma. *Nat. Rev. Cancer* **10**, 683–695 (2010).
35. Waddell, N. *et al.* Whole genomes redefine the mutational landscape of pancreatic cancer. *Nat. 2015 5187540* **518**, 495–501 (2015).
36. Altomare, D. A. *et al.* Frequent activation of AKT2 kinase in human pancreatic carcinomas. *J. Cell. Biochem.* **87**, 470–476 (2002).
37. Mueller, S. *et al.* Evolutionary routes and KRAS dosage define pancreatic cancer phenotypes. *Nature* **554**, 62–68 (2018).
38. Iguchi, E., Safgren, S. L., Marks, D. L., Olson, R. L. & Fernandez-Zapico, M. E. Pancreatic Cancer, A Mis-interpreter of the Epigenetic Language. *Yale J. Biol. Med.* **89**, 575–590 (2016).
39. Bailey, P. *et al.* Genomic analyses identify molecular subtypes of pancreatic cancer. *Nature* **531**, 47–52 (2016).
40. Collisson, E. A. *et al.* Subtypes of pancreatic ductal adenocarcinoma and their differing responses to therapy. *Nat. Med.* **17**, 500–503 (2011).
41. Puleo, F. *et al.* Stratification of Pancreatic Ductal Adenocarcinomas Based on Tumor and Microenvironment Features. *Gastroenterology* **155**, 1999-2013.e3 (2018).
42. Moffitt, R. A. *et al.* Virtual microdissection identifies distinct tumor- and stroma-specific subtypes of pancreatic ductal adenocarcinoma. *Nat. Genet.* **47**, 1168–1178 (2015).
43. Daemen, A. *et al.* Metabolite profiling stratifies pancreatic ductal adenocarcinomas into subtypes with distinct sensitivities to metabolic inhibitors. *Proc. Natl. Acad. Sci. U. S. A.* **112**, E4410-7 (2015).
44. Lomberk, G. *et al.* Distinct epigenetic landscapes underlie the pathobiology of pancreatic cancer subtypes. *Nat. Commun.* **9**, 1978 (2018).
45. Chan-Seng-Yue, M. *et al.* Transcription phenotypes of pancreatic cancer are driven by genomic events during tumor evolution. *Nat. Genet.* **52**, 231–240 (2020).
46. Collisson, E. A., Bailey, P., Chang, D. K. & Biankin, A. V. Molecular subtypes of

pancreatic cancer. *Nature Reviews Gastroenterology and Hepatology* vol. 16 207–220 (2019).

47. Badea, L., Herlea, V., Dima, S. O., Dumitrascu, T. & Popescu, I. Combined gene expression analysis of whole-tissue and microdissected pancreatic ductal adenocarcinoma identifies genes specifically overexpressed in tumor epithelia. *Hepatogastroenterology.* **55**, 2016–2027 (2008).
48. Regel, I., Mayerle, J. & Mahajan, U. M. Current Strategies and Future Perspectives for Precision Medicine in Pancreatic Cancer. *Cancers (Basel).* **12**, (2020).
49. Jackson, E. L. *et al.* Analysis of lung tumor initiation and progression using conditional expression of oncogenic K-ras. *Genes Dev.* **15**, 3243 (2001).
50. Colvin, E. K. & Scarlett, C. J. A historical perspective of pancreatic cancer mouse models. *Semin. Cell Dev. Biol.* **27**, 96–105 (2014).
51. Hingorani, S. R. *et al.* Preinvasive and invasive ductal pancreatic cancer and its early detection in the mouse. *Cancer Cell* **4**, 437–450 (2003).
52. Schönhuber, N. *et al.* A next-generation dual-recombinase system for time and host specific targeting of pancreatic cancer. *Nat. Med.* **20**, 1340 (2014).
53. Aguirre, A. J. *et al.* Activated Kras and Ink4a/Arf deficiency cooperate to produce metastatic pancreatic ductal adenocarcinoma. *Genes Dev.* **17**, 3112–3126 (2003).
54. Bardeesy, N. *et al.* Both p16(Ink4a) and the p19(Arf)-p53 pathway constrain progression of pancreatic adenocarcinoma in the mouse. *Proc. Natl. Acad. Sci. U. S. A.* **103**, 5947–5952 (2006).
55. Morton, J. P. *et al.* Mutant p53 drives metastasis and overcomes growth arrest/senescence in pancreatic cancer. *Proc. Natl. Acad. Sci. U. S. A.* **107**, 246 (2010).
56. Kojima, K. *et al.* Inactivation of Smad4 accelerates Kras(G12D)-mediated pancreatic neoplasia. *Cancer Res.* **67**, 8121–8130 (2007).
57. Skoulidis, F. *et al.* Germline Brca2 heterozygosity promotes Kras(G12D) -driven carcinogenesis in a murine model of familial pancreatic cancer. *Cancer Cell* **18**, 499–509 (2010).
58. Rowley, M. *et al.* Inactivation of Brca2 promotes Trp53-associated but inhibits KrasG12D-dependent pancreatic cancer development in mice. *Gastroenterology* **140**, 1303 (2011).
59. Feldmann, G. *et al.* Inactivation of Brca2 cooperates with Trp53R172H to induce invasive pancreatic ductal adenocarcinomas in mice: A mouse model of familial pancreatic cancer. *Cancer Biol. Ther.* **11**, 959 (2011).

60. Morton, J. P. *et al.* LKB1 haploinsufficiency cooperates with Kras to promote pancreatic cancer through suppression of p21-dependent growth arrest. *Gastroenterology* **139**, 586–97, 597.e1–6 (2010).
61. Mann, K. M. *et al.* Sleeping Beauty mutagenesis reveals cooperating mutations and pathways in pancreatic adenocarcinoma. *Proc. Natl. Acad. Sci. U. S. A.* **109**, 5934–5941 (2012).
62. Pérez-Mancera, P. A. *et al.* The deubiquitinase USP9X suppresses pancreatic ductal adenocarcinoma. *Nature* **486**, 266 (2012).
63. Hassan, Z. *et al.* MTOR inhibitor-based combination therapies for pancreatic cancer. *Br. J. Cancer 2018 1183* **118**, 366–377 (2018).
64. Hassan, Z. Role of NFkB2 and MTOR in Pancreatic Ductal Adenocarcinoma. (Technische Univesität München, 2020).
65. Müller, S. Evolutionary trajectories and KRAS dosage define pancreatic cancer phenotypes. (Technische Universität München, 2020).
66. Conibear, A. C. Deciphering protein post-translational modifications using chemical biology tools. *Nat. Rev. Chem. 2020 412* **4**, 674–695 (2020).
67. NOLAN, C., NOVOA, W. B., KREBS, E. G. & FISCHER, E. H. FURTHER STUDIES ON THE SITE PHOSPHORYLATED IN THE PHOSPHORYLASE B TO A REACTION. *Biochemistry* **3**, 542–551 (1964).
68. Eichhorn, P. J. A., Creyghton, M. P. & Bernards, R. Protein phosphatase 2A regulatory subunits and cancer. *Biochimica et Biophysica Acta - Reviews on Cancer* vol. 1795 1–15 (2009).
69. Chen, M. J., Dixon, J. E. & Manning, G. Genomics and evolution of protein phosphatases. *Sci. Signal.* **10**, (2017).
70. Kerk, D. *et al.* The origin and radiation of the phosphoprotein phosphatase (PPP) enzymes of Eukaryotes. *Sci. Reports 2021 111* **11**, 1–13 (2021).
71. Seshacharyulu, P., Pandey, P., Datta, K. & Batra, S. K. Phosphatase: PP2A structural importance, regulation and its aberrant expression in cancer. (2013) doi:10.1016/j.canlet.2013.02.036.
72. Nasa, I. & Kettenbach, A. N. Coordination of protein kinase and phosphoprotein phosphatase activities in mitosis. *Front. Cell Dev. Biol.* **6**, 1–14 (2018).
73. Olsen, J. V. *et al.* Global, In Vivo, and Site-Specific Phosphorylation Dynamics in Signaling Networks. *Cell* **127**, 635–648 (2006).
74. Cho, U. S. & Xu, W. Crystal structure of a protein phosphatase 2A heterotrimeric holoenzyme. *Nature* **445**, 53–57 (2007).
75. Mumby, M. C. & Walter, G. Protein serine/threonine phosphatases: Structure, regulation, and functions in cell growth. *Physiological Reviews* vol. 73 673–699

(1993).

76. Wlodarchak, N. & Xing, Y. PP2A as a master regulator of the cell cycle. *Critical Reviews in Biochemistry and Molecular Biology* vol. 51 162–184 (2016).
77. Martin, M., Kettmann, R. & Dequiedt, F. Recent insights into Protein Phosphatase 2A structure and regulation: The reasons why PP2A is no longer considered as a lazy passive housekeeping enzyme. *Biotechnol. Agron. Soc. Environ.* **14**, 243–252 (2010).
78. Yoo, S. J. S., Boylan, J. M., Brautigan, D. L. & Gruppuso, P. A. Subunit composition and developmental regulation of hepatic protein phosphatase 2A (PP2A). *Arch. Biochem. Biophys.* **461**, 186–193 (2007).
79. Janssens, V. & Goris, J. Protein phosphatase 2A : a highly regulated family of serine/threonine phosphatases implicated in cell growth and signalling. *Biochem. J* **353**, 417–439 (2001).
80. Stanevich, V. *et al.* The Structural Basis for Tight Control of PP2A Methylation and Function by LCMT-1. *Mol. Cell* **41**, 331–342 (2011).
81. Jiang, L. *et al.* Structural basis of protein phosphatase 2A stable latency. *Nat. Commun.* **4**, 1699 (2013).
82. Short, K. M., Hopwood, B., Yi, Z. & Cox, T. C. MID1 and MID2 homo- and heterodimerise to tether the rapamycin-sensitive PP2A regulatory subunit, Alpha 4, to microtubules: Implications for the clinical variability of X-linked Opitz GBBB syndrome and other developmental disorders. *BMC Cell Biol.* **3**, 1 (2002).
83. Guo, F. *et al.* Structural basis of PP2A activation by PTPA, an ATPdependent activation chaperone. *Cell Res.* **24**, 190–203 (2014).
84. Longin, S. *et al.* Selection of protein phosphatase 2A regulatory subunits is mediated by the C terminus of the catalytic subunit. *J. Biol. Chem.* **282**, 26971–26980 (2007).
85. Chen, J., Martin, B. L. & Brautigan, D. L. Regulation of protein serine-threonine phosphatase type-2A by tyrosine phosphorylation. *Science (80-.).* **257**, 1261–1264 (1992).
86. Kloeker, S. *et al.* Parallel purification of three catalytic subunits of the protein serine/threonine phosphatase 2A family (PP2A(C), PP4(C), and PP6(C)) and analysis of the interaction of PP2A(C) with alpha4 protein. *Protein Expr. Purif.* **31**, 19–33 (2003).
87. Zheng, H. *et al.* Identification of Integrator-PP2A complex (INTAC), an RNA polymerase II phosphatase. *Science (80-.).* **370**, (2020).
88. Kaur, A. & Westermarck, J. Regulation of protein phosphatase 2A (PP2A) tumor suppressor function by PME-1. *Biochem. Soc. Trans.* **44**, 1683–1693 (2016).

89. TUNG, H. Y. L., ALEMANY, S. & COHEN, P. The protein phosphatases involved in cellular regulation. 2. Purification, subunit structure and properties of protein phosphatases-2Ao, 2A1, and 2A2 from rabbit skeletal muscle. *Eur. J. Biochem.* **148**, 253–263 (1985).

90. Lee, T.-Y. *et al.* The B563 Regulatory Subunit of Protein Phosphatase 2A (PP2A) Regulates S Phase-specific Nuclear Accumulation of PP2A and the G 1 to S Transition * □ S. (2010) doi:10.1074/jbc.M109.094953.

91. Perrotti, D. & Neviani, P. Targeting A Tumor Suppressor To Suppress Tumor Growth: News and Views on Protein Phosphatase 2A (PP2A) as a Target for Anti-cancer Therapy. *Lancet Oncol* **14**, 229–238 (2013).

92. Junttila, M. R. *et al.* CIP2A Inhibits PP2A in Human Malignancies. *Cell* **130**, 51–62 (2007).

93. Janssens, V. & Rebollo, A. The Role and Therapeutic Potential of Ser/Thr Phosphatase PP2A in Apoptotic Signalling Networks in Human Cancer Cells. *Curr. Mol. Med.* **12**, 268–287 (2012).

94. Sontag, J. M. & Sontag, E. Protein phosphatase 2A dysfunction in Alzheimer's disease. *Front. Mol. Neurosci.* **7**, (2014).

95. Kowluru, A. & Matti, A. Hyperactivation of protein phosphatase 2A in models of glucolipotoxicity and diabetes: Potential mechanisms and functional consequences. *Biochemical Pharmacology* vol. 84 591–597 (2012).

96. Ruvolo, P. P. The broken "Off" switch in cancer signaling: PP2A as a regulator of tumorigenesis, drug resistance, and immune surveillance. *BBA Clinical* vol. 6 87–99 (2016).

97. Reynhout, S. & Janssens, V. Physiologic functions of PP2A: Lessons from genetically modified mice. *Biochimica et Biophysica Acta - Molecular Cell Research* (2019) doi:10.1016/j.bbamcr.2018.07.010.

98. Sents, W., Ivanova, E., Lambrecht, C., Haesen, D. & Janssens, V. The biogenesis of active protein phosphatase 2A holoenzymes: A tightly regulated process creating phosphatase specificity. *FEBS J.* **280**, 644–661 (2013).

99. Chen, W., Wang, Z., Jiang, C. & Ding, Y. PP2A-mediated anticancer therapy. *Gastroenterol. Res. Pract.* **2013**, (2013).

100. Sangodkar, J. *et al.* All roads lead to PP2A: Exploiting the therapeutic potential of this phosphatase. **283**, 1004–1024 (2017).

101. Fujiki, H. & Suganuma, M. Tumor Promotion by Inhibitors of ProteinZ Phosphatases 1 and 2A: The Okadaic Acid Class of Compounds. *Adv. Cancer Res.* **61**, 143–194 (1993).

102. Nagao, M., Shima, H., Nakayasu, M. & Sugimura, T. Protein serine/threonine

phosphatases as binding proteins for okadaic acid. *Mutat. Res.* **333**, 173–179 (1995).

103. Chen, W. *et al.* Identification of specific PP2A complexes involved in human cell transformation. *Cancer Cell* **5**, 127–136 (2004).
104. Uhn, S. C. *et al.* Structural basis of PP2A inhibition by small t antigen. *PLoS Biol.* **5**, 1810–1819 (2007).
105. Arriazu, E., Pippa, R. & Odero, M. D. Protein phosphatase 2A as a therapeutic target in acute myeloid leukemia. *Front. Oncol.* **6**, 78 (2016).
106. Cristòbal, I. *et al.* Potential anti-tumor effects of FTY720 associated with PP2A activation: a brief review. *Curr. Med. Res. Opin.* **32**, 1137–1141 (2016).
107. Guénin, S. *et al.* PP2A activity is controlled by methylation and regulates oncoprotein expression in melanoma cells: A mechanism which participates in growth inhibition induced by chloroethylnitrosourea treatment. *Int. J. Oncol.* **32**, 49–57 (2008).
108. Janssens, V., Goris, J. & Van Hoof, C. PP2A: the expected tumor suppressor. *Curr. Opin. Genet. Dev.* **15**, 34–41 (2005).
109. Liu, Z. *et al.* Cancerous inhibitor of PP2A is targeted by natural compound celastrol for degradation in non-small-cell lung cancer. *Carcinogenesis* **35**, 905–914 (2014).
110. Liu, Z., Ma, L., Wen, Z. S., Cheng, Y. X. & Zhou, G. B. Ethoxysanguinarine Induces Inhibitory Effects andDownregulates CIP2A in Lung Cancer Cells. *ACS Med. Chem. Lett.* **5**, 113 (2014).
111. Tseng, L. M. *et al.* CIP2A is a target of bortezomib in human triple negative breast cancer cells. *Breast Cancer Res.* **14**, (2012).
112. Chen, K. F. *et al.* Bortezomib overcomes tumor necrosis factor-related apoptosis-inducing ligand resistance in hepatocellular carcinoma cells in part through the inhibition of the phosphatidylinositol 3-kinase/Akt pathway. *J. Biol. Chem.* **284**, 11121–11133 (2009).
113. Chen, K. F. *et al.* Development of erlotinib derivatives as CIP2A-ablating agents independent of EGFR activity. *Bioorg. Med. Chem.* **20**, 6144–6153 (2012).
114. Kauko, O. *et al.* PP2A inhibition is a druggable MEK inhibitor resistance mechanism in KRAS-mutant lung cancer cells. *Sci. Transl. Med.* **10**, (2018).
115. Mazhar, S., Taylor, S. E., Sangodkar, J. & Narla, G. Targeting PP2A in cancer: Combination therapies. *Biochimica et Biophysica Acta - Molecular Cell Research* vol. 1866 51–63 (2019).
116. Chien, W. *et al.* Activation of protein phosphatase 2A tumor suppressor as potential treatment of pancreatic cancer. *Mol. Oncol.* **9**, 889–905 (2015).

117. Gutierrez, A. *et al.* Phenothiazines induce PP2A-mediated apoptosis in T cell acute lymphoblastic leukemia. *J. Clin. Invest.* **124**, 644 (2014).
118. Jones, T. A. *et al.* Localization of the genes encoding the catalytic subunits of protein phosphatase 2A to human chromosome bands 5q23-->q31 and 8p12-->p11.2, respectively. *Cytogenet. Cell Genet.* **63**, 35–4l (1993).
119. Sallman, D. A., Wei, S. & List, A. PP2A: The achilles heal in MDS with 5q deletion. *Front. Oncol.* **4**, 264 (2014).
120. Wei, S. *et al.* A critical role for phosphatase haplodeficiency in the selective suppression of deletion 5q MDS by lenalidomide. *Proc. Natl. Acad. Sci. U. S. A.* **106**, 12974–12979 (2009).
121. List, A. F. *et al.* Extended survival and reduced risk of AML progression in erythroid-responsive lenalidomide-treated patients with lower-risk del(5q) MDS. *Leuk. 2014 285* **28**, 1033–1040 (2013).
122. Kiely, M. & Kiely, P. A. PP2A: The wolf in sheep's clothing? *Cancers (Basel).* **7**, 648–669 (2015).
123. Li, W. *et al.* Cantharidin, a potent and selective PP2A inhibitor, induces an oxidative stress-independent growth inhibition of pancreatic cancer cells through G2/M cell-cycle arrest and apoptosis. *Cancer Sci.* **101**, 1226–1233 (2010).
124. Huang, Y., Liu, Q., Liu, K., Yagasaki, K. & Zhang, G. Suppression of growth of highly-metastatic human breast cancer cells by norcantharidin and its mechanisms of action. *Cytotechnology* **59**, 201 (2009).
125. Liu, S. *et al.* Norcantharidin induces melanoma cell apoptosis through activation of TR3 dependent pathway. *Cancer Biol. Ther.* **12**, 1005 (2011).
126. Kok, S. H. *et al.* Comparisons of norcantharidin cytotoxic effects on oral cancer cells and normal buccal keratinocytes. *Oral Oncol.* **39**, 19–26 (2003).
127. Zhang, J. T. *et al.* Norcantharidin inhibits tumor growth and vasculogenic mimicry of human gallbladder carcinomas by suppression of the PI3-K/MMPs/Ln-5γ2 signaling pathway. *BMC Cancer* **14**, 1–17 (2014).
128. To, K. K. W., Ho, Y. P. & Au-Yeung, S. C. R. In vitro and in vivo suppression of growth of hepatocellular carcinoma cells by novel traditional Chinese medicine-platinum anti-cancer agents. *Anticancer. Drugs* **16**, 825–835 (2005).
129. Qi, X. M., Wang, F., Mortensen, M., Wertz, R. & Chen, G. Targeting an oncogenic kinase/phosphatase signaling network for cancer therapy. *Acta Pharm. Sin. B* **8**, 511–517 (2018).
130. Xing, Y. *et al.* Structural Mechanism of Demethylation and Inactivation of Protein Phosphatase 2A. *Cell* **133**, 154–163 (2008).
131. Roskoski, R. J. Properties of FDA-approved small molecule protein kinase

inhibitors: A 2023 update. *Pharmacol. Res.* **187**, 106552 (2023).

132. Roskoski, R. Properties of FDA-approved small molecule protein kinase inhibitors: A 2022 update. *Pharmacol. Res.* **175**, (2022).
133. Bechman, K., Yates, M. & Galloway, J. B. The new entries in the therapeutic armamentarium: The small molecule JAK inhibitors. *Pharmacol. Res.* **147**, 104392 (2019).
134. Turdo, A. *et al.* Targeting Phosphatases and Kinases: How to Checkmate Cancer. *Front. Cell Dev. Biol.* **9**, 2979 (2021).
135. Pan, J., Zhou, L., Zhang, C., Xu, Q. & Sun, Y. Targeting protein phosphatases for the treatment of inflammation-related diseases: From signaling to therapy. *Signal Transduct. Target. Ther. 2022 71* **7**, 1–24 (2022).
136. Kovach. (12) United States Patent45) Date of Patent: (54) (75) (73) (*) (21) (22) (65) (60) (51) (52) (58) OXABICYCLOHEPTANES AND OXABICYLCOHEPTENES, THEIR PREPARATION AND USE. (2011).
137. Chung, V. *et al.* Safety, tolerability, and preliminary activity of LB-100, an inhibitor of protein phosphatase 2A, in patients with relapsed solid tumors: An open-label, dose escalation, first-in-human, phase I trial. *Clin. Cancer Res.* **23**, 3277–3284 (2017).
138. Lu, J. *et al.* Inhibition of serine/threonine phosphatase PP2A enhances cancer chemotherapy by blocking DNA damage induced defense mechanisms. *Proc. Natl. Acad. Sci. U. S. A.* **106**, 11697 (2009).
139. D'Arcy, B. M. *et al.* The Antitumor Drug LB-100 is a Catalytic Inhibitor of ProteinPhosphatase 2A (PPP2CA) and 5 (PPP5C) Coordinating with the Active SiteCatalytic Metals in PPP5C. *Mol. Cancer Ther.* **18**, 556 (2019).
140. Lu, J. *et al.* The effect of a PP2A inhibitor on the nuclear receptor corepressor pathway in glioma. *J. Neurosurg.* **113**, 225–233 (2010).
141. Hong, C. S. *et al.* LB100, a small molecule inhibitor of PP2A with potent chemo- and radio-sensitizing potential. *Cancer Biol. Ther.* **16**, 821 (2015).
142. Zhang, C. *et al.* A synthetic cantharidin analog for the enhancement of doxorubicin suppression of stem cell-derived aggressive sarcoma. *Biomaterials* **31**, 9535–9543 (2010).
143. Bai, X. L. *et al.* Inhibition of protein phosphatase 2A enhances cytotoxicity and accessibility of chemotherapeutic drugs to hepatocellular carcinomas. *Mol. Cancer Ther.* **13**, 2062–2072 (2014).
144. Bai, X. *et al.* Inhibition of protein phosphatase 2A sensitizes pancreatic cancer to chemotherapy by increasing drug perfusion via HIF-1α-VEGF mediated angiogenesis. *Cancer Lett.* **355**, 281–287 (2014).

145. Wei, D. *et al.* Inhibition of protein phosphatase 2A radiosensitizes pancreatic cancers by modulating CDC25C/CDK1 and homologous recombination repair. *Clin. Cancer Res.* **19**, 4422 (2013).
146. Lê, L. H. *et al.* Phase I and pharmacokinetic study of fostriecin given as an intravenous bolus daily for five consecutive days. *Invest. New Drugs* **22**, 159–167 (2004).
147. Martiniova, L. *et al.* Pharmacologic Modulation of Serine/Threonine Phosphorylation Highly Sensitizes PHEO in a MPC Cell and Mouse Model to Conventional Chemotherapy. *PLoS One* **6**, e14678 (2011).
148. Lu, J. *et al.* Inhibition of serine/threonine phosphatase PP2A enhances cancer chemotherapy by blocking DNA damage induced defense mechanisms. *Proc. Natl. Acad. Sci. U. S. A.* **106**, 11697–11702 (2009).
149. U.S. National Institute of Health. ClinicalTrials.gov. https://clinicaltrials.gov/ct2/home.
150. Lier, S. Technische Universität München. (Technical University of Munich, 2022).
151. Bradford, M. M. A rapid and sensitive method for the quantitation of microgram quantities of protein utilizing the principle of protein-dye binding. *Anal. Biochem.* **72**, 248–254 (1976).
152. Laemmli, U. K. Cleavage of Structural Proteins during the Assembly of the Head of Bacteriophage T4. *Nat. 1970 2275259* **227**, 680–685 (1970).
153. Burnette, W. N. 'Western blotting': electrophoretic transfer of proteins from sodium dodecyl sulfate--polyacrylamide gels to unmodified nitrocellulose and radiographic detection with antibody and radioiodinated protein A. *Anal. Biochem.* **112**, 195–203 (1981).
154. Ravi, V., Jain, A., Mishra, S. & Sundaresan, N. R. Measuring Protein Synthesis in Cultured Cells and Mouse Tissues Using the Non-radioactive SUnSET Assay. *Curr. Protoc. Mol. Biol.* **133**, 1–23 (2020).
155. Schneider, C. A., Rasband, W. S. & Eliceiri, K. W. NIH Image to ImageJ: 25 years of image analysis. *Nat. Methods 2012 97* **9**, 671–675 (2012).
156. Orben, F. *et al.* Epigenetic drug screening defines a PRMT5 inhibitor-sensitive pancreatic cancer subtype. *JCI Insight* **7**, (2022).
157. Parekh, S., Ziegenhain, C., Vieth, B., Enard, W. & Hellmann, I. The impact of amplification on differential expression analyses by RNA-seq. *Sci. Rep.* **6**, 1–11 (2016).
158. Dobin, A. *et al.* STAR: ultrafast universal RNA-seq aligner. *Bioinformatics* **29**, 15–21 (2013).
159. Quinlan, A. R. & Hall, I. M. BEDTools: a flexible suite of utilities for comparing

genomic features. *Bioinformatics* **26**, 841–842 (2010).

160. Kent, W. J. *et al.* The human genome browser at UCSC. *Genome Res.* **12**, 996–1006 (2002).
161. Yates, A. *et al.* Ensembl 2016. *Nucleic Acids Res.* **44**, D710–D716 (2016).
162. Harrow, J. *et al.* GENCODE: the reference human genome annotation for The ENCODE Project. *Genome Res.* **22**, 1760–1774 (2012).
163. Anders, S. & Huber, W. Differential expression analysis for sequence count data. *Genome Biol.* **11**, 1–12 (2010).
164. Boutz, P. L., Bhutkar, A. & Sharp, P. A. Detained introns are a novel, widespread class of post-transcriptionally spliced introns. *Genes Dev.* **29**, 63–80 (2015).
165. Anders, S., Reyes, A. & Huber, W. Detecting differential usage of exons from RNA-seq data. *Genome Res.* **22**, 2008–2017 (2012).
166. Park, J. W., Tokheim, C., Shen, S. & Xing, Y. Identifying differential alternative splicing events from RNA sequencing data using RNASeq-MATS. *Methods Mol. Biol.* **1038**, 171–179 (2013).
167. Liao, Y., Smyth, G. K. & Shi, W. featureCounts: an efficient general purpose program for assigning sequence reads to genomic features. *Bioinformatics* **30**, 923–930 (2014).
168. Joung, J. *et al.* Genome-scale CRISPR-Cas9 knockout and transcriptional activation screening. *Nat. Protoc.* **12**, 828–863 (2017).
169. Falcomatà, C. *et al.* Selective multi-kinase inhibition sensitizes mesenchymal pancreatic cancer to immune checkpoint blockade by remodeling the tumor microenvironment. *Nat. Cancer* **3**, 318–336 (2022).
170. Griger, J. *et al.* An integrated cellular and molecular model of gastric neuroendocrine cancer evolution highlights therapeutic targets. *Cancer Cell* **41**, 1327-1344.e10 (2023).
171. The Galaxy Community. The Galaxy platform for accessible, reproducible and collaborative biomedical analyses: 2022 update. *Nucleic Acids Res.* **50**, W345–W351 (2022).
172. Ewels, P., Magnusson, M., Lundin, S. & Käller, M. MultiQC: summarize analysis results for multiple tools and samples in a single report. *Bioinformatics* **32**, 3047–3048 (2016).
173. Bolger, A. M., Lohse, M. & Usadel, B. Trimmomatic: a flexible trimmer for Illumina sequence data. *Bioinformatics* **30**, 2114–2120 (2014).
174. Wang, B. *et al.* Integrative analysis of pooled CRISPR genetic screens using MAGeCKFlute. *Nat. Protoc.* **14**, 756 (2019).
175. Gerstner, N. *et al.* GeneTrail 3: advanced high-throughput enrichment analysis.

Nucleic Acids Res. **48**, 515–520 (2020).

176. Huang, K. L. *et al.* Integrator Recruits Protein Phosphatase 2A to Prevent Pause Release and Facilitate Transcription Termination. *Mol. Cell* **80**, 345-358.e9 (2020).
177. Behan, F. M. *et al.* Prioritization of cancer therapeutic targets using CRISPR-Cas9 screens. *Nature* **568**, 511–516 (2019).
178. Dempster, J. M. *et al.* Chronos: a cell population dynamics model of CRISPR experiments that improves inference of gene fitness effects. *Genome Biol.* **22**, 343 (2021).
179. Tang, Z. *et al.* GEPIA: a web server for cancer and normal gene expression profiling and interactive analyses. *Nucleic Acids Res.* **45**, W98–W102 (2017).
180. Schmidt, T. *et al.* ProteomicsDB. *Nucleic Acids Res.* **46**, D1271–D1281 (2018).
181. Lier, S. *et al.* A novel Cereblon E3 ligase modulator with antitumor activity in gastrointestinal cancer. *Bioorg. Chem.* **119**, 105505 (2022).
182. Subramanian, A. *et al.* Gene set enrichment analysis: A knowledge-based approach for interpreting genome-wide expression profiles. *Proc. Natl. Acad. Sci. U. S. A.* **102**, 15545–15550 (2005).
183. Mootha, V. K. *et al.* A R T I C L E S PGC-1α-responsive genes involved in oxidative phosphorylation are coordinately downregulated in human diabetes. *Nat. Genet. Vol.* **34**, (2003).
184. Ge, S. X., Jung, D. & Yao, R. ShinyGO: a graphical gene-set enrichment tool for animals and plants. *Bioinformatics* **36**, 2628–2629 (2020).
185. Pettersen, E. F. *et al.* UCSF Chimera--a visualization system for exploratory research and analysis. *J. Comput. Chem.* **25**, 1605–1612 (2004).
186. Behan, F. M. *et al.* Prioritization of cancer therapeutic targets using CRISPR-Cas9 screens. *Nature* **568**, 511–516 (2019).
187. Du, R., Huang, C., Liu, K., Li, X. & Dong, Z. Targeting AURKA in Cancer: molecular mechanisms and opportunities for Cancer therapy. *Mol. Cancer 2021 201* **20**, 1–27 (2021).
188. Goodwin, C. M. *et al.* Combination Therapies with CDK4/6 Inhibitors to Treat KRAS-Mutant Pancreatic Cancer. *Cancer Res.* **83**, 141–157 (2023).
189. Salvador-Barbero, B. *et al.* CDK4/6 Inhibitors Impair Recovery from Cytotoxic Chemotherapy in Pancreatic Adenocarcinoma. *Cancer Cell* **37**, 340-353.e6 (2020).
190. Singh, K. *et al.* Targeting eIF4A-dependent translation of KRAS signaling molecules. *Cancer Res.* **81**, 2002–2014 (2021).
191. Bewick, V., Cheek, L. & Ball, J. Statistics review 12: Survival analysis. *Crit. Care*

8, 389 (2004).

192. Lankes, K. *et al.* Targeting the ubiquitin-proteasome system in a pancreatic cancer subtype with hyperactive MYC. *Mol. Oncol.* **14**, 3048–3064 (2020).
193. Peisl, S. *et al.* Therapeutic targeting of STAT3 pathways in pancreatic adenocarcinoma: A systematic review of clinical and preclinical literature. *PLoS One* **16**, (2021).
194. Rajagopal, M. U. *et al.* TGFβ Drives Metabolic Perturbations during Epithelial Mesenchymal Transition in Pancreatic Cancer: TGFβ Induced EMT in PDAC. *Cancers (Basel).* **13**, (2021).
195. Krauß, L. *et al.* HDAC2 Facilitates Pancreatic Cancer Metastasis. *Cancer Res.* **82**, 695–707 (2022).
196. Lin, S. *et al.* Comparison of the transcriptional landscapes between human and mouse tissues. *Proc. Natl. Acad. Sci. U. S. A.* **111**, 17224–17229 (2014).
197. Shichi, Y. *et al.* Epithelial and Mesenchymal Features of Pancreatic Ductal Adenocarcinoma Cell Lines in Two- and Three-Dimensional Cultures. *J. Pers. Med.* **12**, 746 (2022).
198. Yue, J. *et al.* Targeted chemotherapy overcomes drug resistance in melanoma. *Genes Dev.* **34**, 637–649 (2020).
199. Kim, J., Koo, B. K. & Knoblich, J. A. Human organoids: model systems for human biology and medicine. *Nat. Rev. Mol. Cell Biol. 2020 2110* **21**, 571–584 (2020).
200. Mechanism matters. *Nat. Med. 2010 164* **16**, 347–347 (2010).
201. Marcelo, A., Koppenol, R., de Almeida, L. P., Matos, C. A. & Nóbrega, C. Stress granules, RNA-binding proteins and polyglutamine diseases: too much aggregation? *Cell Death Dis. 2021 126* **12**, 1–17 (2021).
202. Tian, X. *et al.* Targeting the Integrated Stress Response in Cancer Therapy. *Front. Pharmacol.* **12**, 2621 (2021).
203. Pakos-Zebrucka, K. *et al.* The integrated stress response. *EMBO Rep.* **17**, 1374–1395 (2016).
204. Wu, Y., Zhang, Z., Li, Y. & Li, Y. The Regulation of Integrated Stress Response Signaling Pathway on Viral Infection and Viral Antagonism. *Front. Microbiol.* **12**, 4199 (2022).
205. Xi, H. *et al.* The role of interaction between autophagy and apoptosis in tumorigenesis (Review). *Oncol. Rep.* **48**, 1–16 (2022).
206. Vance, J. E. Phospholipid synthesis in a membrane fraction associated with mitochondria. *J. Biol. Chem.* **265**, 7248–7256 (1990).
207. Malhotra, J. D. & Kaufman, R. J. ER Stress and Its Functional Link to Mitochondria: Role in Cell Survival and Death. *Cold Spring Harb. Perspect. Biol.*

3, 1–13 (2011).

208. Ren, L. *et al.* Mitochondrial Dynamics: Fission and Fusion in Fate Determination of Mesenchymal Stem Cells. *Front. Cell Dev. Biol.* **8**, 1133 (2020).
209. Gu, X., Ma, Y., Liu, Y. & Wan, Q. Measurement of mitochondrial respiration in adherent cells by Seahorse XF96 Cell Mito Stress Test. *STAR Protoc.* **2**, 100245 (2021).
210. Lai, H. T. *et al.* Insight into the interplay between mitochondria-regulated cell death and energetic metabolism in osteosarcoma. *Front. Cell Dev. Biol.* **10**, (2022).
211. Mauthe, M. *et al.* Chloroquine inhibits autophagic flux by decreasing autophagosome-lysosome fusion. *Autophagy* **14**, 1435–1455 (2018).
212. Bock, C. *et al.* High-content CRISPR screening. *Nat. Rev. Methods Prim. 2022 21* **2**, 1–23 (2022).
213. Doench, J. G. *et al.* Optimized sgRNA design to maximize activity and minimize off-target effects of CRISPR-Cas9. *Nat. Biotechnol.* **34**, 184–191 (2016).
214. Armingol, E., Officer, A., Harismendy, O. & Lewis, N. E. Deciphering cell–cell interactions and communication from gene expression. *Nat. Rev. Genet. 2020 222* **22**, 71–88 (2020).
215. Szklarczyk, D. *et al.* The STRING database in 2023: protein-protein association networks and functional enrichment analyses for any sequenced genome of interest. *Nucleic Acids Res.* **51**, D638–D646 (2023).
216. Paronetto, M. P., Passacantilli, I. & Sette, C. Alternative splicing and cell survival: from tissue homeostasis to disease. *Cell Death Differ.* **23**, 1919 (2016).
217. Chao, Y. *et al.* Regulatory roles and mechanisms of alternative RNA splicing in adipogenesis and human metabolic health. *Cell Biosci. 2021 111* **11**, 1–16 (2021).
218. Aguiar, D. *et al.* Bayesian nonparametric discovery of isoforms and individual specific quantification. *Nat. Commun. 2018 91* **9**, 1–12 (2018).
219. Herzel, L., Ottoz, D. S. M., Alpert, T. & Neugebauer, K. M. Splicing and transcription touch base: co-transcriptional spliceosome assembly and function. *Nat. Rev. Mol. Cell Biol. 2017 1810* **18**, 637–650 (2017).
220. Kornblihtt, A. R., De La Mata, M., Fededa, J. P., Muñoz, M. J. & Nogués, G. Multiple links between transcription and splicing. *RNA* **10**, 1489 (2004).
221. Tellier, M., Maudlin, I. & Murphy, S. Transcription and splicing: A two-way street. *Wiley Interdiscip. Rev. RNA* **11**, 1–25 (2020).
222. Madsen, J. G. S. *et al.* iRNA-seq: computational method for genome-wide assessment of acute transcriptional regulation from total RNA-seq data. *Nucleic Acids Res.* **43**, e40 (2015).
223. Eghbalnia, H. R., Wilfinger, W. W., Mackey, K. & Chomczynski, P. Coordinated

analysis of exon and intron data reveals novel differential gene expression changes. *Sci. Reports 2020 101* **10**, 1–13 (2020).

224. Welsh, S. A. & Gardini, A. Genomic regulation of transcription and RNA processing by the multitasking Integrator complex. *Nat. Rev. Mol. Cell Biol. 2022 243* **24**, 204–220 (2022).
225. Mendoza-Figueroa, M. S., Tatomer, D. C. & Wilusz, J. E. The Integrator Complex in Transcription and Development. *Trends Biochem. Sci.* **45**, 923–934 (2020).
226. Offley, S. R. *et al.* A combinatorial approach to uncover an additional Integrator subunit. *Cell Rep.* **42**, (2023).
227. Yokoyama, A. RNA polymerase II-dependent transcription initiated by selectivity factor 1: A central mechanism used by MLL fusion proteins in leukemic transformation. *Front. Genet.* **10**, 722 (2019).
228. Huang, K. L. *et al.* Integrator Recruits Protein Phosphatase 2A to Prevent Pause Release and Facilitate Transcription Termination. *Mol. Cell* **80**, 345-358.e9 (2020).
229. Yue, J. *et al.* Integrator orchestrates RAS/ERK1/2 signaling transcriptional programs. *Genes Dev.* **31**, 1809–1820 (2017).
230. Casamassimi, A. & Ciccodicola, A. Transcriptional Regulation: Molecules, Involved Mechanisms, and Misregulation. *Int. J. Mol. Sci.* **20**, (2019).
231. Petrenko, N. & Struhl, K. Comparison of transcriptional initiation by RNA polymerase II across eukaryotic species. *Elife* **10**, (2021).
232. Chen, X. *et al.* Structures of +1 nucleosome-bound PIC-Mediator complex. *Science* **378**, 62–68 (2022).
233. Vos, S. M., Farnung, L., Urlaub, H. & Cramer, P. Structure of paused transcription complex Pol II–DSIF–NELF. *Nat. 2018 5607720* **560**, 601–606 (2018).
234. Abuhashem, A., Garg, V. & Hadjantonakis, A. K. RNA polymerase II pausing in development: Orchestrating transcription. *Open Biol.* **12**, (2022).
235. Chen, F. X., Smith, E. R. & Shilatifard, A. Born to run: control of transcription elongation by RNA polymerase II. *Nat. Rev. Mol. Cell Biol. 2018 197* **19**, 464–478 (2018).
236. Ohe, S. *et al.* ERK-mediated NELF-A phosphorylation promotes transcription elongation of immediate-early genes by releasing promoter-proximal pausing of RNA polymerase II. *Nat. Commun. 2022 131* **13**, 1–17 (2022).
237. Brookes, E. & Pombo, A. Modifications of RNA polymerase II are pivotal in regulating gene expression states. *EMBO Rep.* **10**, 1213–1219 (2009).
238. Cortazar, M. A. *et al.* Control of RNA Pol II Speed by PNUTS-PP1 and Spt5 Dephosphorylation Facilitates Termination by a “Sitting Duck Torpedo”

Mechanism. *Mol. Cell* **76**, 896-908.e4 (2019).

239. Evan, T., Wang, V. M. Y. & Behrens, A. The roles of intratumour heterogeneity in the biology and treatment of pancreatic ductal adenocarcinoma. *Oncogene 2022 4142* **41**, 4686–4695 (2022).
240. Vlachogiannis, G. *et al.* Patient-derived organoids model treatment response of metastatic gastrointestinal cancers. *Science* **359**, 920–926 (2018).
241. Miyabayashi, K. *et al.* Intraductal Transplantation Models of Human Pancreatic Ductal Adenocarcinoma Reveal Progressive Transition of Molecular Subtypes. *Cancer Discov.* **10**, 1566–1589 (2020).
242. Tiriac, H. *et al.* Organoid Profiling Identifies Common Responders to Chemotherapy in Pancreatic Cancer. *Cancer Discov.* **8**, 1112–1129 (2018).
243. Sugimoto, S. & Sato, T. Organoid vs In Vivo Mouse Model: Which is Better Research Tool to Understand the Biologic Mechanisms of Intestinal Epithelium? *Cell. Mol. Gastroenterol. Hepatol.* **13**, 195 (2022).
244. Davis, R. L. Mechanism of Action and Target Identification: A Matter of Timing in Drug Discovery. *iScience* **23**, 101487 (2020).
245. Herzel, L., Ottoz, D. S. M., Alpert, T. & Neugebauer, K. M. Splicing and transcription touch base: co-transcriptional spliceosome assembly and function. *Nat. Rev. Mol. Cell Biol. 2017 1810* **18**, 637–650 (2017).
246. Aslanzadeh, V. & Beggs, J. D. Revisiting the window of opportunity for cotranscriptional splicing in budding yeast. *RNA* **26**, 1081–1085 (2020).
247. Fong, N. *et al.* Pre-mRNA splicing is facilitated by an optimal RNA polymerase II elongation rate. *Genes Dev.* **28**, 2663–2676 (2014).
248. Tullai, J. W. *et al.* Immediate-Early and Delayed Primary Response Genes are Distinct in Function and Genomic Architecture. *J. Biol. Chem.* **282**, 23981 (2007).
249. Saha, R. N. *et al.* Rapid activity-induced transcription of arc and other IEGs relies on poised RNA polymerase II. *Nat. Neurosci.* **14**, 848 (2011).
250. Bahrami, S. & Drablos, F. Gene regulation in the immediate-early response process. *Adv. Biol. Regul.* **62**, (2016).
251. Stein, C. B. *et al.* Integrator endonuclease drives promoter-proximal termination at all RNA polymerase II-transcribed loci. *Mol. Cell* **82**, 4232-4245.e11 (2022).
252. Elrod, N. D. *et al.* The Integrator Complex Attenuates Promoter-Proximal Transcription at Protein-Coding Genes. *Mol. Cell* **76**, 738-752.e7 (2019).
253. Baillat, D. & Wagner, E. J. Integrator: surprisingly diverse functions in gene expression. *Trends Biochem. Sci.* **40**, 257–264 (2015).
254. Albrecht, T. R. & Wagner, E. J. snRNA 3′ End Formation Requires Heterodimeric Association of Integrator Subunits. *Mol. Cell. Biol.* **32**, 1112–1123 (2012).

255. Zheng, H. *et al.* Identification of Integrator-PP2A complex (INTAC), an RNA polymerase II phosphatase. *Science* **370**, (2020).
256. Hu, S. *et al.* INTAC endonuclease and phosphatase modules differentially regulate transcription by RNA polymerase II. *Mol. Cell* **83**, 1588-1604.e5 (2023).
257. Chen, F. X. *et al.* PAF1, a Molecular Regulator of Promoter-Proximal Pausing by RNA Polymerase II. *Cell* **162**, 1003–1015 (2015).
258. Wang, Z. *et al.* Coordinated regulation of RNA polymerase II pausing and elongation progression by PAF1. *Sci. Adv.* **8**, eabm5504 (2022).
259. Nimmakayala, R. K. *et al.* PAF1 cooperates with YAP1 in metaplastic ducts to promote pancreatic cancer. *Cell Death Dis.* **13**, 839 (2022).
260. Mandal, R., Becker, S. & Strebhardt, K. Targeting CDK9 for anti-cancer therapeutics. *Cancers* vol. 13 (2021).
261. Smith, E. & Shilatifard, A. Transcriptional elongation checkpoint control in development and disease. *Genes Dev.* **27**, 1079–1088 (2013).
262. Franco, L. C., Morales, F., Boffo, S. & Giordano, A. CDK9: A key player in cancer and other diseases. *J. Cell. Biochem.* **119**, 1273–1284 (2018).
263. Vervoort, S. J. *et al.* The PP2A-Integrator-CDK9 axis fine-tunes transcription and can be targeted therapeutically in cancer. *Cell* **184**, 3143-3162.e32 (2021).
264. Dacol, E. C., Wang, S., Chen, Y. & Lepique, A. P. The interaction of SET and protein phosphatase 2A as target for cancer therapy. *Biochim. Biophys. acta. Rev. cancer* **1876**, 188578 (2021).
265. Xu, H. *et al.* Histone acetylation insulator SET orchestrates PP2A inhibition and super-enhancer activation. *bioRxiv* 2023.01.15.524091 (2023) doi:10.1101/2023.01.15.524091.
266. Parua, P. K., Kalan, S., Benjamin, B., Sansó, M. & Fisher, R. P. Distinct Cdk9-phosphatase switches act at the beginning and end of elongation by RNA polymerase II. *Nat. Commun.* **11**, 4338 (2020).
267. Allan Drummond, D. & Wilke, C. O. The evolutionary consequences of erroneous protein synthesis. *Nat. Rev. Genet.* **10**, 715–724 (2009).
268. Read, A. & Schröder, M. The Unfolded Protein Response: An Overview. *Biology (Basel).* **10**, (2021).
269. Senft, D. & Ronai, Z. A. UPR, autophagy, and mitochondria crosstalk underlies the ER stress response. *Trends Biochem. Sci.* **40**, 141–148 (2015).
270. Marcelo, A., Koppenol, R., de Almeida, L. P., Matos, C. A. & Nóbrega, C. Stress granules, RNA-binding proteins and polyglutamine diseases: too much aggregation? *Cell Death Dis.* **12**, 592 (2021).
271. Pakos-Zebrucka, K. *et al.* The integrated stress response. *EMBO Rep.* **17**, 1374–

1395 (2016).

272. Botrus, G. *et al.* Increasing Stress to Induce Apoptosis in Pancreatic Cancer via the Unfolded Protein Response (UPR). *International Journal of Molecular Sciences* vol. 24 (2023).
273. Zeindl-Eberhart, E. *et al.* Epithelial-Mesenchymal Transition Induces Endoplasmic-Reticulum-Stress Response in Human Colorectal Tumor Cells. *PLoS One* **9**, e87386 (2014).
274. Genovese, G. *et al.* Synthetic vulnerabilities of mesenchymal subpopulations in pancreatic cancer. *Nature* **542**, 362–366 (2017).
275. Palamaris, K., Felekouras, E. & Sakellariou, S. Epithelial to Mesenchymal Transition: Key Regulator of Pancreatic Ductal Adenocarcinoma Progression and Chemoresistance. *Cancers* vol. 13 (2021).
276. Nie, Z. *et al.* c-Myc Is a Universal Amplifier of Expressed Genes in Lymphocytes and Embryonic Stem Cells. *Cell* **151**, 68–79 (2012).
277. Lin, C. Y. *et al.* Transcriptional amplification in tumor cells with elevated c-Myc. *Cell* **151**, 56–67 (2012).
278. Lenkiewicz, E. *et al.* Genomic and epigenomic landscaping defines new therapeutic targets for adenosquamous carcinoma of the pancreas. *Cancer Res.* **80**, 4324–4334 (2020).
279. Witkiewicz, A. K. *et al.* Whole-exome sequencing of pancreatic cancer defines genetic diversity and therapeutic targets. *Nat. Commun. 2015 61* **6**, 1–11 (2015).
280. Zatzman, M. *et al.* Widespread hypertranscription in aggressive human cancers. *Sci. Adv.* **8**, eabn0238 (2023).
281. Balamotis, M. A. *et al.* Complexity in transcription control at the activation domain-mediator interface. *Sci. Signal.* **2**, (2009).

10 Acknowledgment

~ Für Hannelore ~
Leider kam LB-100 zu spät.

Unknown at the beginning, LB-100 showed up quickly as an unexpectedly and unpredictable highly personal project and therefore my big thankfulness goes firstly to my supervisor and doctoral father Prof. Dr. Günter Schneider, giving me the chance to graduate with a real heart project. Thanks for your supervision during these years, the unique possibility to work in such an exciting research field, letting me grow as an independent scientist and challenging me for becoming my personal best.

Secondly, I want to thank my second supervisor and mentor during these years, Prof. Dr. Oliver Krämer. You improved the project with other views, notions and ideas. I learned, that all what you need to have is good science and a lovely cat!

Third, I want to thank Prof. Dr. Roland M. Schmid as my third supervisor and head of my research in Munich. Without you, I couldn't finish my doctoral thesis in my hometown, surrounded with my family and friends. I will be forever grateful for that. An additional thank you also for including me in your research team and therefore strengthen my connections in Munich.

Additionally, I want to thank Prof. Dr. Paul Boutz from the University of Rochester (USA) for giving me the chance of an international research exchange and scientific booster during my PhD. I would have never learned so much about splicing without you. Thanks also to Leon and Yang for making this stay unforgettable.

Thanks also to our cooperation partners and teams of AG Saur, AG Rad, AG Reichert, AG Robles and AG Braun for your helping support.

Thank you, old AG Schneider members (Caro, Lukas, Aylin, Svenja, Felix, Zonera, Kathi, Christian) and the medical students for making the first year of my PhD unforgettable. We had the best time together! An outstanding thank you also to AG Geisler (Steffi and Simone) and the basement group for take over the team-part after the move of AG

Schneider. I really will miss our ritual tea break in the morning! Steffi, a special thanks for your help with all the orderings and work orders, your time for my English improvement and for all the cat stories and reels :)

Last but not least and for me the most important thank you goes to my family, my boyfriend and friends, for keeping my head up during these years, always succour and supporting me during these hard times. Without you, I wouldn’t be the one I am.

Dear Lollo, unfortunately you can't see and experience it anymore, but you were my internal driver and motivation for this thesis. I will never forget you!